



UNIVERSITA' DEGLI STUDI DI VERONA

DIPARTIMENTO DI

Biotecnologie

SCUOLA DI DOTTORATO DI

Scienze Naturali e Ingegneristiche

DOTTORATO DI RICERCA IN

Nanoscience and Advanced Technologies

XXXV/2019

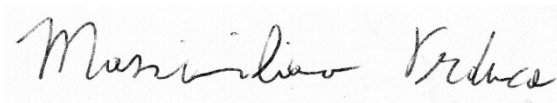
Improving bioavailability of insoluble payloads through PLGA nanotechnology

S.S.D. BIO/11 BIOLOGIA MOLECOLARE

Coordinatore: Prof. Adolfo Speghini

Firma _____

Tutor: Prof. Massimiliano Perduca

Firma  _____

Ph.D student Dott. Salvatore Calogero Gaglio

Firma



ABSTRACT	9
<hr/>	
INTRODUCTION	11
<hr/>	
1. IMPROVING BIOAVAILABILITY OF INSOLUBLE PAYLOADS	11
2. ENCAPSULATION TECHNOLOGIES	14
3. THE “NANO” IN MEDICINE	16
4. DRUG DELIVERY SYSTEMS	18
5. PLGA THE “GOLDEN” STANDARD	20
PLGA NANOTECHNOLOGY	23
<hr/>	
OXYRESVERATROL INHIBITS R848-INDUCED PRO-INFLAMMATORY MEDIATORS RELEASE BY HUMAN DENDRITIC CELLS EVEN WHEN EMBEDDED IN PLGA NANOPARTICLES	23
1.1 AIM	24
1.2 INTRODUCTION	25
1.3 EXPERIMENTAL SECTION	26
1.4 RESULTS	31
1.5 DISCUSSION	38
1.6 CONCLUSION	41
OXYRESVERATROL-LOADED PLGA NANOPARTICLES INHIBIT OXYGEN FREE RADICAL PRODUCTION BY HUMAN MONOCYTES: ROLE IN NANOPARTICLE BIOCOMPATIBILITY	43
2.1 AIM	44
2.2 INTRODUCTION	45
2.3 EXPERIMENTAL SECTION	47
2.4 RESULTS	52
2.5 DISCUSSION	58
2.6 CONCLUSION	60
FISETIN: AN INTEGRATED APPROACH TO IDENTIFY A STRATEGY PROMOTING OSTEOGENESIS	62
3.1 AIM	63
3.2 INTRODUCTION	64
3.3 EXPERIMENTAL SECTION	66
3.4 RESULTS	72
3.5 DISCUSSION	80
3.6 CONCLUSION	82
EMBEDDING BIOMIMETIC MAGNETIC NANOPARTICLES COUPLED WITH PEPTIDE AS-48 INTO PLGA TO TREAT INTRACELLULAR PATHOGENS	84
4.1 AIM	85
4.2 INTRODUCTION	86
4.3 EXPERIMENTAL SECTION	90
4.4 RESULTS	98
4.5 DISCUSSION	111

4.6 CONCLUSION	115
NIR CIRCULARLY POLARIZED LUMINESCENCE FROM WATER STABLE ORGANIC NANOPARTICLES CONTAINING A CHIRAL YB(III) COMPLEX	117
5.1 AIM	118
5.2 INTRODUCTION	120
5.3 EXPERIMENTAL SECTION	122
5.4 RESULTS	124
5.5 DISCUSSION	128
5.6 CONCLUSION	129
<u>CONCLUSION</u>	<u>131</u>
<u>REFERENCES</u>	<u>133</u>

Before starting to read this thesis which I hope you will appreciate, there are many people who have participated in my personal growth achieved so far.

*Among all, my supervisor as well as mentor **Prof. Massimiliano Perduca**, for his constant support and for allowing me to express myself at my best.*

*I thank **Prof. Concepción Jiménez López** for her trust and for making her laboratories available to me. It was an honour to join her team and give my contribution.*

Special thanks also to all the researchers, professors and PhD students who have tested the nanomaterials and who have taught me new methodologies.

I remember with joy ... PhD Ylenia Jabalera Ruz, PhD Francesca Oltolina, Prof. Stefano Dusi, PhD Marta Donini, Prof. Alessandro Romeo, Prof. Manuel Montalbán López, Prof. Guillermo Iglesias Salto ...

“TRY TO BECOME NOT A MAN OF SUCCESS,
BUT RATHER A MAN OF VALUE.”

A. Einstein

*L'intera opera è dedicata alla mia famiglia,
una costante senza la quale,
non sarei giunto ai massimi accademici.*

G. P. N.

Ai tuoi prossimi migliori passi ...

SC.G

Abstract

Bioactive molecules are a cluster of natural or synthetic compounds, which modulate actions in the body promoting good health. Furthermore, they have been applied in the prevention of cancer, heart disease, and other diseases for their antioxidant, anti-inflammatory, anti-microbial, anti-cancer properties. Among them, many are hydrophobic or poorly soluble nutrients, such as phenolic compounds, carotenoids, essential oils, essential fatty acids, insoluble peptides, and vitamins. Their low water solubility is the limiting factor for their use in both nutraceutical and pharmacological industries. In fact, drugs with poor water solubility show a slower absorption rate, which can lead to inadequate bioavailability making the drug ineffective. Furthermore, hydrophobic molecules can also be used as bio-probe for imaging purpose. Narrow bandwidth emissions and large Stokes shifts make lanthanide complexes interesting as versatile molecular probes of biological systems. Nevertheless, they are not widely used for imaging purpose since their luminescence is completely quenched in aqueous environment.

In this scenario, nanoencapsulation through the use of polymeric nanoparticles (NPs) could be an effective solution to improve solubility and protection of the insoluble payload with consequent increase in bioavailability and action. Poly lactic-co-glycolic acid (PLGA) is a synthetic copolymer of lactic acid and glycolic acid of remarkable interest for potential applications in biomedicine; indeed, for its biodegradability and biocompatibility, it has been approved for human use both by Food and Drug Administration (FDA) and European Medicine Agency (EMA). In this thesis, we want to give several proofs of concept about the huge potentiality of PLGA nanoparticles in medical purpose. We used single emulsion method (O/W) to encapsulate natural bioactive molecules producing plant-derived PLGA nanocarriers enabling anti-inflammatory and antioxidant activity when the polyphenol Oxyresveratrol has been incorporated into PLGA NPs. Moreover, an osteogenic promoting action has been observed when PLGA NPs have been embedded with Fisetin (a natural flavonoid).

Since PLGA can deliver more than one payload simultaneously, we also produced PLGA nanoassemblies able to combine antibacterial activity with physical treatments (such as magnetic and photothermic hyperthermia). Finally, we exploited the shielding properties of PLGA to preserve the luminescence of NIR-emitting lanthanide complexes in aqueous environment. Therefore, we produced a NIR-CPL probe based on PLGA for bioassay imaging.

To summarise, during the past three years we were able to use PLGA encapsulation technology to make natural or synthetic compounds bioavailable, even if naturally water insoluble, and use the loaded nanomaterials in in-vitro experiments assessing the activity of the encapsulated material, paving the way for their application in in-vivo tests and eventual use in nanomedicine.

Introduction

1. Improving bioavailability of insoluble payloads

Natural or synthetic compounds which modulate actions in the body promoting good health are defined as bioactive molecules (figure 1). Furthermore, their role has also been studied across different fields in the prevention of cancer, heart disease, and other diseases for their beneficial antioxidant, anti-inflammatory, anti-microbial, anti-cancer properties.¹ Among them, many are hydrophobic or poorly soluble nutrients such as phenolic compounds, carotenoids, essential oils, essential fatty acids, insoluble peptides and vitamins². The low water solubility is the limiting factor for their use in both nutraceutical and pharmacological industries.¹⁻³ Solubility is a parameter that most influences the concentration of a drug in the systemic circulation to achieve the desired pharmacological response. Drugs with poor water solubility show a slower absorption rate, which can lead to inadequate bioavailability making the drug ineffective.^{4,5} Around ~60% of all the active pharmaceutical ingredients (API) are administered almost exclusively orally. The popularity of the oral route administration is related with the high patient compliance, especially in cases of chronic diseases.^{6,7}

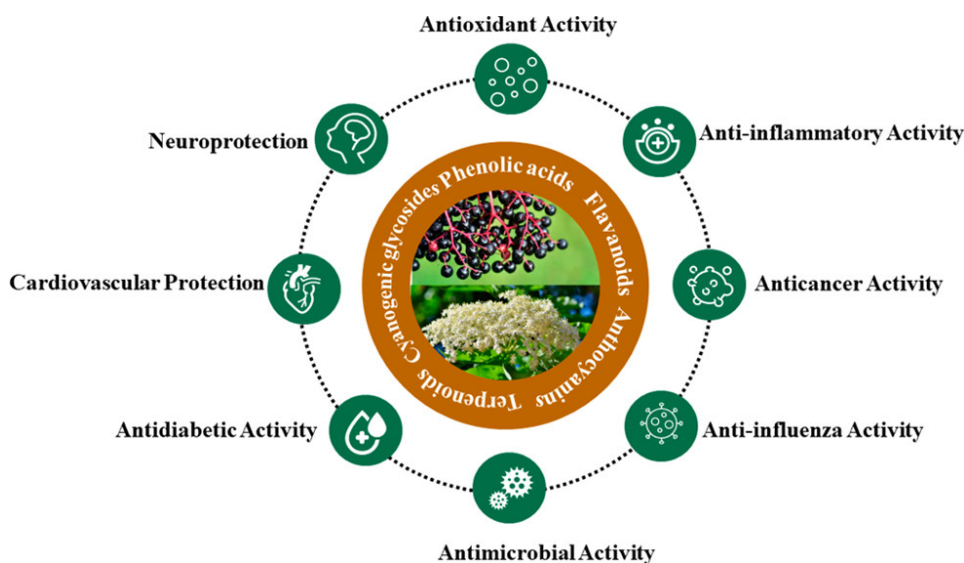


Figure 1. Several beneficial properties of natural bioactive hydrophobic molecules⁸.

Furthermore, hydrophobic compounds can also be used as bio probe for imaging purpose. In this scenario, narrow bandwidth emissions and large Stokes shifts makes lanthanides complexes interesting as versatile molecular probes of biological systems^{9,10}. Despite, lanthanide-based probes can be adopted to improve detection sensitivity and imaging depth, they are not widely utilized for biological imaging. Lanthanides fluorescence intensity depends not only on the efficacy of energy transfer from the antenna to the donor (antenna effect) but also on the presence of non-radiative quenching phenomena¹¹. Unfortunately, in aqueous medium lanthanide fluorescence is reduced by the presence of an alternative pathway to dissipate the excited state in the form of vibrational energy transfer to water molecules; this phenomenon is called multiphonon relaxation (figure 2)^{11,12}.

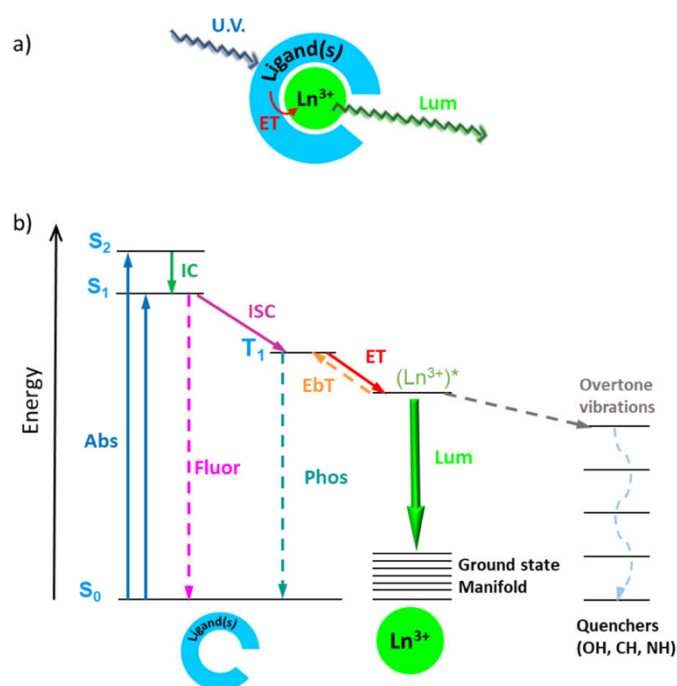


Figure 2. (a) Schematic representation of the antenna effect, and (b) Jablonski diagram of the antenna effect (solid arrows) together with competing energy transitions (dashed arrows). Abs: absorbance; IC: internal conversion; Fluor: fluorescence; ISC: intersystem crossing; Phos: phosphorescence; ET: energy transfer; EbT: energy back-transfer; Lum: luminescence.

https://encyclopedia.pub/entry/history/compare_revision/31497

Therefore, improving the bioavailability and protection to exploit the multiple possibilities of insoluble molecules, opens new possible uses of these compounds in healthcare industries.

2. Encapsulation technologies

Besides low solubility and poor bioavailability, the application of bioactive compounds is also greatly limited by their chemical instability and susceptibility to oxidative degradation. Encapsulation consists in coating molecules of interest with protective material to prepare nano and micro formulations able to enhance their beneficial properties¹³. From one side, encapsulation can enhance biomolecules health-promoting and anti-disease activities by improving water solubility, while from the other side, it can preserve payloads from environmental stresses^{14,15}. In pharmaceutical and food industries, nano and micro scale particles are widely used to preserve bioactive compounds (micronutrients, polyphenols, carotenoids, peptide etc.) by improving physical stability and shelf life^{14,16,17}. The size range that distinguishes nanoparticles from microparticles has not yet been clarified and is subject to debate¹⁸. To simplify, we will refer to nanoencapsulation as all methods to produce particles in the 10-1000 nm, and to microencapsulation as those producing particles 3-8 μm according to Rossi *et al.* statement¹⁹. Table 1 resumes the common features and the difference between the two encapsulation methods. Despite both methods share the ability to protect payloads as well as to enhance bioavailability, it is important to distinguish some differences.

Micro-encapsulation is used to mask unpleasant flavor of micronutrients like essential oils, polyphenols and so on¹³. Prolonged release is required in tissue reconstruction to promote healing on the damage site, thus, microparticles have been used in bone regeneration providing sustained release of growth factors for several days or weeks²⁰. Additionally, micro-encapsulation technologies represent a potential tool in tissue engineering and regenerative medicine since microparticles can be designed to produce scaffold and to delivery living cells to the target²¹.

Nano-encapsulation is suitable for precision medicine and in those applications like cancer therapy, in which increasing the targeting accuracy is required to avoid side effects²². Additionally, nanoparticles show an enhanced cellular uptake increasing

the effectiveness of the drug even at lower dosage²³. Thanks to the smaller and the narrow size distribution, nanoparticles can be designed to overcome complex biological barriers (such as the Blood–Brain Barrier (BBB)) by directly crossing the physiochemical barriers and improving therapeutic indices²². Hirano *et al*²⁴ have designed a PLGA based nanocarrier (~200 nm) for improving the penetration of ketamine through the Blood–Brain Barrier (BBB).²⁵

Table 1. Comparison between Micro-encapsulation and Nano-encapsulation.

Micro-encapsulation		Nano-encapsulation	
I.	Protection of bioactive compounds	I.	Protection of bioactive compounds
II.	Controlling release profile	II.	Controlling release profile
III.	Increase chemical-physical stability and extend shelf life	III.	increase physical stability and extend shelf life
IV.	Increase bioavailability	IV.	Increase bioavailability
V.	Improvement of flow properties	V.	Create narrow distribution and increase the surface area
VI.	Masking the unwanted flavors	VI.	Increase targeting accuracy and promote passage through fenestrated cells
VII.	Prolonged release	VII.	Enhance intracellular uptake
		VIII.	Enhanced permeability effect (EPR)

Therefore, encapsulation plays a crucial role to preserve as well as enhance the functionality of bioactive molecules.

3. The “Nano” in medicine

The interest of nanotechnology in medicine has arisen for many reasons:

- I. Difficulties associated to bioactive compounds with poor intrinsic solubility
- II. Pathogen drug resistance conditions due to chronic use
- III. Increase in cases of undesirable effects due to the non-achievement of the therapeutic concentration

These drawbacks can be overcome by using nanoencapsulation technologies, which is the design and the production of nanoparticles (generally less than 1000 nm) used as carrier to add or improve properties to biological active compounds^{26,27}. Thus, we refer to Nanomedicine as the application of nanotechnology to achieve innovation in healthcare^{28,29}. Interestingly, at the nano-scale, the surface-to-volume ratio increase dramatically, adding new physical chemical properties compared to the bulk-scale³⁰.

Drug delivery through nanotechnology could enhance efficacy by reducing the dosage and providing active-targeting to the site of interest³¹: this means that the drug can reach the suitable concentration *in situ* reducing adverse effects. Moreover, nanoparticles can reach several grades of complexity enabling the possibilities of combining physical treatment with chemotherapy. This strategy allows the use of chemotherapy agents at lower doses with benefits not only in reducing side effects but also in avoiding the development of a condition called multidrug resistance (MDR) which leads in most cases to therapy failure³²⁻³⁴. Jabalera *et al* developed a nanoassembly showing at lower dosage anti-tumor activity close to free doxorubicin when hyperthermia was combined with the chemotherapy³⁵. Liposomes, nanocrystals, micelles, nanospheres and nanocapsules, solid lipid nanoparticles (SLNs) and nano-lipid carriers (NLCs) have all been used in attempts to improve the side

effect profile of APIs by targeting drug delivery and enhanced stability by shielding APIs from the harsh, gastrointestinal tract (GIT) ³⁶.

The choice of the “building blocks” is critical for nanocarrier optimization and usually these are the guidelines to follow for an effective design:

- I. Characteristics of bioactive agents like size, solubility, charge etc.
- I. Safety and effectiveness of the drug-carrier complex
- II. Route of administration

For applications in humans, it is evident that the fundamental parameter to be satisfied is biocompatibility. Biocompatibility is the ability of a material to perform its desired function without causing any local or systemic adverse response. Additionally, the biocompatible property is mostly influenced by the materials employed, the site and duration of exposure, and to the host. Therefore, it is necessary to test the effects of the interaction between nanocarriers and biological systems in a wide spectrum, ranging from cytotoxicity tests and immune responses caused by exceptional events such as cell priming³⁶⁻³⁸.

4. Drug delivery systems

Nanoparticles widely used for precision medicine can be grouped into three main classes: lipid-based, polymeric, inorganic.

Inorganic nanoparticles (INPs) are prepared with extreme precision by modulating structure and shape adapting physico-chemical properties to the desired application. For instance, different drug release profiles can be obtained controlling the pore size of porous in silica nanoparticles³⁹. Furthermore, INPs can operate as theranostic, imaging and photothermal agents thank to the physico-chemical features. Gold nanoparticles are often used for the diagnosis and photothermal treatment of tumours⁴⁰. Among the FDA-approved inorganic nanomedicines, most are magnetic iron oxide NPs possessing superparamagnetic properties. They have been employed as contrast agents, drug delivery vehicles, and thermal-based therapies^{41,42}. Despite the numerous advantages, these nanoparticles are biocompatible but not biodegradable. Consequently, bioaccumulation could trigger to undesirable effects.⁴³

Due to the similar morphology to cellular membrane, Liposomes are widely employed as delivery system representing a huge part of the FDA-approved nanomedicines^{44,45}. They consist of phospholipids which can form unilamellar and multilamellar vesicular structure allowing to transport hydrophilic compounds inside the vesicle and lipophilic drugs in the phospholipid's bilayer, even simultaneously. Liposomes are easy to prepare and biodegradable with very low toxicity: they provide sustained or controlled release, protection of drugs from degradation, superior therapeutic effects.⁴⁶ Nevertheless, they show low Encapsulation Efficiency (EE) which increase the manufacturing cost since a considerable amount of drug is lost. Additionally, for clinical application liposome-based delivery system requires further modification to extend the circulation time since they are rapidly absorbed by the reticuloendothelial system^{47,48}. Surface modifications of liposome represent drawbacks in scaling up procedure and they also could affect the EE. Lipid nanoparticles

(LNPs) are another sub-class of lipid-based delivery system with tuneable matrix core that differs from the vesicular structure of liposomes. They are mainly employed in nucleic acid delivery, however, LNP systems are still limited by low drug loading and biodistribution ^{48,49}.

Polymeric nanoparticles (PNPs) are the third class of nanocarriers commonly employed in medicine: they are biodegradable, easy to fabricate, low toxic to the human body and cost effective. Compared to lipid-based NPs, PNPs dramatically increase the EE and the preparation method allow more reproducibility with a narrow-size distribution of nanoparticles ⁵⁰⁻⁵². Additionally, they have improved stability and cargo retention efficiency useful to stimulate immune response in vaccination. PNPs are also cost-effectiveness and some of the preparation methods, such as microfluidics and nanoprecipitation, are suitable to scale up compared to those of the lipid-based NPs. ^{50,53} Payloads can be encapsulated within the core, trapped in the polymer matrix, chemically conjugated to the polymer, or bound to the surface. This enables the precise modulation of the drug release profile. Various therapeutic substances including hydrophobic and hydrophilic compounds, as well as cargoes with different molecular weights can be delivered. Additionally, PNPs are ideal in co-delivery applications. PNPs can be produced as nanocapsules in which the inner core is divided by a polymeric bilayer called polymerosome, or as nanospheres consisting of polymeric matrices or highly branched structures (dendrimers).^{42,54}

5. PLGA the “golden” standard

Among all the nanocarriers, the polymeric polylactic-co-glycolic acid (PLGA) has shown tremendous advantages by adding innovation in the pharmaceutical industry, especially as a drug delivery system^{55,56}. Poly lactic-co-glycolic acid is a synthetic biodegradable copolymer of lactic acid (LA) and glycolic (GA) acid. In 1989, Lupron® Depot was the first drug delivery system based on PLGA microspheres approved by the Food and Drug Administration (FDA) and used in the treatment of prostate cancer⁵⁶.

Interestingly, its degradation rate can be modulated by regulating the LA/GA ratio of PLGA, leading to a sustained drug release profile that reduces harmful side effects and improves patient compliance⁵⁰. Additionally, it is also approved by the European Medicine Agency (EMA) as drug delivery system for parenteral administration and used as component of biodegradable sutures⁵⁵. PLGA is degraded by spontaneous hydrolysis when resuspended in an aqueous environment and its by-products are completely metabolized by Krebs cycles. Furthermore, due to its adjustable degradation rate through variation of its monomer ratios or molecular weights, PLGA is widely used as scaffolding materials for regenerative medicine and control drug release in the field of precision therapy⁵⁷. The “erosion” of PLGA nanostructure in water environment is the mechanism driving the release of the drug. Depending on the location of the payload different release patterns can be modulated. For example, when the cargo is on the surface of PLGA NP a “burst release” occurs while the cargo within it is released over an extended time. The scenario where part of the payload is on the surface and the other fraction is within the polymer matrix leads to sustained release.⁵⁸

Moreover, the ability to protect the payload and to modulate the physicochemical properties with the synthesis and functionalization, make PLGA a versatile material for multiple applications in medicine⁵⁹. Surface of PLGA NPs can be functionalized with ligands, such as antibodies, aptamers, peptides, or small molecules, that

for instance can recognize tumor-specific antigens, to provide an active targeting towards specific organs or cells^{60,61}.

In summary, the benefits added by using PLGA nanoparticles are:

- I. Achieving target site and reducing the toxicity of bioactive agents, using a biodegradable non-toxic polymer
- II. Enhancing the solubility of drugs which are hydrophobic by nature
- III. Shielding the active molecule from degradation by the environment
- IV. Control on drug release rate
- V. Delivering drugs through biological barriers such as blood-brain barrier and tight epithelial junctions

PLGA is suitable for delivering more than one payload finding application in theranostics and dual treatments. For instance, Edurne Luque-Michel *et al.* co-encapsulated Doxorubicin with SPIONs (Superparamagnetic iron oxide nanoparticles) in PLGA, to monitor the treatment in real time by Magnetic Resonance Imaging⁶².

PLGA nanoparticles with precise physico-chemical properties can be prepared changing parameters such as temperature, pH, concentration, organic solvent, polymer weight, ratio, surfactant, of the method employed; among several methods, single emulsion oil/water (O/W) is suitable to encapsulate hydrophobic payload in PLGA NPs. Briefly, the polymer is dissolved in an organic phase (e.g., acetone, dichloromethane) and emulsified under stirring in an aqueous solution in presence of a surfactant (i.e., polyvinyl alcohol, sodium dodecyl sulphate) which is used to stabilize nano-scale PLGA particles avoiding aggregation phenomenon^{63,64}. Then, the emulsion is usually left under stirring to favour organic solvent evaporation. This method allows to encapsulation of hydrophobic molecules simply dissolving them in the organic phase with the polymer. The Nanoparticles obtained are approximately 150-200 nm with long-circulating time since they should be able to

avoid fast clearance by the reticuloendothelial system⁶⁵ and the rapid elimination through the kidneys⁶⁶.

A simpler method used to obtain smaller PLGA nanoparticles encapsulating hydrophobic payloads (>100 nm) is nanoprecipitation^{67,68}. On the contrary of the single emulsion method, this is a one-step procedure in which nanoparticles are instantaneously generated and it can be easily scaled up. The method requires addition of two phases: the “solvent” is the organic phase in which the polymer and the drug are dissolved, while the “anti-solvent” is the aqueous phase. Nanoparticles are formed by mixing the solvent and the anti-solvent, to increase the supersaturation condition⁶⁹.

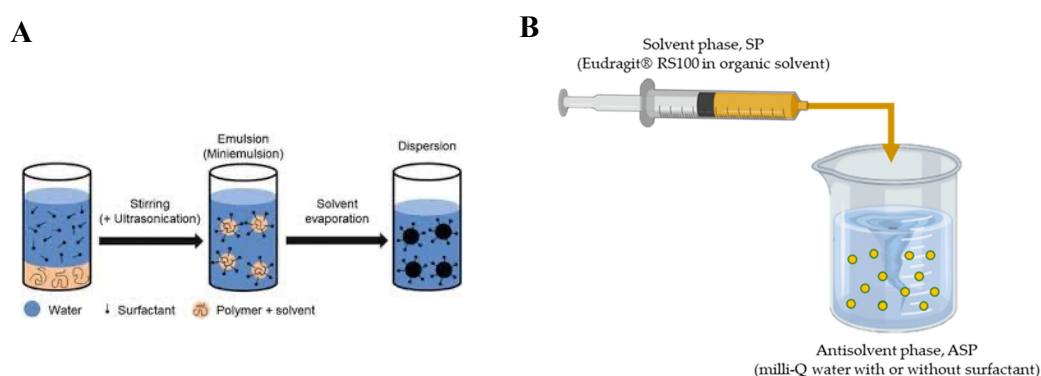


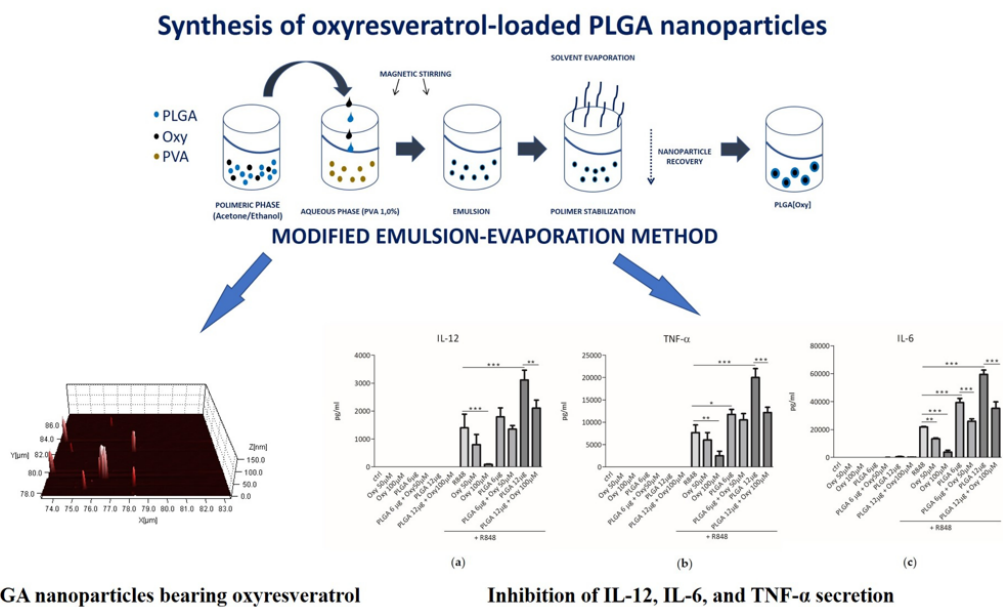
Figure 3. Two-step, Single Emulsion Evaporation method (A)⁷⁰; one-step Nanoprecipitation⁷¹.

In the following chapters we optimized the parameters for producing PLGA nanoparticles suitable for delivering small molecules like plant-derived bioactive, for the first time tested in this context, and NIR-bioprobes.

We also gave a proof of concept in adapting PLGA Nanoparticle protocols for assembling multifunctional Nanoplatform.

PLGA Nanotechnology

Oxyresveratrol Inhibits R848-Induced Pro-Inflammatory Mediators Release by Human Dendritic Cells Even When Embedded in PLGA Nanoparticles



Gaglio, S.C *et al.* *Molecules* 2021, 26, 2106, <https://doi.org/10.3390/molecules26082106>

1.1 Aim

The administration of nanostructures to patients is sometimes hampered by possible undesirable effects related to intrinsic defense mechanism activation: nanoparticles interacting with immune cells, such as Dendritic Cells (DCs), can cause their activation and consequently adverse effects such as inflammation or allergy ⁷². Ox-
yresveratrol, a stilbene extracted from the plant *Artocarpus lakoocha* Roxb, has been reported to provide a considerable anti-inflammatory activity. Thus, we investigated whether the interaction with PLGA particles produced a DC response and whether the insertion of an anti-inflammatory molecules such as oxyresveratrol was able to downregulate inflammatory cytokine expression.

1.2 Introduction

Dendritic cells (DCs) play a fundamental role in regulating both inflammatory and adaptive immune response. DCs undergo a process of maturation which enables them to present antigens to lymphocytes activating the specific immune response⁷³⁻⁷⁵. Mature DCs produce chemical mediators that modulate the adaptive immune reaction and the inflammatory process against pathogen microorganisms and cancer cells. IL-12 is a fundamental cytokine activating natural killer cells and T lymphocytes^{76,77}, while IL-6 and TNF- α are involved in the induction of the systemic acute phase reaction characterized by fever, headache, changes in the sleep-wake cycle, anorexia, nausea and emesis^{78,79}. Švajger *et al*⁸⁰ demonstrated the anti-inflammatory activity of the polyphenol resveratrol, when dendritic cells have been treated in the differentiation phase. The cells showed a reduction in expression of inflammatory molecules, such as IL-12 and an increased secretion of the immunosuppressive cytokine IL-10.

Oxyresveratrol is a polyphenol extracted from *Artocarpus lakoocha* Roxb. heartwood, a plant known in Thai as ‘Ma-Haad’ and used in traditional medicine⁸¹; compared to resveratrol, it has an additional OH- group which should increase the biological effect. The anti-inflammatory effect of oxy-resveratrol is mainly attributed to the downregulation of pro-inflammatory cytokine production⁸²⁻⁸⁵. As far as we know, no investigations have been made on the effect of oxyresveratrol on the functional activity of human DCs, which play an essential role in activation of inflammation and immune reaction⁷³⁻⁷⁵. We found that oxyresveratrol did not elicit per se the release of these cytokines, but inhibited their secretion induced upon DC stimulation. To verify the anti-inflammatory activity of the polyphenol inside nanoparticles, empty and oxyresveratrol-loaded PLGA nanoparticles were prepared. From one side, empty nanoparticles did not elicit cytokine secretion in resting DCs, from the other side they increased IL-12, IL-6, and TNF- α secretion in R848-stimulated DCs, an event known as “priming effect”.

1.3 Experimental Section

Material. RPMI 1640 and low-endotoxin FBS were obtained from Lonza (Walkersville, MD, USA). Recombinant human GM-CSF and human IL-4 were purchased from Miltenyi Biotec (Bergisch Gladbach, Germany); Flow cytometric analysis was performed using the following mouse anti-human antibodies: CD83 (HB15e) and CD1a (HI149) (Becton Dickinson, San Jose, CA, USA); CD80 (2D10), CD86 (T2.2), HLA-DR (L243) and CD14 (M5E2) (Biolegend, San Diego, CA, USA). PLGA (poly[DL-lactide-co-glycolide] 50:50 lactide-glycolide ratio, CAS 26780-50-7), PVA (poly[vinyl alcohol], CAS 9002-89-5), Acetone ($\geq 99\%$ purity, 1.00013), Dimethyl sulfoxide (DMSO, $\geq 99\%$ purity D-5879), Oxyresveratrol ($\geq 97\%$ purity, 91211) were purchased from Sigma-Aldrich, (St. Louis, MO, USA).

Preparation of PLGA nanoparticles. The protocol used to produce PLGA nanoparticles loading oxyresveratrol is based on the single emulsion-evaporation method, under sterile conditions at 20 °C ⁸⁶. 10 mg of the polymer and 5 mM (1.22 mg) of oxyresveratrol from *Artocarpus lakoocha* heartwood were co-dissolved in 1 mL of organic solvent (95% Acetone and 5% DMSO); the obtained organic phase was added dropwise under stirring (2000 RPM) to 10 mL of 1% polyvinyl alcohol (PVA) aqueous solution and left overnight to evaporate the organic phase. Afterwards, the preparation was pelleted at 4 °C 11,000 rpm for 20 min (Eppendorf Centrifuge 5804R) and nanoparticles were collected and washed twice with 10 mL of Milli-Q water. Finally, purified nanoparticles were re-suspended in 1 mL of phosphate buffer saline solution pH 7.4 for the subsequent analysis and storage at 4 °C, otherwise freeze-dried. Empty PLGA nanoparticles were prepared with the same protocol avoiding the addition of oxyresveratrol to the organic phase.

Size and ζ -potential characterization. Size and ζ -potential of PLGA nanoparticles were estimated at 25 °C using a Nano Zeta Sizer ZS (ZEN3600, Malvern Instruments, Malvern, Worcestershire, UK). Before performing the analysis, samples were diluted 10 times from the stock solutions in PBS for size determination and

into in 10 mM NaClO₄ pH 7.5 for ζ -Potential measurements; data were collected in triplicate and analyzed by the ZetaSizer software (version 7.10).

To further support DLS data, a Nanosight tracking analysis was performed on PLGA[Oxy] NPs and empty PLGA nanoparticles (Malvern NanoSight NS300, Malvern Panalytical Ltd, Malvern, UK). Due to the high concentration, each sample was diluted 5000 times in PBS; 1498 frames divided in 3 runs of 60 s were recorded at camera level of 13 and the analysis were performed with a detection threshold in the range 5–7. Finally, the number of particles/mL was estimated as well. Moreover, pictures by atomic force microscopy of both nanoparticle types were acquired: 20 μ L of each sample (prepared as in the above section) were loaded on a bracket covered by inert mica surface. After 20 min for solvent evaporation, the analysis was performed using a NT-MDT Solver Pro atomic force microscope (Moscow, Russia) with NT-MDT NSG01 golden coated silicon tip in semi contact mode with different scanning frequencies (3–1 Hz) to produce optimized AFM images. The microscope was calibrated by a calibration grating (TGQ1 from NT-MDT) to reduce nonlinearity and hysteresis in the measurements. Finally, images were processed with the Scanning Probe Image Processor (SPIPTM) program (Image Metrology ApS, version 5.13, Lyngby, Denmark) and a statistical study was performed to compare results to DLS and Nanosight data.

Spectroscopic Studies, Encapsulation Efficiency and Release Evaluation. To assess the presence of oxyresveratrol inside our nanoparticles the emission pattern was recorded upon excitation at 335 nm, the absorption wavelength of the polyphenol, by using a Jasco Spectrofluorometer FP-8200 (Easton, MD, USA).

To quantify the amount of the entrapped oxyresveratrol (Encapsulation Efficiency), a direct method was used. PLGA[Oxy] NPs were dissolved in DMSO and the obtained solution was analyzed using a calibration curve (Figure 4). Encapsulation efficiency was estimated using the following Equation (1):

$$(1) \quad EE(\%) = \frac{OxyR_{loaded}}{OxyR_{fed}} \times 100$$

To confirm these data, a second method has been employed as well: waste supernatants from the nanoparticle preparation were collected and analyzed by comparing data to a second calibration curve obtained in Milli-Q water (Figure 4). The value of loaded oxyresveratrol ($OxyR_{loaded}$) was indirectly estimated by the following Equations (2) and (3) and finally EE was calculated as described above.

$$(2) \ OxyR_{loaded} = OxyR_{fed} - OxyR_{lost}$$

$$(3) \ OxyR_{loaded} = OxyR_{supernatant} + OxyR_{wash1} + OxyR_{wash2}$$

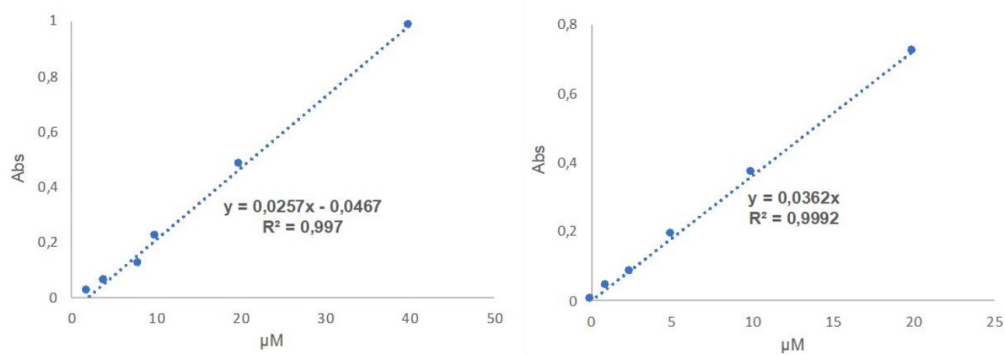


Figure 4. Calibration curve for oxyresveratrol in DMSO (left). Calibration curve for oxyresveratrol in aqueous solution (right).

To assess the ability of the nanoparticles to retain oxyresveratrol over the time, a release study was performed in 1 mL of PBS pH 7.4 at 4 and 37 °C. Samples were collected at different time intervals and replaced with an equal volume of media to maintain the sink condition. The released OxyR was quantified using a calibration curve obtained by UV-Visible spectroscopy at 335 nm.

Dendritic cells (DCs) culture. After written informed consent and upon approval of the ethical committee (Prot. N. 5626, 2 February 2012; Prot. n. 57182, 16 October 2019), buffy coats from the venous blood of normal healthy volunteers were obtained from the Blood Transfusion Centre of the University of Verona. Peripheral blood mononuclear cells were isolated by Ficoll-Hypaque and Percoll (GE Healthcare Life Science) density gradients and used as a source for

immunomagnetic isolation of CD14-positive cells (Miltenyi Biotec GmbH). The purity of CD14+ cells was always greater than 98%, as determined by flow cytometry. To generate immature DCs, monocytes were cultured at 37 °C, 5% CO₂ at 1 × 10⁶/mL in 6-well tissue culture plates (Greiner, Nurtigen, Germany) in RPMI-1640 supplemented with 10% FBS (<0.5 EU/mL; Sigma-Aldrich, (St. Louis, MO, USA), 2 mM l-glutamine, 50 ng/mL GM-CSF and 20 ng/mL IL-4. After 5 days, non-adherent immature DCs were harvested and characterized by flow cytometry as CD1a^{high}, CD80⁻, CD83⁻, CD86^{low} and HLA-DR^{low}. To induce cytokine release, DCs were stimulated for 24 h with 5 μM R848 (Invivogen).

Quantification of Cytokine Production. ELISA development kits purchased from Mabtech (Nacka Strand, Sweden) were used to assay the protein levels of IL-12 (p70) (range 6–600 pg/mL), IL-6 (range 10–1000 pg/mL) and TNF-α (range 4–400 pg/mL) in the cell culture supernatant, according to the manufacturer's instructions. Briefly, DCs resting or activated with 5 μM R848 were treated with oxyresveratrol alone or encapsulated in PLGA nanoparticles, or with corresponding amounts of bare PLGA particles for 24 h, and then the supernatants were collected. Several dilutions of each supernatant were incubated for 2 h at room temperature protected from the light in appropriate assay plates (EIA/RIA Plate, 96 Well Half Area, Flat Bottom, High Binding purchased from Corning (Corning, NY, USA)) previously coated overnight at 4 °C with 50 μL/well Capture Antibody and then blocked by addition of 100 μL/well Assay Diluent for 1 h at RT. Supernatants were discarded and Detection Antibody (50 μL/well) was added. After 1 h incubation at RT, Avidin-HRP (50 μL/well, 30 min) and subsequently Substrate Solution (50 μL/well, 15 min), were added. The reaction was stopped with Stop Solution. Every step of the above procedure was followed by appropriate plate washes. The plates were read at 450 nm with Victor3 1420 Multilabel Counter PerkinElmer. A standard curve was prepared by serial dilution of standards and used for determining the cytokine concentrations in supernatants.

Cell Viability Evaluation. Cell viability was assessed using the Cell Proliferation Reagent WST-1 assay (Roche Diagnostics GmbH, Mannheim, Germany) according to the manufacturer's instructions. DCs resting or activated with R848 were treated with oxyresveratrol alone or encapsulated in PLGA nanoparticles, or with corresponding amounts of bare PLGA particles for 24 h. After treatment, cell supernatant was removed and 50 μ L of pre-warmed fresh complete medium were added to the cells and to 3 empty wells (Blank). A 2 \times WST solution was freshly prepared by dilution of the 10 \times WST reagent in the complete medium and a volume of 50 μ L was dispensed in the wells and blank. The plate was incubated for 60 min. The absorbance (OD) of the samples was measured using a Victor3 multilabel reader (PerkinElmer, Shelton, CT, USA) at 450 nm.

Statistical analysis. Data are expressed as means + SD. Statistical analyses, including two-way ANOVA followed by Bonferroni post-test, were performed with GraphPad Prism 5 (GraphPad Software, Inc., San Diego, CA, USA).

**All the *in vitro* experiment has been performed thanks to Prof Dusi's Lab,
Department of Medicine, Section of General Pathology**

**All the AFM experiments were performed thanks to the equipment provided
by prof. Alessandro Romeo, Department of Biotechnology LAPS (Laboratory
for Photovoltaics and Solid State Physics)**

1.4 Results

1.4.1 Physico-chemical characterization

The aim of the investigation was to assess whether oxy-resveratrol alone or encapsulated into polymeric nanoparticles would modulate the release of proinflammatory cytokines by human DCs. Firstly, we prepared PLGA nanoparticles loaded with oxyresveratrol via single emulsion evaporation method. Thus, we obtained PLGA nanoparticles embedding oxyresveratrol showing a diameter quite similar to the one of empty nanoparticles, with an average size of 169.6 ± 3.5 and a polydispersity index (PDI) of 0.06 ± 0.02 . The encapsulation of oxy-resveratrol did not affect the size and size-distribution of the nanoparticles, but rather it made the ζ -potential less negative (-7.1 ± 0.5 mV) than the one of empty nanoparticles (-9.6 ± 0.4 mV) (Table 2); despite this slight difference, oxy-resveratrol loaded nanoparticles showed a good colloidal stability as well. The encapsulation efficiency for these nanoparticles was found to be close to 45% \pm SD (43.75 ± 3.1 % and 45.47 ± 4.55 % calculated by the direct and the indirect approach); very similar values, within the experimental error, were obtained using a direct method, based on the quantification of the oxyresveratrol loaded on the nanoparticles, and with the indirect method, where the bound fraction was estimated as the difference between the total amount added in the reaction buffer and the unloaded fraction still remaining after the reaction and the two sequent washing steps.

Table 2. Dynamic light scattering and ζ -potential data of unloaded (Empty PLGA) and oxyresveratrol-loaded (PLGA[Oxy]) nanoparticles. The results are expressed as the mean value \pm SD of three independent measures on three replica samples.

Nanoformulation	Particles size (nm)	Polydispersity Index	ζ -potential (mV)
Empty PLGA	170.2 ± 2.5	0.05 ± 0.04	-9.6 ± 0.4
PLGA[Oxy]	169.6 ± 3.5	0.06 ± 0.02	-7.1 ± 0.5

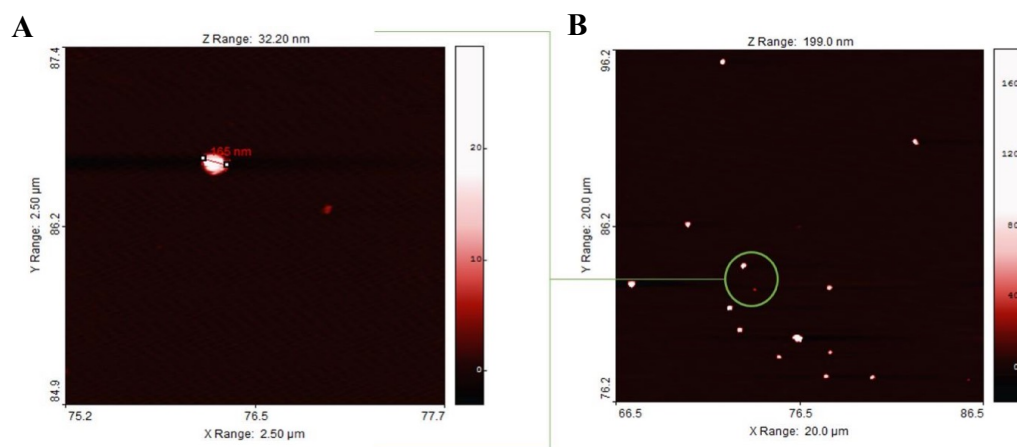


Figure 5. AFM image of a single oxyresveratrol-loaded PLGA nanoparticle with a resolution of 2.5x2.5 μm (A). Image of several single loaded nanoparticles and an aggregate with a resolution of 20X20 μm (B). The images were collected in intermittent mode.

Nanotracking and atomic force microscopy (AFM) analysis were also performed to further investigate the size distribution. Figure 5 shows nanoparticles with spherical shape; moreover, even if the techniques were based on different physico-chemical properties, data obtained by the three methods (table 3) are in agreement and in the same order of magnitude.

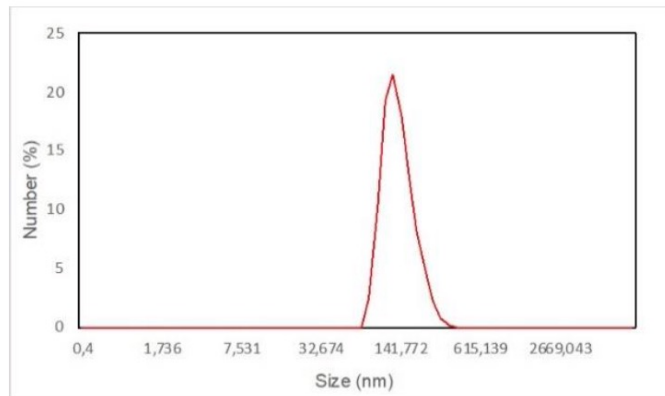
Table 3. Comparison between DLS, AFM and Nanosight tracking analysis data for empty and oxyresveratrol-loaded nanoparticles.

Nanof ormulation	Z-average (nm)	Peak number (nm)	AFM diameter* (nm)	NTA distribution (nm)
Empty PLGA	170.2 ± 2.5	148.3 ± 43.0	165 ± 34.5	140.8 ± 25.0
PLGA(Oxy)	169.6 ± 3.5	140.5 ± 42.9	171.0 ± 58.7	139.3 ± 26.7

*The statistical analysis was performed over a population major than 100 particles using SPIP™ statistical tool.

In addition, Nanosight diagram confirmed the monodispersed trend observed by dynamic light scattering (figure 6).

A



B

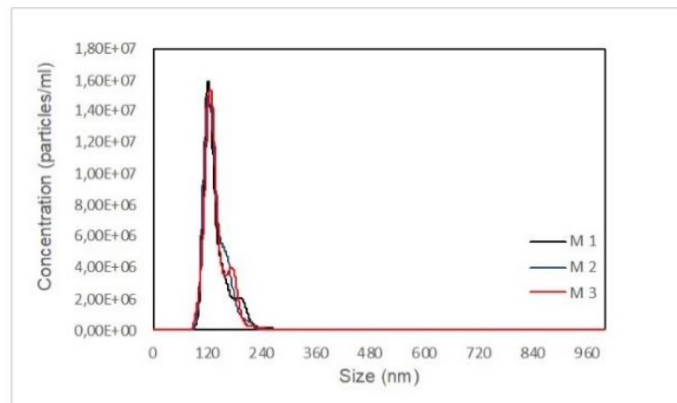


Figure 6. Comparison between DLS (A) and NTA (B) diagram. All the experiments were performed in triplicate.

1.4.2 Spectroscopy studies

The presence of oxyresveratrol in the PLGA nanoformulation was assessed by fluorescence spectroscopy. Figure 7a shows the emission pattern of loaded and empty nanoparticles: upon excitation at 335 nm, oxyresveratrol loaded nanoparticles exhibited a fluorescence spectrum different than the one shown by empty nanoparticles. Figure 7b illustrates that the emission peak close to 410–420 nm of oxyresveratrol encapsulated in PLGA nanoparticles overlapped the emission spectrum of the free polyphenol in DMSO, and both these data are indicative of effective entrapment of oxyresveratrol into PLGA nanoparticles. The observed red-shift trend was probably due to an interaction with the hydrophobic part of the polymer that could affect the emission pattern.

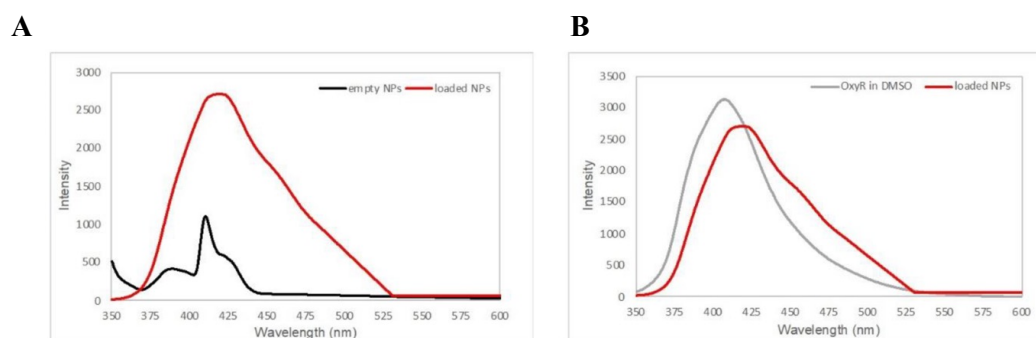


Figure 7. (A) Emission spectra of empty PLGA nanoparticles (black line) and oxyresveratrol-loaded PLGA nanoparticles (red line) collected in phosphate buffer saline pH 7.4. (B) Overlapping between free oxyresveratrol emission pattern in DMSO (grey line) and oxyresveratrol encapsulated in PLGA nanoparticles (red line) in phosphate buffer saline pH 7.4.

1.4.3 Release pattern

Finally, we investigated whether PLGA nanoparticles released oxyresveratrol at various time points and temperatures (4 and 37 °C) by UV-Visible spectroscopy to understand the release profile over time in preserving conditions (4 °C) and at the temperature used during the interaction with DCs. We found that oxyresveratrol-loaded nanoparticles exhibited an initial burst release in the first four hours with a sustained trend in the next 28 h, reaching a value of 64% in 32 h (figure 8). As expected, the trends at different temperatures were similar, even if the increase in temperature led to a curve with an enhanced slope.

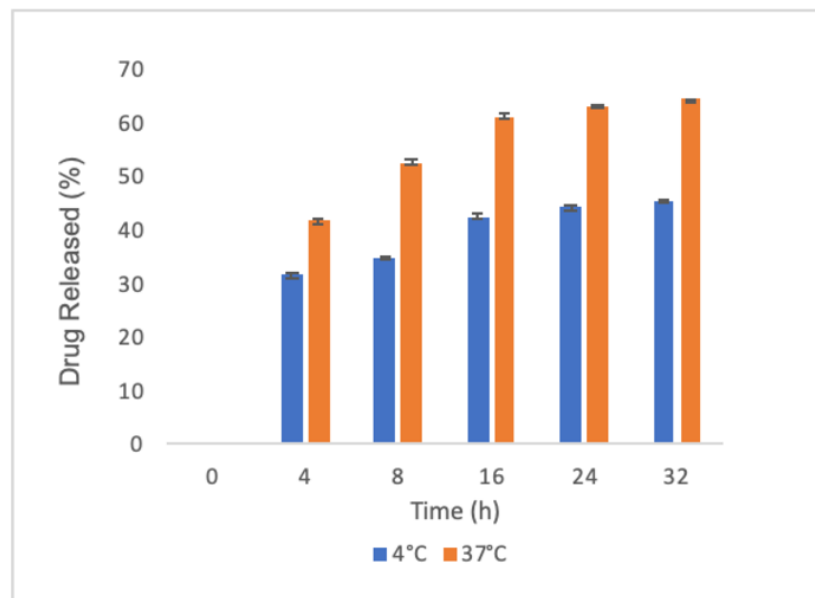


Figure 8. Oxyresveratrol release by PLGA nanoparticles: average cumulative data at 4 °C (blue bars) and 37 °C (orange bars) in phosphate buffer saline pH 7.4; each sample was collected at the indicated time points. Data were acquired in triplicate and are expressed as the mean value \pm SD.

1.4.4 In vitro studies

PLGA is a safety polymer, FDA approved for application in drug delivery⁵⁵. Nevertheless, to exclude any toxic effects we assessed whether oxyresveratrol embedding PLGA nanoparticles would affect the DC viability. To mimic viral infection condition, we also challenged the cells with R848, a molecule binding the toll like receptors TLR7 and TLR8^{87,88}. Instead, interaction between nanostructure and cells could change in presence of inflammation or viral infection⁷². For this purpose, DCs were treated with oxyresveratrol-loaded PLGA nanoparticles and compared to empty nanoparticles and free oxyresveratrol in absence or presence of R848. 50 or 100 μ M were selected as concentrations for dosing the polyphenol. Figure 9 shows DC cells with viability close to 100% when treated with empty and loaded NPs, while a slight alteration was observed in the case of free oxyresveratrol.

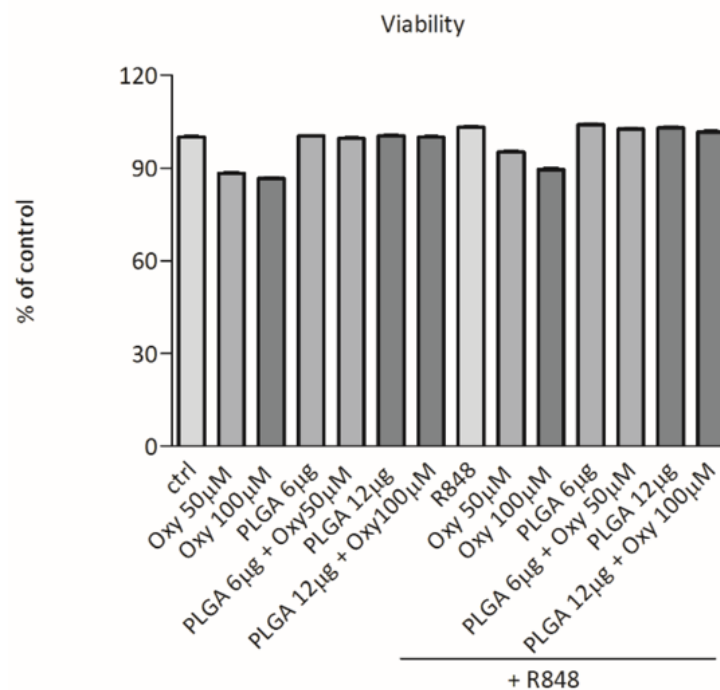


Figure 9. Effects of free oxyresveratrol and oxyresveratrol-bearing PLGA nanoparticles on DC viability. DCs were treated or not treated (ctrl) with the indicated doses of free oxyresveratrol (Oxy), unloaded PLGA nanoparticles (PLGA), or oxyresveratrol-bearing PLGA particles (PLGA + Oxy) for 24 h, followed by 1 h incubation with WST. Values are expressed as the percentage of WST reduction relative to untreated cells (designated as 100%). Data are means \pm SD of four experiments.

Thus, blood monocyte derived DCs were treated with 50 or 100 μM free oxyresveratrol, both in the absence or presence of 5 μM R848. After 24 hours, oxyresveratrol did not trigger the release of IL-12, TNF- α , or IL-6 by DCs, but inhibited the R848-induced secretion of all these pro-inflammatory cytokines (Figure 10). Marongiu *et al*⁸⁹ demonstrated that PLGA nanoparticles were efficiently internalized by human monocyte-derived DC. Thus, we investigated if oxyresveratrol was able to modulate cytokine secretion once encapsulated into PLGA nanoparticles. Firstly, we assessed the role of unloaded PLGA particles to affect the cytokine release by human DCs. Figure 10 shows that the incubation of resting DCs with 6 or 12 μg of empty nanoparticles did not trigger cytokine release. However, unloaded PLGA NPs dose-dependently increased the cytokine secretion by R848-stimulated DCs (Figure 10). Without any stimuli, same results were collected when oxyresveratrol was encapsulated in PLGA NPs. Interestingly, oxyresveratrol encapsulated into PLGA nanoparticles significantly inhibited the synergistic effect of PLGA and R848 in the induction of IL-12, TNF- α and IL-6 release by DC (Figure 10).

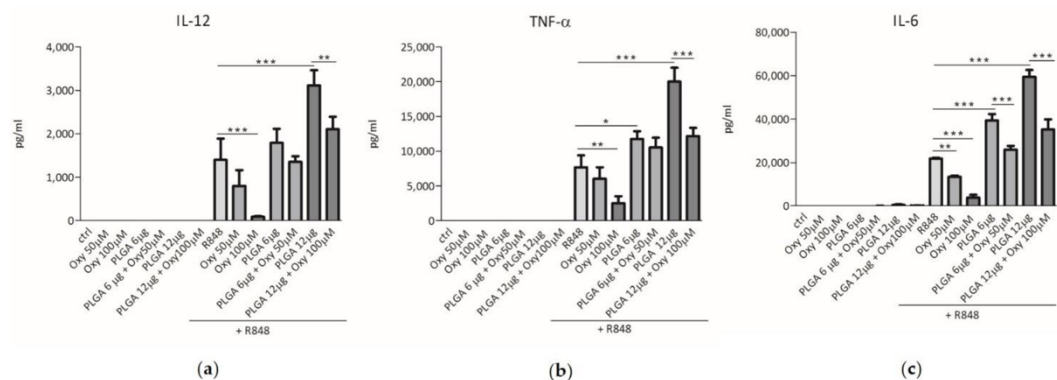


Figure 10. Effects of free or PLGA-conjugated oxyresveratrol on pro-inflammatory cytokine release by human dendritic cells (DCs). DCs were treated for 24 h with the indicated doses of free oxyresveratrol (Oxy), bare PLGA nanoparticles (PLGA) or oxyresveratrol-bearing PLGA nanoparticles (PLGA + Oxy). All the treatments were conducted in the absence or presence of 5 μM R848. The release of IL-12 (a), TNF- α (b) and IL-6 (c) in culture supernatants was evaluated by ELISA assay. The results are expressed as the mean value \pm SD of four independent experiments. * p < 0.05, ** p < 0.01 *** p < 0.001 by two-way ANOVA followed by Bonferroni post-test.

1.5 Discussion

Many attempts have been made to identify new molecules able to blunt the inflammatory response in absence of the harmful side-effects frequently observed following administration of the currently used glucocorticoids and non-steroid anti-inflammatory drugs ^{90,91} Oxyresveratrol is a polyphenol derived from a plant, *Artocarpus lakoocha* Roxb. (Moraceae), which has been used in Thai traditional medicine as an antioxidant and to treat inflammatory and parasitic diseases ^{92,93} Recently, many studies have been performed to investigate the pharmacological effects of oxyresveratrol: in particular, it has been reported to suppress lipopolysaccharide-induced inflammatory response in murine models ^{94,94} and to exert its anti-inflammatory effects mainly by downregulating the release of various cytokines ⁸²⁻⁸⁵. The reason for the anti-inflammatory action of oxyresveratrol could be related to similarity in structure and properties with estrogens. The polyphenol can act as an agonist of estrogen receptors (ERs), which are well-known players in modulating inflammation. ER-oxyresveratrol binding could trigger a series of mechanisms responsible for NF- κ B signaling pathway attenuation at both the transcriptional and translational levels, thus reducing the release of pro-inflammatory cytokines ⁸⁴.

In this scenario, we demonstrated an anti-inflammatory activity of the polyphenol by suppressing secretion of IL-12, TNF- α and IL-6 when human DCs were stimulated with R848, an agonist of TLR 7 and TLR 8 which recognize single stranded RNA viruses such as Influenza, Sendai, Coxsackie B, HIV and HCV ^{87,88} Therefore, cell stimulation with R848 mimics the natural interaction between DCs and some pathogen viruses, and the results obtained suggest that oxyresveratrol could be a good tool to mitigate the inflammatory response elicited by these microorganisms. It is worth to emphasize that here we show that oxyresveratrol inhibited the R848-induced secretion of cytokines which play a fundamental role in activation of the inflammatory process. In fact, IL-12 stimulates T cells and natural killer cells to produce IFN- γ , which in turn widens the immune and inflammatory response ^{76,77} TNF- α mediates basal inflammatory events such as edema, leukocyte adhesion to

epithelium, oxidative stress, and fever ⁶¹ and IL-6 activates, among others, acute phase responses, B lymphocyte maturation, and T cell functions ⁷⁹. Therefore, oxyresveratrol might be employed to treat autoimmune and chronic inflammatory diseases, such as Crohn's disease, psoriasis, multiple sclerosis, asthma, Crohn's disease, Alzheimer's diseases and rheumatoid arthritis, where IL-12, TNF- α , and IL-6 have been found to play an important role ⁹⁵⁻⁹⁸.

Although oxyresveratrol has wide potential benefit to the human health ^{84,92,94,99,100}, the hydrophobic nature severely limits its use. Thus, to improve bioavailability and stability, we encapsulated the polyphenol into PLGA NPs. The embedded nanoparticles showed size range lower than 200 nm which could improve the circulating time after administration. Additionally, nanoparticles bigger than 100 nm are rapidly eliminated by kidneys ²³. According to the AFM results, PLGA[Oxy] were nanosphere-like with a smooth and pore-free surface, in which oxyresveratrol is immersed in a polymeric matrix. However, further TEM analyses should be performed to further investigate the internal arrangement. No differences with empty nanoparticles were observed, confirming that loading did not affect both size and morphology. Probably, the small size of oxyresveratrol and its hydrophobic nature do not perturb the nanostructure. ζ -potential is strongly related to the surface properties: the difference we observed in the loaded nanoparticles could be due to the presence of some oxyresveratrol molecules on the surface which influence the surface charge. Furthermore, this could be the reason behind the initial burst release observed within 4 hours (Figure 8).

Then, we investigated if the polyphenol could exert the anti-inflammatory activity once encapsulated in PLGA nanoparticles. Thus, we prepared empty and oxyresveratrol-loaded PLGA NPs showing similar dimensions, both resulting in a monodispersed trend in phosphate buffer saline and having good colloidal stability. The encapsulation efficiency was close to 45%, and the release of oxyresveratrol by nanoparticles at 37 °C reached 64% in 32 h, ensuring to oxyresveratrol a good bioavailability in the 24 h of exposure to dendritic cells. In fact, providing an

adequate and constant concentration over time, positively influences the effect of a bioactive compound because of the increase in bioavailability. Additionally, PLGA nanoparticles prepared in this work, could be used to successfully delivery ox-yresveratrol inside DCs, as it has been demonstrated by confocal analysis ⁸⁹.

The use of nanoparticles for medical purposes is often hampered by unwanted activation of immune cells, leading to pro-inflammatory effects and adverse reactions such as fever, allergy, or autoimmunity^{72,101,102}. We demonstrated that both empty and loaded nanoparticles do not elicit any cytokine release by resting DCs, suggesting that these particles are biologically inert. However, empty PLGA enhanced the cytokine release triggered by DCs stimulated with R848. This unexpected result might be due to the ability of PLGA nanoparticles to interact with unknown cellular targets able to cooperate with TLR7- and TLR8-dependent pro-inflammatory signals. As an alternative, the activation of phagocytosis mechanisms to engulf the PLGA particles might elicit pathways which collaborate with those induced by R848 to enhance cytokine release. This synergistic phenomenon, called “cell priming”, is characterized by the ability of some agents to induce an hyper-responsiveness of leukocytes to other stimuli if simultaneously or consequently added ^{103,104}. For instance, it has been reported that simultaneous addition of LPS and porous silicon-TiO₂ microparticles was much more effective than stimulation with LPS alone to induce IL-12 and TNF- α secretion by human DCs ¹⁰⁵. Nevertheless, ox-yresveratrol inside PLGA nanoparticles blunted the nanoparticle-dependent enhancement of cytokine release by R848 treated DCs, indicating that this polyphenol maintains its anti-inflammatory properties also once conjugated to a nanostructure.

1.6 Conclusion

Free oxyresveratrol shows a great susceptibility to human metabolism, leading to the production of intermediate forms with reduced pharmacokinetics, and therefore, biological efficacy¹⁰⁶. Encapsulation into PLGA Nanoparticles not only solves the bioavailability problem, but also could protect oxyresveratrol from metabolism, thus increasing its pharmacokinetic and efficacy¹⁰⁷. However, the primary aim of this study was to emphasize the advantage of including oxyresveratrol in the design of PLGA-based nanocarriers to avoid undesired priming-related consequences.

PLGA nanoparticles having no apparent intrinsic pro-inflammatory activity, triggered pro-inflammatory events when co-administered in presence of a stimulus simulating virus infection. Furthermore, oxyresveratrol not only can act as anti-inflammatory agent, turning down pathogen-induced inflammatory events, but it can also reduce an eventual synergistic effect between nanoparticles and products of microorganisms when it is enclosed into such nanoparticles. Thanks to the narrow size distribution, retain ability and colloidal stability, PLGA could be successfully used to delivery plant-derived molecules in order to modulate pro-inflammatory activity of DCs. For instance, PLGA-associated α -bisabolol, a natural sesquiterpene found in the oil of *Matricaria chamomilla*, decreased the secretion of cytokines by lipopolysaccharide (LPS)-stimulated human DCs, as it was demonstrated in Marongiu, L. *et al*⁸⁹.

Although the mechanism by which oxyresveratrol inhibits the secretion of cytokines by human DCs remains to be clarified, the polyphenol entrapped into nanoparticles can contrast an unwanted synergistic effect of nanoparticles with microorganisms present in the patient tissues, “priming effect”, overcoming a condition unfavorable to administration in biological systems. Nevertheless, these results suggest the importance of an accurate testing of both loaded and unloaded nanostructures in combination with products of microorganisms to avoid unwanted side-effects once they are administered to patients.

Article

Oxyresveratrol Inhibits R848-Induced Pro-Inflammatory Mediators Release by Human Dendritic Cells Even When Embedded in PLGA Nanoparticles

Salvatore Calogero Gaglio ¹, Marta Donini ² , Piyachat Evelyn Denbaes ¹, Stefano Dusi ^{2,*}  and Massimiliano Perduca ^{1,*} 

¹ Department of Biotechnology, University of Verona, Strada Le Grazie 15, 37134 Verona, Italy; salvatorecalogero.gaglio@univr.it (S.C.G.); piyachat@live.com (P.E.D.)

² Department of Medicine, Section of General Pathology, University of Verona, Strada Le Grazie 8, 37134 Verona, Italy; marta.donini@univr.it

* Correspondence: stefano.dusi@univr.it (S.D.); massimiliano.perduca@univr.it (M.P.); Tel.: +39-045-802-7124 (S.D.); +39-045-802-7984 (M.P.)



Citation: Gaglio, S.C.; Donini, M.; Denbaes, P.E.; Dusi, S.; Perduca, M. Oxyresveratrol Inhibits R848-Induced Pro-Inflammatory Mediators Release by Human Dendritic Cells Even When Embedded in PLGA Nanoparticles. *Molecules* **2021**, *26*, 2106. <https://doi.org/10.3390/molecules26082106>

Academic Editors: Filomena Barreiro and Isabel P. Fernandez

Received: 15 March 2021

Accepted: 3 April 2021

Published: 7 April 2021

Publisher's Note: MDPI stays neutral with regard to jurisdictional claims in published maps and institutional affiliations.



Copyright: © 2021 by the authors. Licensee MDPI, Basel, Switzerland. This article is an open access article distributed under the terms and conditions of the Creative Commons Attribution (CC BY) license (<https://creativecommons.org/licenses/by/4.0/>).

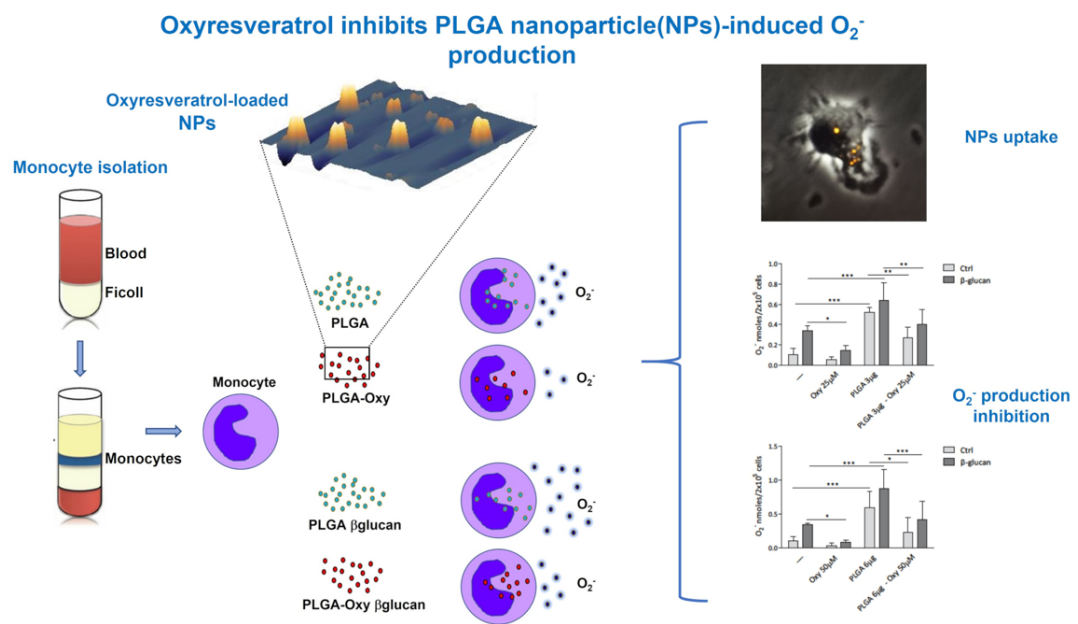
Abstract: Oxyresveratrol, a stilbene extracted from the plant *Artocarpus lakoocha* Roxb., has been reported to provide a considerable anti-inflammatory activity. Since the mechanisms of this therapeutic action have been poorly clarified, we investigated whether oxyresveratrol affects the release of the pro-inflammatory cytokines IL-12, IL-6, and TNF- α by human dendritic cells (DCs). We found that oxyresveratrol did not elicit per se the release of these cytokines, but inhibited their secretion induced upon DC stimulation with R848 (Resiquimod), a well-known immune cell activator engaging receptors recognizing RNA viruses. We then investigated whether the inclusion of oxyresveratrol into nanoparticles promoting its ingestion by DCs could favor its effects on cytokine release. For this purpose we synthesized and characterized poly(lactic-co-glycolic acid) (PLGA) nanoparticles, and we assessed their effects on DCs. We found that bare PLGA nanoparticles did not affect cytokine secretion by resting DCs, but increased IL-12, IL-6, and TNF- α secretion by R848-stimulated DCs, an event known as “priming effect”. We then loaded PLGA nanoparticles with oxyresveratrol and we observed that oxyresveratrol-bearing particles did not stimulate the cytokine release by resting DCs and inhibited the PLGA-dependent enhancement of IL-12, IL-6, and TNF- α secretion by R848-stimulated DCs. The results herein reported indicate that oxyresveratrol suppresses the cytokine production by activated DCs, thus representing a good anti-inflammatory and immune-suppressive agent. Moreover, its inclusion into PLGA nanoparticles mitigates the pro-inflammatory effects due to cooperation between nanoparticles and R848 in cytokine release. Therefore, oxyresveratrol can be able to contrast the synergistic effects of nanoparticles with microorganisms that could be present in the patient tissues, therefore overcoming a condition unfavorable to the use of some nanoparticles in biological systems.

Keywords: dendritic cells; oxyresveratrol; cytokines; PLGA nanoparticles; inflammation

1. Introduction

Dendritic cells (DCs) are a heterogeneous cell population endowed with the ability to phagocytose antigens present in the extracellular environment. Subsequently, DCs undergo a process of maturation which enables them to present antigens to lymphocytes, thus activating the specific immune response [1–3]. Mature DCs produce chemical mediators that modulate the adaptive immune reaction and the inflammatory process to fight cancer cells and pathogen microorganisms. Among the most important mediators secreted by DCs there is IL-12, a fundamental cytokine activating natural killer cells and T lymphocytes [4,5], as well as IL-6 and TNF- α that stimulate the immune cells and are involved in the induction of the systemic acute phase reaction characterized by fever, headache, changes in the

Oxyresveratrol-Loaded PLGA Nanoparticles Inhibit Oxygen Free Radical Production by Human Monocytes: Role in Nanoparticle Biocompatibility



Donini, M *et al*, *Molecules* 2021, 26, 4351 <https://doi.org/10.3390/molecules26144351>

2.1 Aim

In the previous chapter we described the possibilities of a nanostructure to generate an adverse inflammation response when interacting with living cells. Since most of the time inflammation and oxidative stress are bounded trend, we analysed the impact on the Reactive Oxygen Species generation by PLGA nanoparticles after being internalized by cells. Belonging to the cluster of polyphenols, oxyresveratrol has been reported to be an antioxidant and an oxygen-free radical scavenger⁹⁹. However, no investigations have been performed to assess whether oxyresveratrol inhibits ROS production in human leucocytes, which are able to produce high amounts of oxygen radicals when activated by pathogenic microorganisms⁷⁵⁻⁷⁷. Thus, we examined whether oxyresveratrol was able to contrast oxidative damage even when encapsulated into PLGA NPs.

2.2 Introduction

Monocytes are a heterogeneous cell population initiating and propagating the immune response to pathogenic microorganisms. These cells can freely circulate in the bloodstream and pass into the tissues, where they may differentiate into resident macrophages. During inflammation, the quantity of extravasated monocytes increases to amplify the local immune response through cytokine release and phagocytosis of foreign microorganisms⁷². Upon pathogen uptake, monocytes produce reactive oxygen species (ROS)⁷³. The main source of ROS in monocytes is the NOX2 NADPH oxidase, a multicomponent enzyme which transfers electrons to molecular oxygen to generate superoxide anion (O^{2-})^{76,77}. ROS play an important role in defences against infections^{74,76,77}, but they may also damage the cells by causing oxidative stress, which is responsible for several diseases, such as cancer, hypertension and neurological disorders¹⁰⁸.

Firstly, we investigated a potential oxyresveratrol effect on the generation of superoxide anion (O^{2-}) by human monocytes, which are powerful reactive oxygen species producers. Subsequently, PLGA[Oxy] nanoparticles have been tested as well. Even in this case of study, oxyresveratrol embedding with PLGA NPs significantly inhibited the O^{2-} production elicited by unloaded nanoparticles in resting monocytes as well as the synergistic effect of nanoparticles and β -glucan. Our results indicate that oxyresveratrol can inhibit ROS production by activated monocytes, and its inclusion into PLGA nanoparticles mitigates the oxidative effects due to the interaction between these nanoparticles and resting monocytes. Moreover, oxyresveratrol is able to protect neurons^{100,109–111}, human lens epithelial cells¹¹² and hepatocytes¹¹³, reduces adverse effects of nicotine¹¹⁴ and mitigates DNA damage by mechanisms involving inhibition of ROS generation¹¹⁵. The anti-oxidant activity is mainly due to a decrease in the production of the free radical nitric oxide, which can cause cell injury in many inflammatory diseases, in RAW264.7 murine macrophage cell line^{106,116}.

Several natural molecules show beneficial activity to human health. Since they suffer from poor solubility in an aqueous environment with a consequent low bioavailability, their use as active principles is highly restricted¹¹⁷. Additionally, they show chemico-physical instability due to environmental stress such as oxidation. On the one hand, nanoencapsulation technologies can overcome this issue by increasing solubility and, on the other hand, by providing protection to the payload. Several examples of bioactive molecule nano size formulations are present in literature; some examples are: resveratrol, a natural polyphenol with a broad spectrum of pharmacological activities showing enhanced action against cardiovascular diseases when embedded in nanoformulations¹¹⁸; quercetin, a plant flavonoid whose efficacy as an antitumoral molecule is limited by its low solubility and consequent low bioavailability, greatly enhanced using nanocarriers¹¹⁹; curcumin, another natural phenolic compound derived from the rhizome of *Curcuma longa*, proven to have many pharmacological activities and whose embedding in polymeric nanoparticles increases its oral bioavailability¹²⁰.

PLGA, as a biodegradable polymer, has been widely used to improve the therapeutic effect of various soluble/insoluble drugs, reducing the risk of unwanted side effects for patients. In fact, PLGA shows a very low or absent toxicity since it is degraded by cells into nontoxic compounds (lactic and glycolic acids)⁶⁰ However, upon administration to patients, nanoparticles interact with the cells of the immune system which can react against these materials, producing proinflammatory mediators which lead to adverse events, such as inflammation and allergy³⁸.

Thus, we investigated whether encapsulation with oxyresveratrol could make nanoparticles safer by reducing oxidative stress damage.

2.3 Experimental section

Materials. RPMI 1640 and low-endotoxin FBS were obtained from Lonza (Walkersville, MD, USA); flow cytometric analysis was performed using mouse anti-human antibody CD14 (M5E2) (Biolegend, San Diego, CA, USA).

PLGA (poly[DL-lactide-co-glycolide], CAS 26780-50-7), PVA (poly[vinyl alcohol], CAS 9002-89-5), acetone (1.00013), dimethyl sulfoxide (DMSO, D-5879), oxyresveratrol (91211) and β -glucan from baker's yeast were purchased from Sigma-Aldrich (St. Louis, MO, USA).

Preparation of PLGA nanoparticles. The PLGA nanoparticles embedded with oxyresveratrol used in this study were prepared as previously described³⁸. Briefly, 10 mg of the 50:50 lactide–glycolide ratio PLGA polymer and 5 mM (1.22 mg) of oxyresveratrol were co-dissolved in 1 mL of organic solvent (95% acetone and 5% DMSO); the obtained organic phase was added dropwise under stirring (2000 RPM) to 10 mL of 1% polyvinyl alcohol (PVA) aqueous solution and left overnight to evaporate the organic phase. Nanoparticles were collected and washed by centrifugation (Eppendorf Centrifuge 5804R) at 4 °C for 20 min. The purified nanoparticles were re-suspended in 1 mL of phosphate buffer saline (PBS) solution pH 7.4 and stored at 4 °C. Empty PLGA nanoparticles were prepared with the above-described protocol without the addition of oxyresveratrol to the organic phase.

Fluorescence responsive PLGA nanoparticles were prepared by loading them with rhodamine B. In details, 10 mg of PLGA and 0.041 mM (0.25 mg) of rhodamine B were dissolved in 1 mL of organic mixture (acetone:DMSO) with ratio 87:13. The following steps were the same as those described above.

Size and ζ -Potential Characterization. Size and ζ -potential of PLGA nanoparticles were estimated at 25 °C using a Nano Zeta Sizer ZS (ZEN3600, Malvern Instruments, Malvern, Worcestershire, UK). Samples resuspended in PBS, being used as a stock suspension, were diluted 10 times in PBS for size measurements and into

10 mM NaClO₄ pH 7.5 for ζ-Potential measurements, to obtain a final concentration of 1 mg/mL for the nanoformulations. Data were collected in triplicate and analyzed by the ZetaSizer 7.10 software (Malvern, Worcestershire, UK).

Spectroscopic Studies, Encapsulation Efficiency and Release Evaluation. To assess the presence of oxyresveratrol inside our nanoparticles the emission pattern was recorded upon excitation at 335 nm, the absorption wavelength of the polyphenol, by using a Jasco Spectrofluorometer FP-8200 (Easton, MD, USA).

To quantify the amount of the entrapped oxyresveratrol (Encapsulation Efficiency), a direct method was used. PLGA[Oxy] NPs were dissolved in DMSO and the obtained solution was analyzed using a calibration curve (Figure 4). Encapsulation efficiency was estimated using the following Equation (1):

$$(1) EE(\%) = \frac{OxyR_{loaded}}{OxyR_{fed}} \times 100$$

To confirm these data, a second method has been employed as well: waste supernatants from the nanoparticle preparation were collected and analyzed by comparing data to a second calibration curve obtained in Milli-Q water (Figure 4). The value of loaded oxyresveratrol (OxyR_{loaded}) was indirectly estimated by the following Equations (2) and (3) and finally EE was calculated as described above.

$$(2) OxyR_{loaded} = OxyR_{fed} - OxyR_{lost}$$

$$(3) OxyR_{loaded} = OxyR_{supernatant} + OxyR_{wash1} + OxyR_{wash2}$$

To assess the ability of the nanoparticles to retain oxyresveratrol over the time, a release study was performed in 1 mL of PBS pH 7.4 at 4 and 37 °C. Samples were collected at different time intervals and replaced with an equal volume of media to maintain the sink condition. The released OxyR was quantified using a calibration curve obtained by UV-Visible spectroscopy at 335 nm.

Spectroscopic Studies, Encapsulation Efficiency and Release Evaluation. To assess the presence of dye molecules inside our nanoparticles, the emission pattern was recorded upon excitation at 555 nm, which is a suitable excitation wavelength for rhodamine B. To quantify the amount of the entrapped dye (encapsulation efficiency), a direct method was used: PLGA nanoparticles embedding rhodamine B were dissolved in DMSO and the obtained solutions were analyzed at 555 nm. Results were compared to a previously prepared calibration curve (Figure 11). Encapsulation efficiency was estimated using the following equation:

$$(1) EE(\%) = \frac{dye_{loaded}}{dye_{fed}} \times 100$$

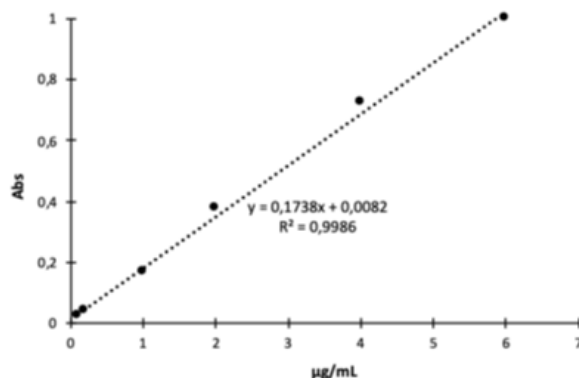


Figure 11. Calibration curve of Rhodamine B in DMSO.

Monocytes Preparation and Culture. After written informed consent and upon approval of the ethical committee (Prot. N. 5626, 2 February 2012; Prot. n. 57182, 16 October 2019), buffy coats from the venous blood of normal healthy volunteers were obtained from the Blood Transfusion Centre of the University of Verona. Peripheral blood mononuclear cells were isolated by Ficoll-Hypaque and Percoll (GE Healthcare Life Science) density gradients and used as a source for immunomagnetic isolation of CD14 positive cells (Miltenyi Biotec GmbH, Auburn, CA, USA). The purity of CD14+ cells was always greater than 98%, as determined by flow cytometry.

Quantification of O²⁻ Production. Monocytes stimulated with 5 µg/mL β-glucan or not were treated with oxyresveratrol alone or encapsulated in PLGA nanoparticles, or with corresponding amounts of bare PLGA particles for 18 h, and then the O²⁻ release was estimated by cytochrome c reduction. Briefly, after culturing the cells for the required time, the medium of each well was replaced with HBSS pH 7.4, containing 80 µM ferricytochrome c type III (Sigma-Aldrich, St. Louis, MO, USA), with or without 5 µg/mL of β-glucan (Sigma-Aldrich, St. Louis, MO, USA). Cytochrome c reduction was evaluated at 550 nm, using an automated microplate reader (Bioteck® Instruments Inc., Winooski, VT, USA).

Cell Viability Evaluation. Cell viability was assessed using the Cell Proliferation Reagent WST-1 assay (Roche Diagnostics GmbH, Mannheim, Germany) according to the manufacturer's instructions. Monocytes resting or activated with β-glucan were treated with oxyresveratrol alone or encapsulated in PLGA nanoparticles, or with corresponding amounts of unloaded PLGA particles for 18 h. After treatment, the cell supernatant was removed and 50 µL of pre-warmed fresh complete medium were added to cells and to three empty wells (blank). A 2× WST solution was freshly prepared by dilution of the 10× WST reagent in the complete medium and a volume of 50 µL was dispensed in the wells and blank. The plate was incubated for 60 min. The absorbance (OD) of the samples was measured using a Victor3 multilabel reader (PerkinElmer, Shelton, CT, USA) at 450 nm.

Immunofluorescence and Microscopy Analysis. Monocytes were seeded on cell culture chamber slide (Corning, NY, USA) and treated for 18 h with 6 µg of PLGA nanoparticles conjugated to rhodamine B. Cells were washed with PBS and fixed with 4% paraformaldehyde (Sigma-Aldrich) for 30 min at room temperature and quenched with 50 mM NH₄Cl. After washing, the coverslips were incubated for 10 min with DAPI (Sigma-Aldrich) to stain nuclei. Images were acquired with a wide field Zeiss AxioImager Z.2 deconvolution microscopy setting (Carlo Zeiss, Germany), equipped with Colibri 7 fluorescent LED illumination, motorized 3D scanning stage and Hamamatsu ORCA-Flash4.0 V3 Digital CMOS camera, set at 8

output bit depth; 512×512 pixel ROIs were acquired with a $100\times$ Plan Aplanachromatic oil immersion objective (AN 1.46). Each field was acquired with bright field illumination and double fluorescent light illumination (385/30 nm ex. for DAPI and 555/30 nm ex. for DsRed). Automatic 3D image scanning was according to the Nyquist–Shannon sampling theorem, using the inline ZEN 2.6 Nyquist Calculator. Three-dimensional scans were then processed with Zeiss ZEN 2.6 by applying the advanced Zeiss deconvolution (DCV) module. Image deconvolution was achieved by applying the constrain iterative algorithm. Spectral linear unmixing was, finally, applied to remove overlapped spectral components and background noise. Deconvolved and unmixed 3D stacks were rendered and analyzed with the ZEN 2.6 Arivis 3D module.

Statistical Analysis. Data are expressed as means \pm SD. Statistical analyses, including two-way ANOVA followed by Bonferroni post-test, were performed with GraphPad Prism 5 (GraphPad Software, Inc., San Diego, CA, USA).

**All the in vitro experiment has been performed thanks to Prof Dusi's Lab,
Department of Medicine, Section of General Pathology**

2.4 Results

2.4.1 Physico-chemical characterization

To prepare empty and oxyresveratrol-loaded PLGA nanoparticles, we used the same protocol described in the previous chapter ³⁸. The reproducibility of the method was again confirmed since particle size and ζ -potential were completely comparable to those previously characterized ³⁸. To investigate the uptake kinetics of PLGA nanoparticles by monocytes, we encapsulated the fluorescence-responsive rhodamine B dye (PLGA[Rhod]). As illustrated in Table 4, dye molecule slightly increased the hydrodynamic radius in comparison to PLGA and PLGA[Oxy], with an average size of 209.2 ± 0.6 nm. However, size-distribution showed a monodisperse trend, as is demonstrated by the low PDI value exhibited by all the different preparations. The ζ -potential measured at pH 7.5 of dye-loaded nanoparticles appeared to be more negative (-18.2 ± 1.4 mV) compared to the PLGA[Oxy] (-7.1 ± 0.5 mV) and PLGA nanoparticles (-9.6 ± 0.4 mV). Finally, all the different nanoformulation exhibited a good colloidal stability thank to stabilization by charge.

Table 4. DLS data and ζ -potential of empty (PLGA), oxyresveratrol (PLGA[Oxy]) and rhodamine B loaded (PLGA[Rhod]) nanoparticles. The results are expressed as the mean value \pm SD of three independent measures on three replica samples.

Nanoformulation	Particles size (nm)	Polydisperse Index	ζ -potential
PLGA	170.2 ± 2.5	0.05 ± 0.03	-9.6 ± 0.4
PLGA[Oxy]	169.6 ± 3.5	0.05 ± 0.02	-7.1 ± 0.5
PLGA[Rhod]	209.2 ± 0.6	0.06 ± 0.02	-18.2 ± 1.4

2.4.2 Spectroscopy studies

The presence of the dye in the PLGA nanoformulations was assessed by fluorescence spectroscopy. Figure 12 shows the emission pattern of PLGA[Rhod]: you can see that upon excitation at 555 nm dye-loaded nanoparticles exhibited the fluorescence pattern typical of the free dye. Furthermore, the amount of encapsulated dye was calculated dissolving the PLGA[Rhod] in dimethyl sulfoxide (DMSO) to enhance nanostructure disassembling: then, the values obtained by absorbance spectroscopy were used in the calibration line equation. We obtained nanoparticles carrying a total dye amount of 12.18 μg of rhodamine B per mg of PLGA with an encapsulation efficiency of $48.97 \pm 0.33 \%$.

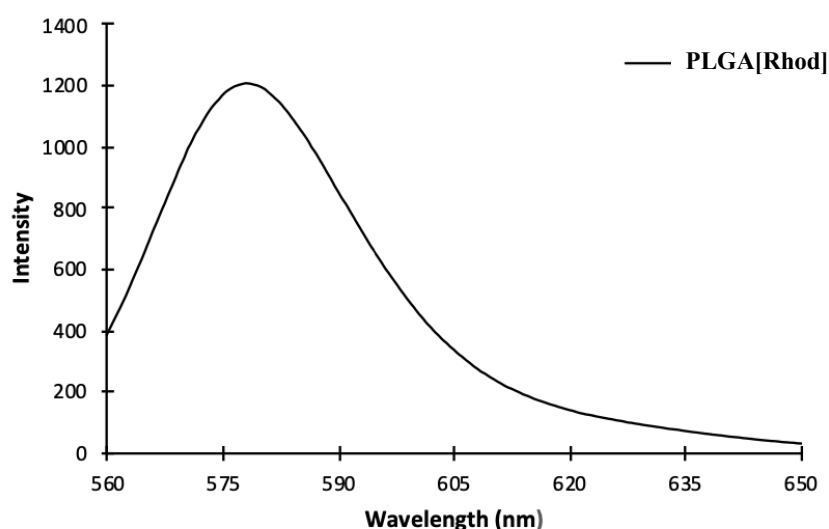


Figure 12. Emission spectrum of rhodamine B-loaded PLGA nanoparticles, collected in phosphate buffer saline pH 7.4, when excited at 555 nm. The emission maximum is approximately 578 nm. Data are means of three independent measures on three replica samples.

2.4.3 In vitro studies

Firstly, we verified the non-toxic effects of free and loaded oxyresveratrol on the viability of human monocytes. As it was done for DCs, monocytes were treated with free oxyresveratrol (Oxy), unloaded PLGA or PLGA[Oxy] in the absence or presence of β -glucan, and cell viability was assessed using the Cell Proliferation Reagent WST-1 assay. Figure 13 shows that under these experimental conditions the viability of monocytes was not or was only slightly altered.

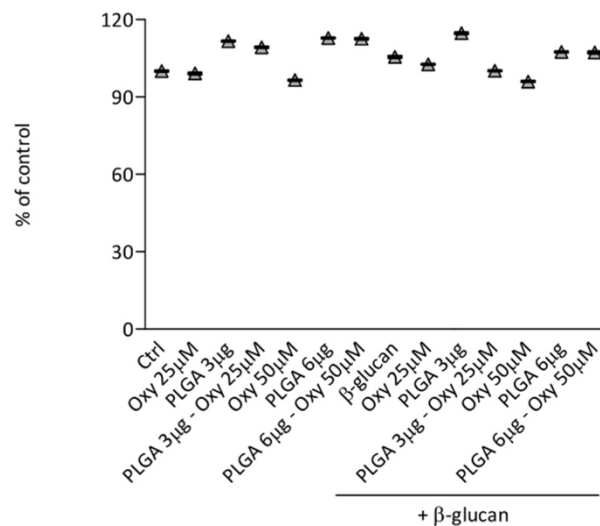


Figure 13. Effects of free oxyresveratrol and oxyresveratrol-bearing PLGA nanoparticles on the viability of monocytes. Monocytes were treated with the indicated doses of free oxyresveratrol (Oxy), unloaded PLGA nanoparticles (PLGA) or oxyresveratrol-loaded PLGA particles (PLGA[Oxy]) for 18 h in the absence (Ctrl) or presence of 5 μ g/mL β -glucan, and then incubated for 1 h with WST. The values are expressed as the percentage of WST reduction relative to untreated cells (designated as 100%). Data are means \pm SD of four experiments.

The interaction between monocytes and pathogenic microorganisms triggers the production of ROS, which can provoke tissue damage as side effect^{108,121}. Thus, we investigated a potential anti-inflammatory activity of oxyresveratrol in decreasing the ROS production elicited by stimulation of monocytes with β -glucan, a yeast-derived molecule able to activate the immune cells^{122,123}.

For this purpose, human blood monocytes were treated with 25 μM and 50 μM free oxyresveratrol (Oxy), both in the absence (Ctrl) and the presence of 5 $\mu\text{g}/\text{mL}$ β -glucan (Figure 14). After an 18 h incubation, oxyresveratrol significantly decreased the β -glucan-induced release of O_2^- by monocytes as it has been assessed by cytochrome c reduction test (figure 14). Moreover, adding higher doses of oxyresveratrol (100 μM) did not lead to further inhibition of ROS production (results not shown).

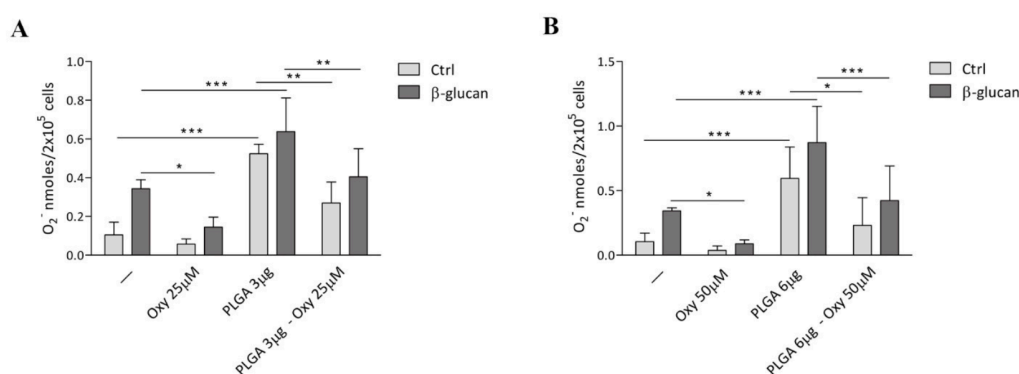


Figure 14. Effects of free or PLGA nanoparticle-conjugated oxyresveratrol on O_2^- production by human monocytes. Monocytes were treated for 18 h with 25 μM (panel (A)) and 50 μM (panel (B)) oxyresveratrol free (Oxy) or loaded on PLGA nanoparticles (PLGA[Oxy]), as well as with equivalent quantities of unloaded PLGA particles (PLGA). All the treatments were conducted in the absence (Ctrl) or presence of 5 $\mu\text{g}/\text{mL}$ β -glucan. The O_2^- production was evaluated by cytochrome c reduction. The results are expressed as the mean value \pm SD of four independent experiments. * $p < 0.05$, ** $p < 0.01$ *** $p < 0.001$ by two way ANOVA followed by Bonferroni post-test.

Subsequently, we studied whether oxyresveratrol-loaded PLGA nanoparticles could mediate ROS production as it was observed in the free form. First of all, empty particles were tested to verify if they were able to trigger O_2^- generation by human monocytes. Figure 14 shows that the incubation of resting monocytes with 3 μg (panel A) or 6 μg (panel B) of bare PLGA particles triggered O_2^- production. Moreover, empty PLGA particles significantly enhanced the O_2^- generation by β -glucan-stimulated monocytes (Figure 14 panel A and B). These results indicated that the nanoparticles elicit per se ROS production, an event probably triggered by

activation of human monocytes during the uptake of the nanoparticles ¹²⁴. Interestingly, PLGA nanoparticles enhanced the ROS generation elicited by β -glucan, indicating a synergistic action between the nanoparticles and the fungal derivative in the stimulation of O^{2-} generation. Figure 14 also shows the results of the treatment of both resting and β -glucan stimulated monocytes with 3 μ g of PLGA nanoparticles loaded with 25 μ M oxyresveratrol (panel A) or 6 μ g of PLGA nanoparticles loaded with 50 μ M oxyresveratrol (panel B). The figure 14 suggests oxyresveratrol encapsulation into PLGA nanoparticles significantly inhibited both the O^{2-} production caused by unloaded nanoparticles in resting monocytes and the synergistic effect of these particles and β -glucan.

Finally, monocytes were incubated with PLGA[Rhod] to assess their cellular uptake kinetics. Internalized particles were visualized by wide-field fluorescence deconvolution microscopy at different time points. This analysis revealed that after 18 h PLGA[Rhod] were efficiently internalized by human monocytes (Figure 15). Three-dimensional scanning reconstruction showed that the particles were localized inside the cells (not shown).

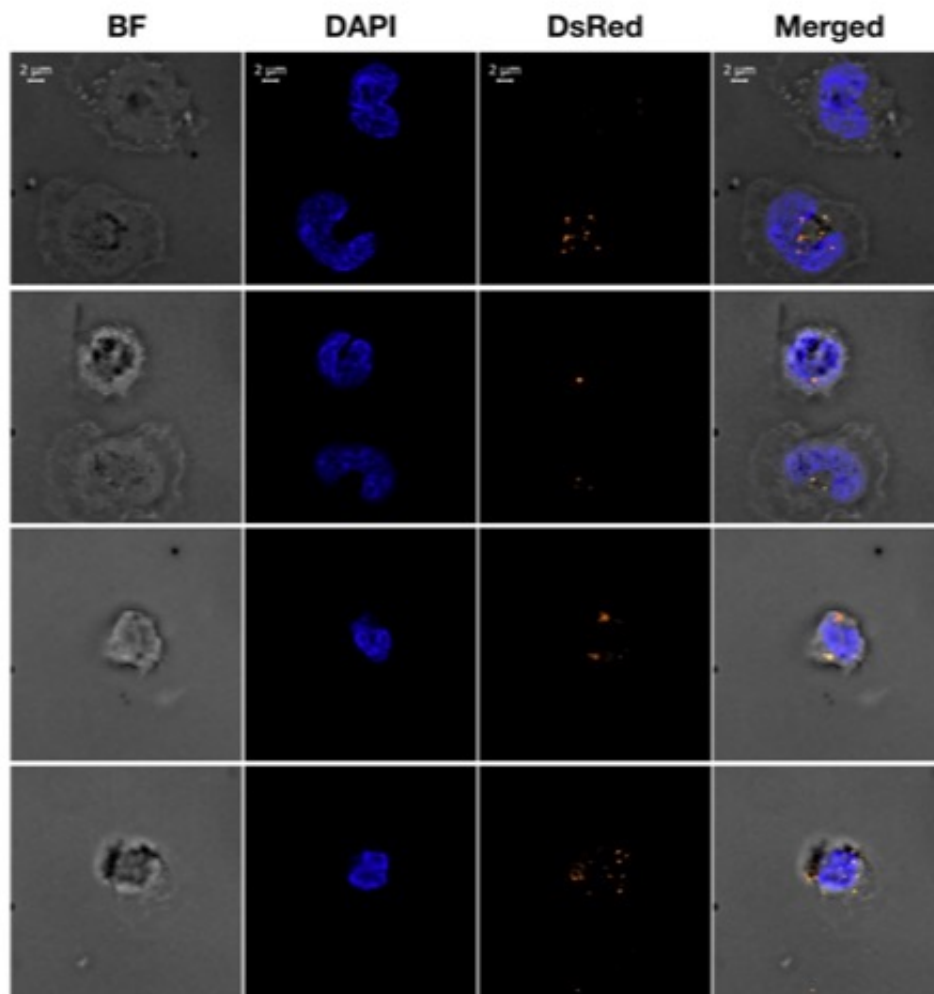


Figure 15. Internalization of PLGA nanoparticles by human primary monocytes. Shown are four representative fields (top to bottom rows) illustrating adherent human primary monocytes treated with rhodamine B-loaded PLGA nanoparticles for 18 h and co-stained with DAPI. From left to right, bright field (BF), DAPI and DsRed (rhodamine B) individual channels are shown. On the far right, merged channels are shown. Scale bar is 2 μm .

2.5 Discussion

Human monocytes have been chosen because they are able to produce large amounts of oxygen radicals through activation of the enzyme NOX2 NADPH oxidase^{121,124}. From one side, these radicals exert a defensive action¹²¹, but from the other side, they can cause oxidative tissue damage during inflammation¹⁰⁸. As far as we know, no data have been reported on the effects of oxyresveratrol on ROS generation by human monocytes. We demonstrated free oxyresveratrol decreased the O^{2-} generation by human monocytes stimulated with β -glucan, a treatment which mimics the natural interaction between pathogenic fungi and immune cells^{122,123}. Therefore, oxyresveratrol seems to act as protective agent against ROS produced by monocytes during the inflammatory process. Moreover, the anti-oxidation activity was evaluated even when the polyphenol was encapsulated in PLGA NPs. Following the same steps of the previous studies, we first tested the effect of the interaction between PLGA nanoparticles and cells.

To study cellular uptake, Rhodamine B was encapsulated to detect the nanoparticles inside the cells. PLGA[Rhod] NPs, with dimensions close to 200 nm and a negative surface charge, were suitable to mimic the interaction that would occur with the same nanoparticles of oxyresveratrol. Furthermore, the emission spectrum collected upon excitation of (the common wavelength used for detecting the dye) demonstrated that the dye was preserved during the encapsulation procedure.

According to the confocal analysis, we demonstrated that these nanoparticles undergo very efficient uptake by human monocytes. The finding that empty PLGA nanoparticles induced O^{2-} production by monocytes agreed with literature; in fact, there are proofs that once phagocytic cells are exposed to nanostructures the mechanisms behind the uptake trigger ROS production^{125–127}. Additionally, it has been verified PLGA particles can activate the production of ROS in human peripheral blood phagocytes¹²⁸. Likely, the process behind ROS generation is linked to the ingestion of nanoparticles by immune cells: the uptake of foreign materials by

phagocytes leads to activation of NADPH oxidase, which is responsible for the production of O^{2-} ¹²⁴. Interestingly, PLGA nanoparticles enhanced the ROS production induced by β -glucan in a similar synergist pattern observed for R848-stimulated dendritic cells. This “cell priming” effect is characterized by the ability of some agents, such as bacterial products, to increase the responsiveness of leukocytes to other stimuli if simultaneously or consequently added ^{103,104}. In this regard, the simultaneous addition of LPS and porous silicon-TiO₂ microparticles was more effective than incubation with LPS alone to induce IL-12 and TNF- α secretion by human DCs ¹⁰⁵. As was observed for the anti-inflammatory effect exerted on DCs, oxyresveratrol incorporated with PLGA nanoparticles significantly attenuated empty nanoparticle-activated ROS production in both resting and stimulated monocytes. The main source of ROS in monocytes is the NOX2 NADPH oxidase, which produces O^{2-} ¹²¹. The inhibition on ROS production probably depends on its action on NADPH oxidase. Moreover, several natural phenolic compounds, including celastrol, apocynin, curcumin and resveratrol, have been reported to be inhibitors of various NADPH oxidase isoforms ¹²⁹. Nevertheless, further investigations are required to clarify the mechanisms by which oxyresveratrol inhibits this enzyme.

2.6 Conclusion

To resume, oxyresveratrol is also a good antioxidant agent because it can inhibit O^{2-} production by human monocytes, which are strong producers of ROS. Interestingly, nanoparticle based on PLGA, which is generally considered to be biocompatible and harmless, could participate in the activation of oxidative events, when administered in the presence of other unexpected agents, such as pathogenic fungi or their derivatives. However, oxyresveratrol encapsulation into PLGA could solve this problem by mitigating the oxidative damage and preventing an eventual synergy between nanostructures and microbial products (cell priming).

In conclusion, from one side PLGA is a very effective molecular vehicle to carry oxyresveratrol inside immune cells, and from the other side, the payload improves the biocompatible properties of the carrier itself.

Article

Oxyresveratrol-Loaded PLGA Nanoparticles Inhibit Oxygen Free Radical Production by Human Monocytes: Role in Nanoparticle Biocompatibility

Marta Donini ¹, Salvatore Calogero Gaglio ², Carlo Laudanna ¹, Massimiliano Perduca ^{2,*} and Stefano Dusi ^{1,†}

¹ Department of Medicine, Section of General Pathology, University of Verona, Strada Le Grazie 8, 37134 Verona, Italy; marta.donini@univr.it (M.D.); carlo.laudanna@univr.it (C.L.); stefano.dusi@univr.it (S.D.)

² Department of Biotechnology, University of Verona, Strada Le Grazie 15, 37134 Verona, Italy; salvatorecalogero.gaglio@univr.it

* Correspondence: massimiliano.perduca@univr.it; Tel.: +39-045-802-7984

† These authors equally contributed.



Citation: Donini, M.; Gaglio, S.C.; Laudanna, C.; Perduca, M.; Dusi, S. Oxyresveratrol-Loaded PLGA Nanoparticles Inhibit Oxygen Free Radical Production by Human Monocytes: Role in Nanoparticle Biocompatibility. *Molecules* **2021**, *26*, 4351. <https://doi.org/10.3390/molecules26144351>

Academic Editor: Lillian Barros

Received: 29 June 2021

Accepted: 16 July 2021

Published: 18 July 2021

Publisher's Note: MDPI stays neutral with regard to jurisdictional claims in published maps and institutional affiliations.



Copyright: © 2021 by the authors. Licensee MDPI, Basel, Switzerland. This article is an open access article distributed under the terms and conditions of the Creative Commons Attribution (CC BY) license (<https://creativecommons.org/licenses/by/4.0/>).

Abstract: Oxyresveratrol, a polyphenol extracted from the plant *Artocarpus lakoocha* Roxb, has been reported to be an antioxidant and an oxygen-free radical scavenger. We investigated whether oxyresveratrol affects the generation of superoxide anion (O_2^-) by human monocytes, which are powerful reactive oxygen species (ROS) producers. We found that oxyresveratrol inhibited the O_2^- production induced upon stimulation of monocytes with β -glucan, a well known fungal immune cell activator. We then investigated whether the inclusion of oxyresveratrol into nanoparticles could modulate its effects on O_2^- release. We synthesized poly(lactic-co-glycolic acid) (PLGA) nanoparticles, and we assessed their effects on monocytes. We found that empty PLGA nanoparticles induced O_2^- production by resting monocytes and enhanced the formation of this radical in β -glucan-stimulated monocytes. Interestingly, the insertion of oxyresveratrol into PLGA nanoparticles significantly inhibited the O_2^- production elicited by unloaded nanoparticles in resting monocytes as well as the synergistic effect of nanoparticles and β -glucan. Our results indicate that oxyresveratrol is able to inhibit ROS production by activated monocytes, and its inclusion into PLGA nanoparticles mitigates the oxidative effects due to the interaction between these nanoparticles and resting monocytes. Moreover, oxyresveratrol can contrast the synergistic effects of nanoparticles with fungal agents that could be present in the patient tissues. Therefore, oxyresveratrol is a natural compound able to make PLGA nanoparticles more biocompatible.

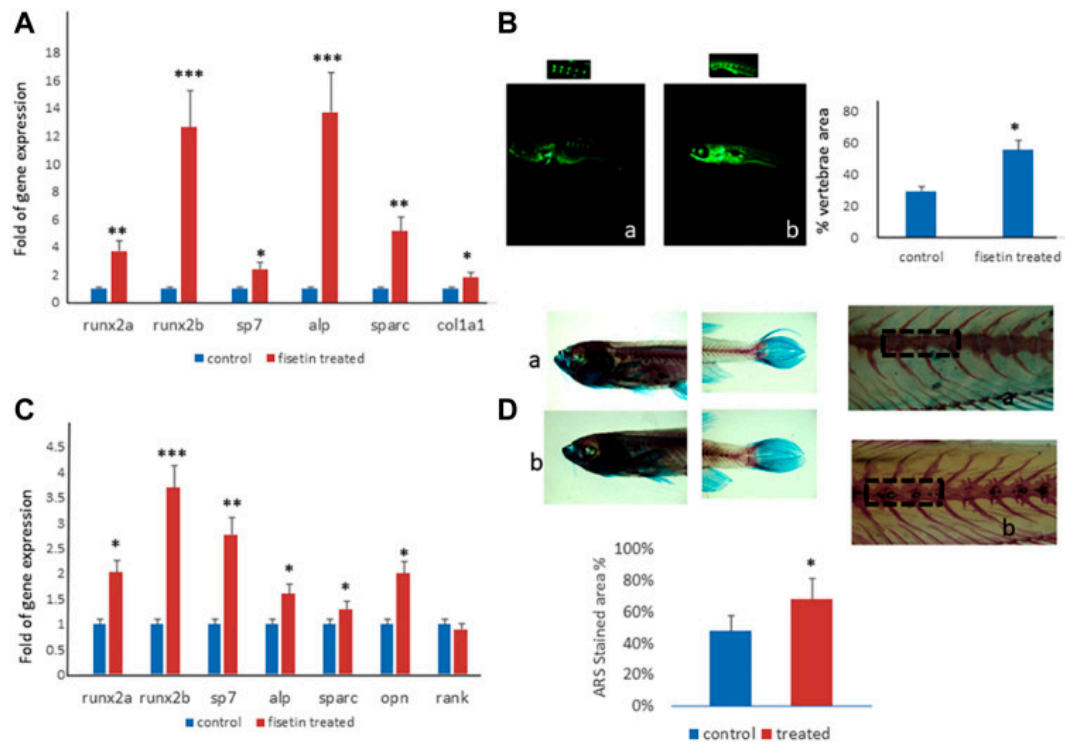
Keywords: oxyresveratrol; β -glucan; PLGA nanoparticles; ROS; monocytes

1. Introduction

Monocytes are a heterogeneous cell population initiating and propagating the immune response to pathogenic microorganisms. These cells circulate in the bloodstream and pass into the tissues where they may differentiate into resident macrophages. During inflammation, the quantity of extravasated monocytes increases to amplify the local immune response through cytokine release and phagocytosis of foreign microorganisms [1]. Upon pathogen uptake, monocytes produce reactive oxygen species (ROS) [2]. The main source of ROS in monocytes is the NOX2 NADPH oxidase, a multicomponent enzyme which transfers electrons to molecular oxygen to generate superoxide anion (O_2^-) [3,4]. ROS play an important role in defenses against infections [3–5], but they may also damage the cells by causing oxidative stress, which is responsible for several diseases, such as cancer, hypertension and neurological disorders [6].

Oxyresveratrol, a natural polyphenol extracted from the plant *Artocarpus lakoocha* Roxb, has been reported to be a good antioxidant, equipped with ROS scavenger activity [7]. In particular oxyresveratrol protects neurons [8–11], human lens epithelial cells [12] and

Fisetin: An Integrated Approach to Identify a Strategy Promoting Osteogenesis



Dalle Carbonare *et al.*, *Frontiers in pharmacology*, 13, 890693.

<https://doi.org/10.3389/fphar.2022.890693>

3.1 Aim

Studies performed by Dalle Carbonare *et al*¹³⁰ demonstrated that fisetin at 2.5 μM concentration was able to promote bone formation *in vitro* and mineralization in the zebrafish model. We have already demonstrated the potential use of PLGA as plant-derived molecules nanocarrier. Thus, we investigated whether the improved bioavailability achieved by producing fisetin-loaded PLGA positively enhances its stimulatory effects on RUNX2 and its downstream SP7 gene expression. Moreover, we performed an *ex vivo* experiment to assess the penetration ability in epithelial intestinal cells of nanoformulated fisetin.

3.2 Introduction

Among flavonoids, fisetin is known to counteract tumour growth¹³¹, osteoarthritis¹³², and rheumatoid arthritis¹³³. In addition, fisetin prevents inflammation-induced bone loss osteoarthritis, and rheumatoid arthritis. Flavonoids are phenolic compounds commonly found in vegetables and fruits. Various flavonoids (quercetin, rutin, etc) have been reported to exert beneficial properties to human health¹³⁴. Additionally, in in-vitro experiments flavonoids promoted osteogenesis by affecting the physiology of osteoblasts, bone-forming cells¹³⁵.

Osteoblasts originate from mesenchymal progenitors through osteogenic differentiation¹³⁶. This process is regulated by different extracellular signals such as bone morphogenetic proteins, parathyroid hormone, Wnt, or hedgehog pathway¹³⁷. Cellular signalling in osteogenesis involves two main actors, Runt-related transcription factor 2 (Runx2) and osterix (SP7)¹³⁸ and they both control cell proliferation and differentiation¹³⁹. In humans, Runx2 gene mutations cause cleidocranial dysplasia (CCD, OMIM#119600), a skeletal disorder with aplasia/hypoplasia of clavicles and dental abnormalities¹⁴⁰, while Sp7 has also a regulatory role by maintaining the balance between differentiation of mesenchymal precursor cells into ossified bone or cartilage¹⁴¹.

Dalle Carbonare *et al*¹³⁰ have demonstrated the potential use of fisetin as bone formation enhancer, suggesting its use in the treatment of bone diseases caused by osteogenic differentiation deregulation. Figure 16 shows a comparison between fisetin and other well-known supplemental molecules able to improve bone tissue quality. Nevertheless, Fisetin has several drawbacks related to poor water solubility and chemical instability¹⁴² limiting the use for medical and nutraceutical purpose. As hydrophobic compound, fisetin is suitable for the nano encapsulation via single emulsion method. Thus, we prepared PLGA nanoparticles loading fisetin [PLGA (Fis)] to improve solubility and chemical stability of the bioactive molecule, and

we studied the effect on cellular signalling compared to free fisetin. Finally, we investigated the percentage of intestinal filtration of nanoformulated fisetin.

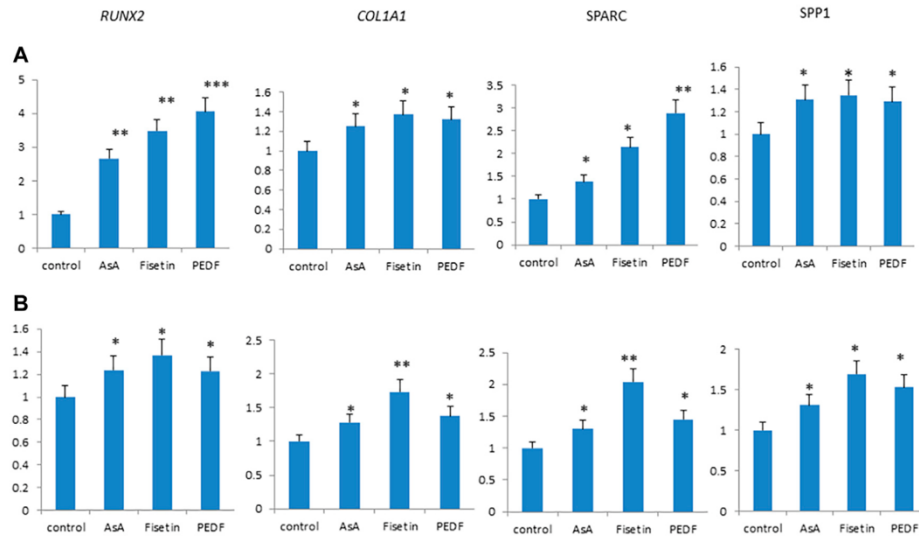


Figure 16. Fisetin, PEDF (pigment epithelium-derived factor) and AsA (ascorbic acid) were able to upregulate osteogenic genes expression in MSCs after 7 (A) and 14 (B) days of supplementation. * $p < 0.05$; ** $p < 0.01$; *** $p < 0.005$.

3.3 Experimental section

Materials. PLGA [poly(DL-lactide-co-glycolide), 50:50 lactide-to-glycolide ratio, CAS 26780-50-7], PVA [poly(vinyl alcohol), CAS 9002-89-5], and acetone ($\geq 99\%$ purity, 1.00013) were purchased from Merck. Fluorescein isothiocyanate (FITC, CAS 27072), cellulose membrane dialysis tubing (CASD9777-100), dimethyl sulfoxide (DMSO, $\geq 99\%$ purity D-5879) were purchased from Sigma-Aldrich. Fisetin was purchased from Santa Cruz Biotechnology (SC-276440).

Nanoparticles preparation. The protocol used for the production of PLGA[Fis] nanoparticles is based on a single emulsion evaporation method, under sterile conditions at 20°C. 20 mg of the polymer and 4 mM (1.14 mg) of fisetin were co-dissolved in 1 ml of DMSO 100%; the obtained organic phase was added dropwise under stirring (2,000 RPM) to 10 ml of 0.5% polyvinyl alcohol (PVA) aqueous solution and left overnight to evaporate the organic phase. Afterward, the preparation was pelleted at 4°C 11,000 rpm for 20 min (Eppendorf Centrifuge 5804R), and the nanoparticles were collected and washed twice with 10 ml of Milli-Q water. Finally, the purified nanoparticles were resuspended in 1 ml of phosphate-buffered saline (PBS) solution pH 7.4 (or NaCl 0.9%) for the subsequent analysis and storage at 4°C, otherwise freeze-dried. Empty nanoparticles were prepared with the same protocol avoiding the addition of fisetin to the reaction. Furthermore, to perform an internalization study and visualize nanoparticles inside cells, PLGA NPs co-delivering fisetin and fluorescein isothiocyanate (FITC) (PLGA[Fis&Fitc]) were prepared dissolving 20 mg of PLGA in a mixture of 640 μ l of acetone and 360 μ l of fisetin/FITC DMSO solution; the molar ratio between fisetin and FITC is 1:1. The other steps were the same as described previously.

Size and ζ -Potential Characterization (DLS, NTA, AFM). The size and ζ -potential of PLGA nanoparticles were estimated at 25 °C by dynamic light scattering (DLS) (Nano Zeta Sizer ZS, ZEN3600, Malvern Instruments, Malvern, Worcestershire, United Kingdom). Nanoparticles were resuspended in PBS, used as a stock

suspension, and were diluted 20 times in PBS for size determination and in 10 mM NaClO₄pH 7.5 for ζ -potential measurements; data were collected in triplicate and analyzed by ZetaSizer software.

To support DLS data, a Nanosight tracking analysis was performed on PLGA[Fis] and empty NPs (Malvern NanoSight NS300). Due to the high concentration, each sample was diluted 10,000 or 5,000 times; 1,498 frames divided into 3 runs of 60 s were recorded at a camera level of 13, and the analysis was performed with a detection threshold in the range 5–7. Finally, the number of particles/ml was estimated as well.

A volume of 20 μ l of each sample (prepared as mentioned in the previous section) was loaded on a bracket covered by an inert mica surface. After 15 min of solvent evaporation, the analysis was performed using an NT-MDT Solver Pro atomic force microscope with NT-MDT NSG01 golden coated silicon tip in semi-contact mode with different scanning frequencies (3–1 Hz) in order to produce optimized AFM images. The microscope was calibrated by a calibration grating (TGQ1 from NT-MDT) in order to reduce nonlinearity and hysteresis in the measurements. Finally, images were processed with the Scanning Probe Image Processor (SPIP™) program (Friis Jan, 2009), and a statistical study was performed to compare results to DLS and Nanosight data.

Absorbance and Emission Spectroscopy. The absorbance pattern of each sample resuspended in PBS or water was analyzed using a Thermo Fisher Evolution 201 UV-Visible Spectrophotometer in the range 250–600 nm to assess the presence of fisetin inside nanoparticles and the co-presence of fisetin and FITC. Moreover, the emission pattern was recorded upon excitation at 360 and 495 nm (excitation wavelengths for fisetin and FITC, respectively) by using a Jasco Spectrofluorometer FP-8200.

Encapsulation Efficiency and Drug Loading. To quantify the amount of fisetin entrapped, PLGA[Fis] NPs were dissolved in DMSO and analysed using the calibration line (Fig x). Encapsulation efficiency and drug loading (DL) were estimated using the following equations:

$$EE (\%) = \frac{Fis_{loaded}}{Fis_{fed}} \times 100$$

$$DL (\%) = \frac{mg \text{ of } Fis_{loaded}}{mg \text{ of } PLGA} \times 100$$

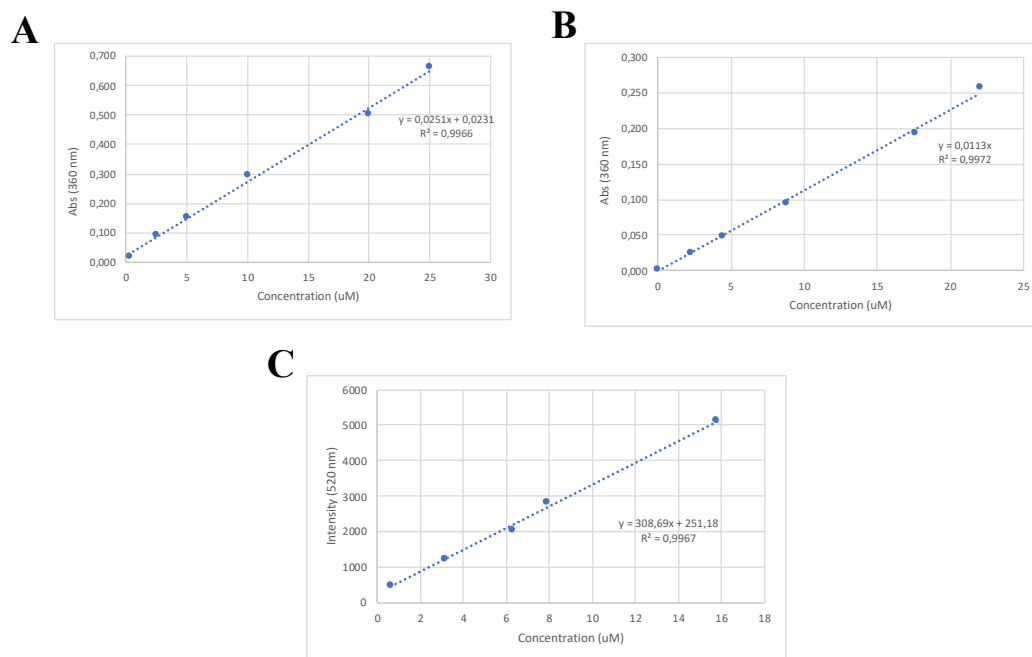


Figure 17. Calibration curves in DMSO (A) and Physiological solution (B, C).

Stability and In Vitro Drug Release. To assess the capacity of the nanoparticles to retain entrapped fisetin over time, a first release study was performed in a total volume of 1 ml, at different temperatures (4 and 37°C) and different media (water, PBS, NaCl 0.9%, and citric acid pH 5). Dialysis was used to carry out the in vitro drug release studies increasing the final volume. PLGA[Fis] NPs were introduced into the dialysis bag (14,000 da molecular weight cutoff, Sigma Aldrich, D9777-100FT) and placed in 100 ml of PBS pH 7.4 containing 0.1%v/v Tween 80 as the release media and stirred at 100 rpm. Samples were collected at different time intervals and replaced with an equal volume of media to maintain the sink condition.

The released fisetin was quantified using a calibration curve obtained by UV–visible spectroscopy at 360 nm ¹⁴³.

Fluid-Dynamic Intestinal Model Resembling Systemic Administration for PLGA[Fis]. A compartmental fluidic device (commercialized as MIVO React4life S.r.l., IT) was used to perform in vitro drug efficacy tests. The 3D fluidic model was performed as follows: 1) 24-well size inserts containing human intestinal tissue (EpiIntestinal by Mattek) were placed and cultured within the device, forming two fluidically independent chambers: the donor and the receiver; 2) both chambers were filled with the culture medium; and 3) the receiver chamber was connected to the peristaltic pump to form a closed-loop fluidic circuit containing 3.8 ml medium circulating at a rate of 0.3 cm/s, to simulate the capillary flow rate. Therefore, a medium containing PLGA[Fis] was added to the donor chamber.

Cell viability. The Cell Proliferation Kit II (XTT Chemicon) was used to evaluate cell viability, as previously described. Six replicates in three independent experiments were tested.

Cell cultivation. Human mesenchymal stem cells (hMSC, PromoCell, Heidelberg, Germany) were used by culturing at a density of 5×10^4 cells with the mesenchymal stem cell growth medium (PromoCell) or osteogenic differentiation medium (PromoCell, Heidelberg, Germany) and incubated at 37°C in a humidified atmosphere with 5% CO₂. Differentiating cells were then used for further analyses. Human dermal fibroblast cultures were established from explanted skin biopsies taken from patient P1 [mutation: c.897T>G->p (Tyr299*), male, 8 years old], P2 [c.1019del->p (Ser340*), female, 10 years old], and a healthy age-matched control with appropriate consent, as previously reported (Venturi et al., 2012). The cells were cultured with high-glucose DMEM (ECB7501L, EuroClone, Milano, Italy) supplemented with 10% FBS (10270-106, Gibco, Life Technologies Limited, Paisley, United Kingdom), 2 mM l-glutamine (5-10K00-H, BioConcept AG, Paradiesrain, Allschwil, Switzerland), 100 U/ml penicillin, and 100 µg/ml streptomycin (penicillin–

streptomycin; ECB3001D, EuroClone, Milano, Italy), as previously described (Venturi et al., 2012).

Realtime experiment. To investigate gene expression modulation, we performed real-time PCR analyses as reported previously¹⁴⁴. Briefly, predesigned, gene-specific primers and probe sets for each gene [RUNX2, hs00231692_m1; OSTERIX (SP7), hs00541729_m1; collagen, type i, alpha 2 (COL1A2), hs01028956_m1; osteonectin (SPARC), hs00234160_m1; OSTEOPONTIN (SPP1), hs00167093_m1, B2M, hs999999_m1 (housekeeping); and GAPDH, 0802021 (housekeeping)] were obtained from assay-on-demand gene expression products (Thermo Fisher Corporation, Waltham, MA, United States). In addition, the following custom primer sets (Invitrogen, Carlsbad, CA, United States) were also used: runx2a (fw GACGGTGGTGACGGTAATGG, rv TGCGGTGGGTTCGTGAATA), runx2b (fw CGGCTCCTACCAGTTCTCCA, rv CCATCTCCCTCCACTCCTCC), rank (fw GCA CGGTTATTGTTGTTA, rv TATTCAGAGGTGGTGTAT), and housekeeping gene actb1 (fw CCCAAAGCCAACAGAGAGAA, rv ACCAGAAGCGTACAGAGAGA). Ct values for each reaction were determined using TaqMan SDS analysis software (Applied Biosystems; Foster City, California, United States) as reported previously. To calculate relative gene expression levels between different samples, we performed the analyses using the $2^{-\Delta\Delta CT}$ method as previously reported¹⁴⁴.

Western blot. RUNX2 protein levels were separated by SDS-PAGE and investigated using Western blot analyses as previously reported (Brugnara and De Franceschi, 1993). Briefly, proteins were extracted by a RIPA buffer (Thermo Fisher Scientific, Waltham, MA, United States), and the proteins were quantified by BCA assay (Thermo Fisher Scientific, Waltham, MA, United States). Proteins were separated by sodium dodecyl sulfate–polyacrylamide gel electrophoresis (SDS-PAGE) and then were transferred onto polyvinylidene difluoride (PVDF) membranes (Thermo Fisher Scientific, Waltham, MA, United States). The PVDF membranes were then probed with the primary antibody for RUNX2 (Cell Signaling, 8486) and β -actin (BA3R) (Thermo Scientific), and secondary antibodies anti-mouse (Cell

Signaling, 7076) and anti-rabbit (Cell Signaling 7074). Signals were detected using a chemiluminescence reagent (ECL, Millipore, Burlington, MA, United States), as previously reported (de Franceschi et al., 2004). Images were acquired by an LAS4000 Digital Image Scanning System (GE Healthcare, Little Chalfont, United Kingdom). The densitometric analysis was performed by ImageQuant software (GE Healthcare, Little Chalfont, United Kingdom). Protein optical density was normalized to β -actin.

Statistical analysis. Results were expressed as mean \pm SD. The statistical analysis was assessed by Student's paired t-test comparing each treatment to the control. Differences were considered positive when $p < 0.05$. For in vitro data, analyses were applied to experiments carried out at least three times. We used SPSS for Windows, version 22.0 (SPSS Inc., Chicago, IL, United States), to analyze the data.

All the in vitro experiments have been performed by Dr. Valenti and Prof Dalle Carbonare' lab, Department of Medicine and Department of Neurosciences, Biomedicine and Movement Sciences - University of Verona

3.4 Results

3.4.1 Physico-Chemical Characterization

We prepared fisetin embedded PLGA nanoparticles to prevent its degradation in order to make the supplementation potentially available for human use. Table 5 shows a comparison between our nano formulation and PLGA-based preparations found in literature ^{142,143,145}. FHIC-PNP was prepared by firstly forming the inclusion complex between Fisetin and hydroxyl propyl beta cyclodextrin (FHIC) to improve solubility of the flavonoid, since the preparation method is based on double emulsion W/O/W. F1, F2 and F3 were prepared by modified nanoprecipitation method tuning the proportion of Poly-(ϵ -caprolactone) (PCL) and PLGA-PEG-COOH. Finally, even FST-PLGA was synthesized by nanoprecipitation where only PLGA was used as raw material. In this study, we simplified and optimized the preparation producing PLGA nanoparticles embedded with fisetin (PLGA[Fis]) by single emulsion method.

PLGA[Fis] showed a more negative ζ -potential than that reported by Kadari *et al.*, conferring it good colloidal stability. Moreover, we achieved a higher drug loading value, corresponding to 23.51%, 6 to 8 times greater than the result reported in Sechi *et al.* PLGA[Fis] nanoparticles show a lower particle size than all the other herein reported, except for those prepared by Kadari *et al.*, but in every case showing a better monodispersivity, as it is evident from the lower PDI value. To further investigate the size distribution of nanoparticles, nanotracking and AFM analysis were also performed. The nanoparticles shape is quite spherical (Figure 18), and, as it is evident from Table 6, data from the three different methods are in agreement and span in the same order of magnitude, even if the techniques are based on different physicochemical properties.

Table 5. Particle size, polydispersity index (PDI), encapsulation efficiency (EE), and drug loading (DL) data for present nanoparticles (PLGA[Fis]*) compared with those of Kadari *et al*** Sechi *et al**** and Liu *et al*****. *Measurements were performed in triplicate.

Nanoformulation	Particles size (nm)	PDI	ζ-Potential (mV)	EE (%)	DL (%)
PLGA[Fis]*	139.2 ± 4.0	0.11 ± 0.02	-10.20 ± 0.30	75.57 ± 4.21	23.51 ± 5.07
FHIC-PNP**	87.3 ± 10.0	0.25 ± 0.01	-8.71 ± 0.03	78.80 ± 0.55	-
F1***	146.2 ± 2.3	0.12 ± 0.05	-	81.96 ± 3.80	4.10 ± 0.20
F2***	198.7 ± 6.0	0.16 ± 0.02	-	74.78 ± 1.9	3.74 ± 0.10
F3***	165.4 ± 3.3	0.15 ± 0.02	-	69.76 ± 2.8	3.49 ± 0.10
FST-PLGA****	187.9 ± 6.1	0.12 ± 0.01	-29.20 ± 1.60	79.30 ± 2.7	-

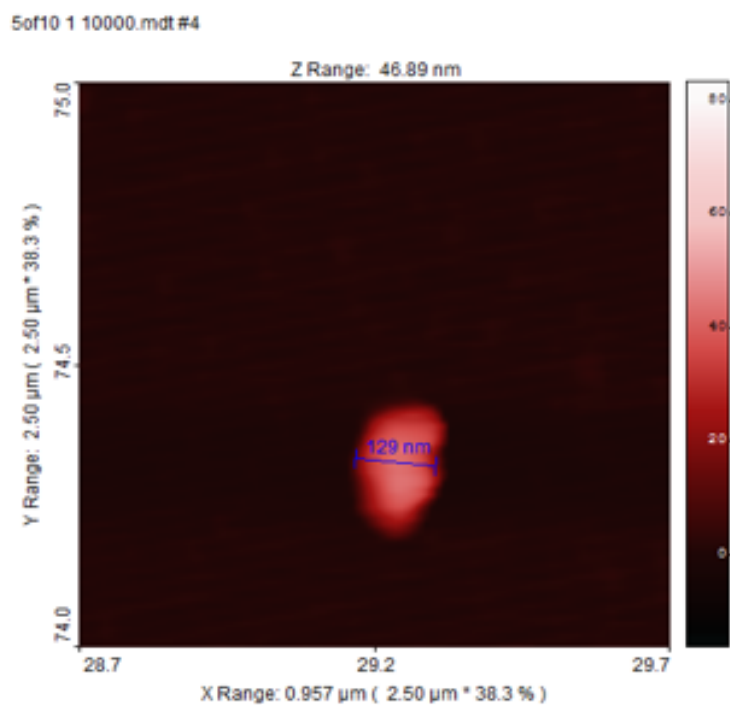


Figure 18. AFM image of single PLGA[Fis] of 129 nm.

Furthermore, freeze-drying did not negatively affect the samples: nanoparticles preserved the size after resuspension in the desire buffer. Furthermore, the co-encapsulation of fisetin and FITC led to nanoparticles slightly bigger than the single-loaded ones.

Table 6. DLS, AFM, and nanotracking analysis data of empty, PLGA[Fis], freeze-dried PLGA[Fis]*, and PLGA[Fis&Fitc) nanoparticles. The statistical analysis was performed over a population greater than 30 units using SPIP statistical tool.

Nanoformulation	Z-average (nm)	Peak Number (nm)	AFM diameter (nm)	NTA distribution (nm)
Empty	173.8 ± 2.0	141.6 ± 44.3	181.8 ± 28.0	136.0 ± 29.1
PLGA[Fis]	130.2 ± 4.0	105.1 ± 31.7	142.7 ± 17.3	117.3 ± 21.8
Dried- PLGA[Fis]*	152.6 ± 2.7	115.1 ± 37.4	172.6 ± 27.9	125.1 ± 27.4
PLGA[Fis&Fitc]	180.6 ± 2.8	139.6 ± 55.3	193.6 ± 40.7	123.6 ± 28.2

3.4.2 Spectroscopy

As it was described in the case of PLGA embedded with oxyresveratrol, we performed emission spectroscopy studies to verify if fisetin was encapsulated unperturbed into PLGA NPs. Figure 19. shows a comparison between empty and loaded nanoparticles upon excitation of 360 nm, the suitable excitation wavelength of Fisetin. We collected a spectrum from 370 to 700 nm in which we observed a peak at 530 nm identifying fisetin molecules. Moreover, empty nanoparticle showed a zero signal at 530 nm while a weak peak was collected at 408 nm. This emission is related to nanostructure as reported in literature^{37,38,86}.

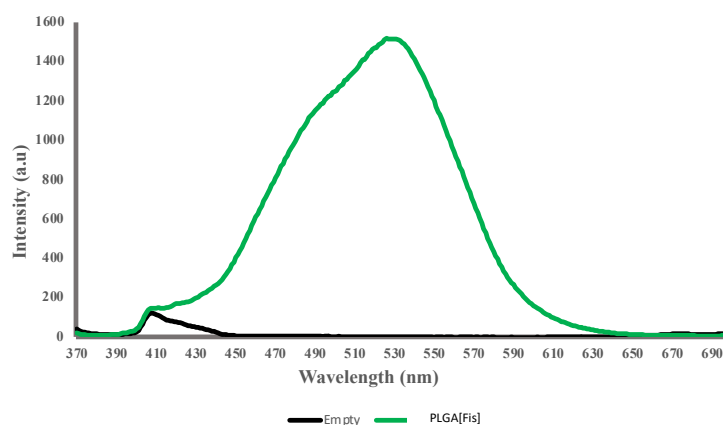


Figure 19. Comparison between emission spectra of PLGA[Fis] (green line) and Empty (black line) upon excitation of 360 nm.

To investigate the cellular uptake by fluorescence microscopy, we co-encapsulated both FITC dye molecules with Fisetin into PLGA NPs (PLGA[Fis&Fitc] NPs). To assess the presence of both dye and flavonoid PLGA[Fis&Fitc] NPs were excited at 450 and 360 nm to collect the emission spectra from FITC and fisetin respectively (figure 20). Interestingly, upon excitation at 450 nm of PLGA[Fis&Fitc] emission pattern was slightly shifted towards the same peak collected for PLGA[Fitc] NPS (520 nm) while upon excitation at 360 nm the emission pattern was close to only fisetin containing nanoparticle spectra (530 nm). Nevertheless, the co-delivery of FITC with Fis into the same carrier was confirmed in the subsequent analysis by fluorescence-microscopy.

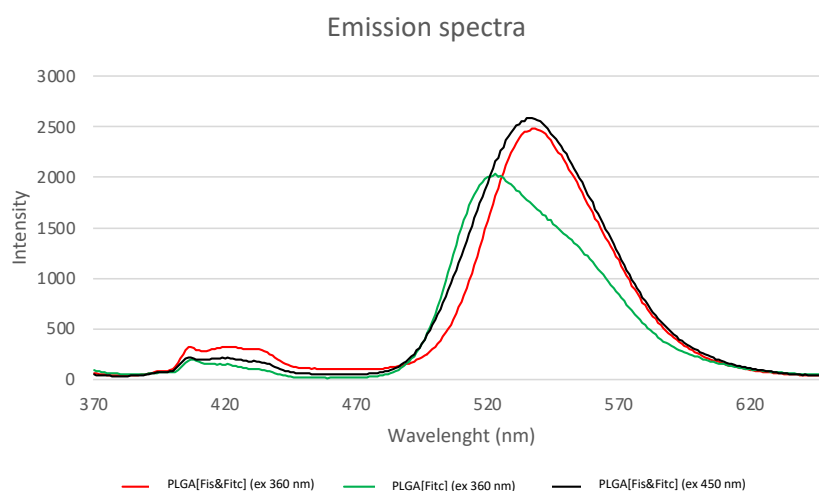


Figure 20. Emission spectra of PLGA[Fis&Fitc] upon excitation at 360 nm (red line) and 450 nm (black line). Emission spectrum of PLGA[Fitc] upon excitation at 450 nm (green line).

3.4.3 Release pattern

In a final 1 ml volume fisetin release rate from PLGA nanoparticles was tested at different temperatures (4 and 37 °C) in PBS. We also investigated the release in citric acid pH 5 to mimic inflammation condition of bone tissues, typical for osteoarthritis and rheumatoid disease^{146–148}. As it is evident from Figure 21A, after an initial burst loss, the release kinetics dropped dramatically. The temperature increase, as expected, leads to fast kinetics, while an acidic pH seems to slow down the loss. Then, an in vitro release study on the volume subsequently used for tests on intestinal epithelial tissue was carried out (Figure 21B). PLGA[Fis] NPs exerted a sustained release trend assessed by the fitting with a second-degree polynomial function. In the first half hour, only 10% of fisetin was explosively released (slope value 17) while in 6 hours the slope decreases reaching a value of 4 (30% of release). Finally, within 48 hours we observed a complete prolonged release for fisetin, with a slope value for the release curve of 1.

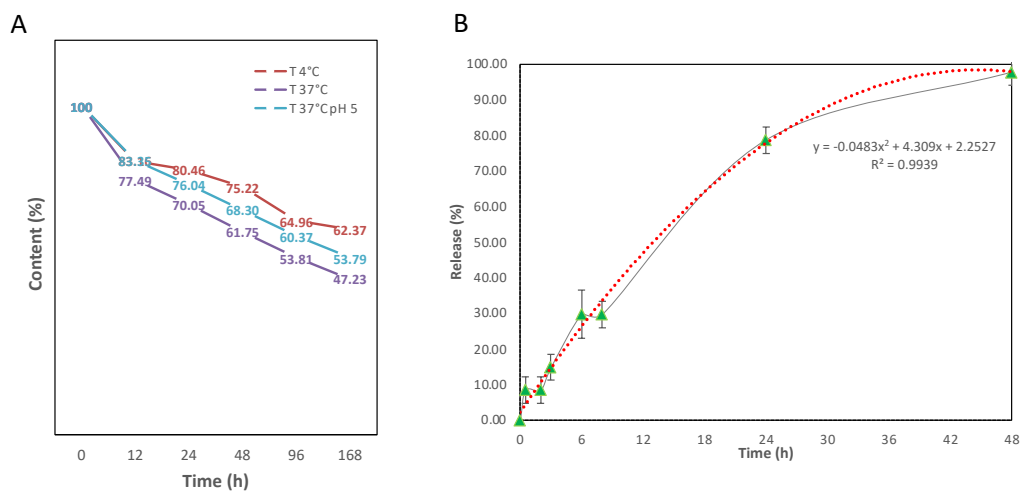


Figure 21. (A) Release test performed at different temperatures (4°C (red line) and 37°C (purple line) in PBS and in citric acid pH 5 37°C (blue line)) in a final volume of 1 ml. (B) In-vitro release study in 100 ml of physiological solution that fits with a second-grade polynomial function curve (red dots).

3.4.4 *In vitro* studies

A microfluidic system containing human intestinal epithelial tissue was created to assess the ability of PLGA[Fis] to cross the intestine (Figure 22). As expected PLGA[Fis] could cross the intestinal epithelium since the nanoparticles with negative zeta potential are taken up by Peyer's patches and are translocated into the blood circulation¹⁴⁹. Our data are shown in Table 7: after 5 h incubation, less than 5% of the initial concentration crossed the epithelium, while a value of 30% was reached within 16 h. The fisetin amount has been calculated using a fluorescence calibration curve. Moreover, PLGA[Fis] recovered after the experiment in the volume filtered by the epithelium showed a slight increase in the size, with values of approximately 190 nm (figure 23).

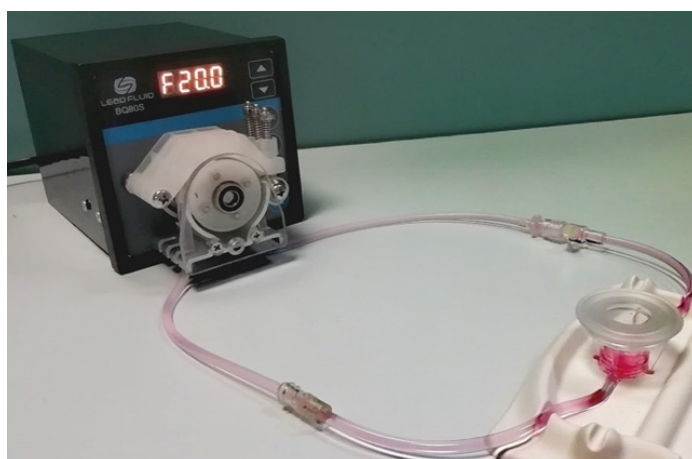


Figure 22. Microfluidic system containing human intestinal epithelial tissue to assess the ability of PLGA[Fis] to cross the intestine.

Table 7. Quantification of fisetin concentration crossing the intestinal epithelium after 5 and 16 h. All the experiments have been performed in triplicate.

Concentration of PLGA[Fis] added to the intestinal epithelium tissue (μM)	Concentration of PLGA[Fis] crossing the epithelium after 5 hours (μM)	Concentration of PLGA[Fis] crossing the epithelium after 16 hours (μM)
$1,550.0 \pm 28.3$	73.4 ± 17.2	436.2 ± 79.5

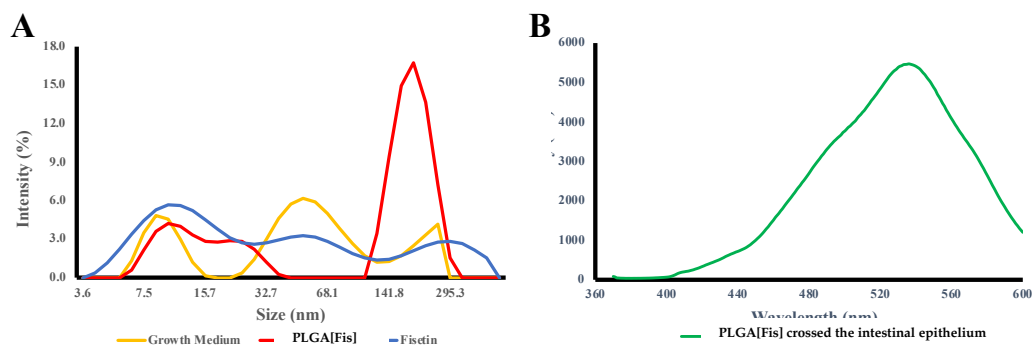


Figure 23. (A) DLS intensity output of PLGA[Fis] NPs (red line), Growth Medium (yellow line), Free fisetin (Blu line). (B) Emission spectra of PLGA[Fis] NPs crossed the intestinal epithelium.

Subsequently, to test the ability of PLGA[Fis] to enter cells while induce osteogenic differentiation, we treated mesenchymal stem cells (MSCs) with PLGA[Fis&Fite] nanoparticles. MSCs were cultured in an osteogenic medium with or without PLGA[Fis&Fite] for 7 days. PLGA[Fis&Fite] were added to every medium change (every 2 or 3 days). Four hours after the addition of the complete medium, nanoparticles were visible in intercellular spaces (Figure 24A). After 6 h of treatment, fisetin (in green) was completely incorporated into the cells (Figure 24B). After 7 days of osteogenic differentiation, cells were collected to perform gene expression analyses. As shown in Figure 24C, we observed that PLGA[Fis] increased the expression of the osteogenic transcription factors RUNX2 and SP7 compared to free fisetin-supplemented cells. Accordingly, COL1A1, a marker of osteogenic maturation, was higher in cells treated with PLGA[Fis] than in control cells (Figure 24D).

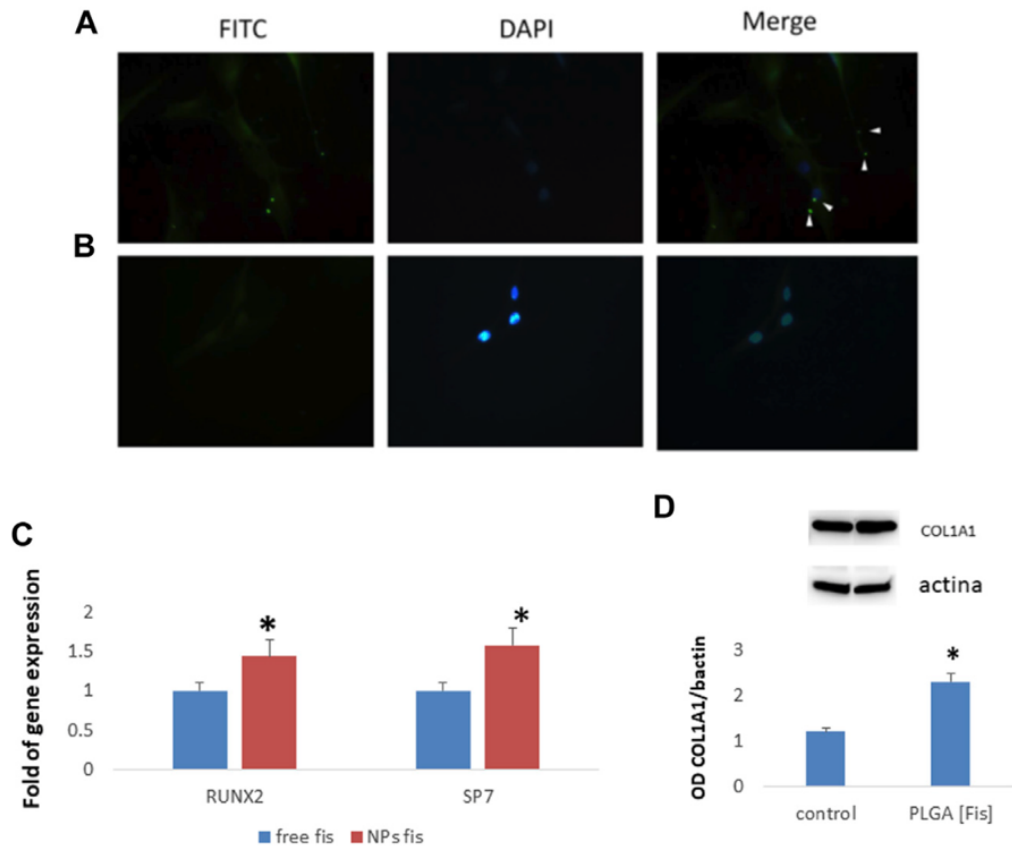


Figure 24. PLGA[Fis] are visible after 4 h of treatment in cultures and fisetin (in green, FITC) diffuses in intercellular spaces (A). However, after 6 h, fisetin is completely absorbed, and only cellular nuclei [blue, 4',6-diamidino-2-fenilindolo diidrocloruro (DAPI) stained nuclei] are visible (B). After 7 days of osteogenic differentiation, PLGA[Fis] increased the expression of the osteogenic transcription factors RUNX2 and SP7 (C). COL1A1 chain levels increased in cells treated with PLGA[Fis] compared to control (D). * $p < 0.05$. Magnification $\times 40$.

3.5 Discussion

In the first reported study, a double emulsion was made to prepare the nanomaterial and specifically fisetin was complexed with hydroxyl propyl beta-cyclodextrin to increase its solubility in water; then it was emulsified to obtain the PLGA nanoparticles. In the second reported study, the authors used a nanoprecipitation and two different polymers (PLGA-peg and polycapryl lactone)^{142,143,145}. However, we used a single emulsion, a simpler method if compared to those previously reported. We obtained colloidal stable nanoparticle with size close to 140 nm and showing the highest drug loading value (23.51 ± 5.07). Moreover, we achieved $75.57 \pm 4.21\%$ as encapsulation efficiency, in line with those reported in previous studies (table 5).^{142,143,145}. Notably, fisetin is not complexed with other molecules, and it interacts directly with PLGA (so “pure” fisetin is released, instead of a fisetin-excipient complex). By comparing the release kinetics at different temperatures and pH, PLGA was able to effectively retain fisetin: for instance, at 37 °C pH 5, more than 60% of fisetin was still recorded to be inside the nanoparticles. Moreover, the release pattern studied in physiological solution suggested that fisetin is completely released within 48 hours. Therefore, the sustained release obtained thanks to the PLGA cover, could be an interesting characteristic for medical/nutraceutical purposes favouring patient compliance. Additionally, we proved that 4 °C and freeze-drying can be used for storage purpose without affecting the quality of the nanomaterial and of the active compound as well.

PLGA encapsulation process did not negatively affected the chemical structure of the payload as it was confirmed by the emission pattern collected for PLGA[Fis] and PLGA[Fis&Fitc] Nps. This allowed to follow the interaction between cells and the complex structure such as intestinal epithelial barrier. By fluorescence microscopy, PLGA[Fis&Fitc] Nps were completely uptaken within 4 hours while after 6 hours the FITC green emission disappeared, suggesting complete metabolization by MSCs. PLGA internalization mechanism involves generally peacking both clathrin-dependent and clathrin-independent endocytosis. Cell membrane is highly

selective and is able to block access to nanoparticles smaller than 50 nm while for dimensions larger than 200 nm an active mechanism is often required to favour the uptake, usually mediated by clathrin. Due to the size within 50-200 nm, we suppose a clathrin-independent endocytosis mechanism be involved in the uptake of PLGA[Fis&Fitc] Nps , although other studies are required¹⁵⁰. Furthermore, PLGA[Fis] NPs were also able to entirely cross the intestinal epithelium cells preserving the payload, as it was demonstrated by DLS intensity diagram and by fisetin emission pattern. Within 16 hours, a concentration close to $436.17 \pm 79.5 \mu\text{M}$ of crossed nanodelivered fisetin was found, corresponding to 30%. Furthermore, the observed increase in size of PLGA[Fis] from 140 to 190 nm, might be due to the well-known protein corona phenomenon or to some interactions occurring during the epithelial tissue crossing.

Finally, as a consequence of the improvement in bioavailability we observed an increased osteogenic differentiation in MSCs supplemented with PLGA-encapsulated fisetin compared to fisetin alone. In fact, nano-delivered fisetin lead to an increase in the expression, almost double compared to free fisetin, of the main genes (RUNX2, SP7, COL1A1) crucial for osteogenesis regulation.

3.6 Conclusion

In conclusion, we prepared narrow-sized PLGA[Fis] nanoparticles with elevated drug loading and enabling to cross the human intestinal epithelial tissue. Moreover, PLGA can effectively stabilize and protect a labile payload such as fisetin over time. Therefore, our findings demonstrated the positive effects of fisetin on osteogenesis and suggest that patients affected by skeletal diseases, both of genetic and metabolic origins, may benefit from fisetin supplementation. In this regard, the sustained release properties of PLGA[Fis] could improve patient compliance.



Fisetin: An Integrated Approach to Identify a Strategy Promoting Osteogenesis

Luca Dalle Carbonare¹, Jessica Bertacco^{1,2}, Salvatore Calogero Gaglio³, Arianna Minoia¹, Mattia Cominacini¹, Samuele Cheri¹, Michela Deiana¹, Giulia Marchetto¹, Anna Bisognin³, Alberto Gandini⁴, Franco Antoniazzi⁴, Massimiliano Perduca³, Monica Mottes² and Maria Teresa Valenti^{1,2*}

¹Department of Medicine, University of Verona, Verona, Italy, ²Department of Neurosciences, Biomedicine and Movement Sciences, University of Verona, Verona, Italy, ³Biocrystallography Lab, Department of Biotechnology, University of Verona, Verona, Italy, ⁴Department of Surgery, Dentistry, Pediatrics and Gynecology, University of Verona, Verona, Italy

OPEN ACCESS

Edited by:

Anjali P Kusumbe,
University of Oxford, United Kingdom

Reviewed by:

Pamela Maher,
Salk Institute for Biological Studies,
United States
Kenza Benzeroual,
Long Island University, United States

*Correspondence:

Maria Teresa Valenti
mariateresa.valenti@univr.it

Specialty section:

This article was submitted to
Experimental Pharmacology and Drug
Discovery,
a section of the journal
Frontiers in Pharmacology

Received: 06 March 2022

Accepted: 11 April 2022

Published: 16 May 2022

Citation:

Dalle Carbonare L, Bertacco J, Gaglio SC, Minoia A, Cominacini M, Cheri S, Deiana M, Marchetto G, Bisognin A, Gandini A, Antoniazzi F, Perduca M, Mottes M and Valenti MT (2022) Fisetin: An Integrated Approach to Identify a Strategy Promoting Osteogenesis. *Front. Pharmacol.* 13:890693. doi: 10.3389/fphar.2022.890693

Flavonoids may modulate the bone formation process. Among flavonoids, fisetin is known to counteract tumor growth, osteoarthritis, and rheumatoid arthritis. In addition, fisetin prevents inflammation-induced bone loss. In order to evaluate its favorable use in osteogenesis, we assayed fisetin supplementation in both *in vitro* and *in vivo* models and gathered information on nanoparticle-mediated delivery of fisetin *in vitro* and in a microfluidic system. Real-time RT-PCR, Western blotting, and nanoparticle synthesis were performed to evaluate the effects of fisetin *in vitro*, in the zebrafish model, and in *ex vivo* samples. Our results demonstrated that fisetin at 2.5 μ M concentration promotes bone formation *in vitro* and mineralization in the zebrafish model. In addition, we found that fisetin stimulates osteoblast maturation in cell cultures obtained from cleidocranial dysplasia patients. Remarkably, PLGA nanoparticles increased fisetin stability and, consequently, its stimulating effects on RUNX2 and its downstream gene SP7 expression. Therefore, our findings demonstrated the positive effects of fisetin on osteogenesis and suggest that patients affected by skeletal diseases, both of genetic and metabolic origins, may actually benefit from fisetin supplementation.

Keywords: osteogenesis, PLGA, fisetin, mesenchymal stem cells, differentiation

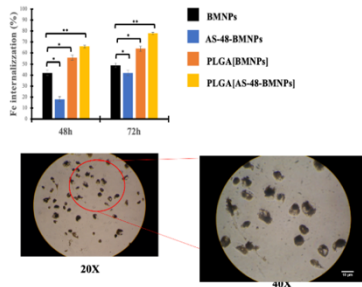
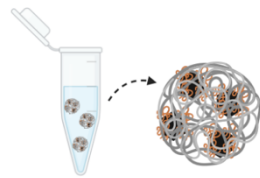
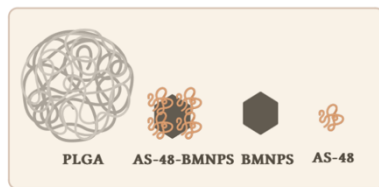
1 INTRODUCTION

Flavonoids are phenolic compounds commonly found in vegetables and fruits. Various flavonoids have been described, and it has been demonstrated that they produce biological effects through different mechanisms of action (Cederroth and Nef, 2009).

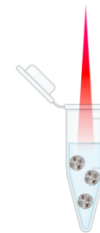
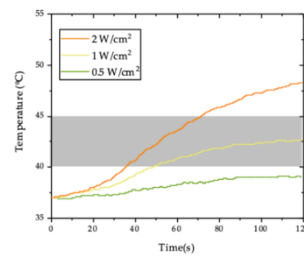
In vitro experiments have shown that flavonoids are able to modulate osteogenesis by affecting the physiology of bone-forming cells, that is, osteoblasts (Trzeciakiewicz et al., 2009).

It is well known that osteoblasts originate from mesenchymal progenitors through osteogenic differentiation (Kular et al., 2012). This process is regulated by different extracellular signals such as bone morphogenetic proteins, parathyroid hormone, Wnt, or hedgehog pathway (Soltanoff et al., 2009). Cellular signaling induces the expression of transcription factors, including Runt-related transcription factor 2 (Runx2) and osterix (SP7) (Marie, 2008). In particular, Runx2 is the osteogenic master gene, controlling proliferation and differentiation (Komori, 2010, 2). In humans, Runx2 gene mutations cause cleidocranial dysplasia (CCD, OMIM#119600), a skeletal disorder with aplasia/

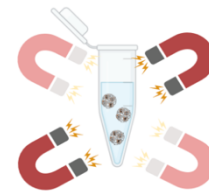
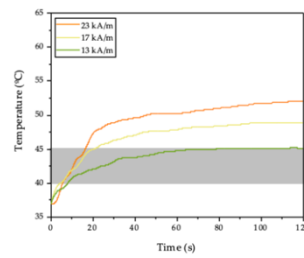
Embedding Biomimetic Magnetic Nanoparticles Coupled with Peptide AS-48 into PLGA to Treat Intracellular Pathogens



Photothermia



Magnetic Hyperthermia



Created with BioRender.com

Gaglio, S.C *et al.* Pharmaceuticals 2022, 14, 2744. <https://doi.org/10.3390/pharmaceutics14122744>

4.1 Aim

Among the strategies employed to overcome the development of multidrug-resistant bacteria, directed chemotherapy combined with local therapies (e.g., magnetic hyperthermia) has gained great interest. A nano-assembly coupling the antimicrobial peptide AS-48 to biomimetic magnetic nanoparticles (AS-48-BMNPs) was demonstrated to have potent bactericidal effects on both Gram-positive and Gram-negative bacteria when the antimicrobial activity of the peptide was combined with magnetic hyperthermia. Nevertheless, intracellular pathogens remain challenging due to the difficulty of the drug reaching the bacterium. Thus, improving the cellular uptake of the nanocarrier is crucial for the success of the treatment. In the present study, we demonstrated the cellular uptake of the original nano-assembly into THP-1, reducing the toxicity of AS-48 toward healthy THP-1 cells. Thus, we optimized the design of PLGA[AS-48-BMNPs] in terms of size, colloidal stability, and hyperthermia activity (either magnetic or photothermal). The stability of the nano-formulation at physiological pH values was evaluated by studying the AS-48 release at this pH value. The influence of pH and hyperthermia on the AS-48 release from the nano-formulation was also studied. These results show a slower AS-48 release from PLGA[AS-48-BMNPs] compared to previous nano-formulations, which could make this new nano-formulation suitable for longer extended treatments of intracellular pathogens. PLGA[AS-48-BMNPs] are internalized in THP-1 cells where AS-48 is released slowly, which may be useful to treat diseases and prevent infection caused by intracellular pathogens. The treatment will be more efficient when combined with hyperthermia or photothermia.

4.2 Introduction

Directed chemotherapy to treat local infections is not only necessary to avoid undesired secondary effects, but also to reduce the number of drugs needed to control the infection. This advantage becomes crucial in the context of antibiotics. In fact, the World Health Organization (WHO) is warning about the increase in the failure of common antibacterial therapies due to the development and selection of multi-drug-resistant (MDR) bacteria, mainly due to the generalized and/or extended drug administration¹⁵¹. As an example, MDR *Mycobacterium tuberculosis* strains have developed resistance to the two major “first-line” drugs used against tuberculosis (isoniazid and rifampicin). Treatment of MDR *M. tuberculosis* requires long-lasting therapy (administered daily for 7–9 months) based on the use of less efficient and more toxic drugs¹⁵².

Among the strategies to overcome the problem of MDR pathogens, directed chemotherapy combined with another local therapy (e.g., magnetic hyperthermia) has gained great interest. Wu *et al.*¹⁵³ showed the potential of combining a photothermic–chemical treatment for a murine subcutaneous abscess induced by methicillin-resistant *Staphylococcus aureus*. Wang *et al.*¹⁵⁴ developed a dual-targeted platform for synergistic chemo–photothermal therapy against multidrug-resistant Gram-negative bacteria and their biofilms. More recently, Jabalera *et al.*³⁴ designed the AS-48-BMNP nano-assembly, where biomimetic magnetic nanoparticles (BMNPs) were simultaneously used as drug carriers and hyperthermia agents, and the circular antimicrobial peptide AS-48 was used as the active antimicrobial compound. The nano-assembly showed strong bactericidal effects on the planktonic cultures of both Gram-positive and Gram-negative bacteria, with the effects being remarkable against the Gram-negative species (*Pseudomonas aeruginosa* and *Klebsiella pneumoniae*), which are naturally resistant to AS-48. Notably, BMNP nano-assemblies can be magnetically guided and/or concentrated at the target¹⁵⁵.

The therapeutic approach is more challenging when the disease is caused by intracellular bacteria, such as *M. tuberculosis*¹⁵⁶. This pathogen reaches the lungs of infected individuals, where it is phagocytosed by alveolar macrophages forming

intracellular acidic vesicles named phagosomes. In many cases, *M. tuberculosis* prevents phagosome maturation and, hence, escapes from eradication by the host cell and turns the phagosome into a niche for cell replication. Infected macrophages stimulate the immune system, triggering the formation of cellular superstructures, the granulomas, which contain the infected macrophages and prevent antituberculosis drugs from reaching the pathogen¹⁵². To successfully treat this kind of pathogens by a magnetically directed therapy, the availing of a carrier that can penetrate granulomas and locally increase drug bioavailability is crucial. Therefore, for the nano-formulation, the already designed AS-48-BMNPs have to, e.g., carry the bacteriocin, allow magnetic driving, ensure stability at the physiological pH, release the bacteriocin at the target, and behave as hyperthermia agents. However, this nano-formulation needs to be optimized to enhance cellular uptake, reduce the toxicity of AS-48 for non-infected cells, and ensure intracellular drug release.

MamC-mediated biomimetic magnetic nanoparticles have proven to be suitable nanocarriers for directed combined therapy^{34,157}. These BMNPs are chemically produced by introducing a magnetosome protein from *Magnetococcus marinus* MC-1, MamC (expressed as a recombinant protein), in the reaction mixture from which magnetite nucleates grow. MamC chelates Fe cations and acts as a template for magnetite nucleation, producing magnetic nanoparticles in different sizes, surface charges, and magnetic properties from those chemically produced (MNPs). In terms of size, BMNPs are larger (~35–40 nm) than MNPs (<20 nm), which allows BMNPs to be superparamagnetic and to display a larger magnetic moment per particle than that displayed by MNPs. This characteristic ensures an enhanced magnetic response once an external magnetic field is applied for guidance and/or concentration and favours a non-magnetic behaviour of BMNPs in the absence of an external magnetic field, which prevents BMNP aggregation¹⁵⁵.

In terms of surface charge, the advantage of using BMNPs versus MNPs is mainly related to the greater ease in the process of functionalization. MNPs usually have an isoelectric point close to 7; thus, they need to be coated to successfully bind the relevant molecule and to keep the nano-assembly at the physiological pH stable^{158,159}. Instead, in the case of BMNPs, MamC confers to the nanoparticle-surface

functional groups, which switch their isoelectric points to ~ 4.5 ¹⁵⁷. This is important since, as the nanoparticle is negatively charged at the physiological pH, drug-binding by electrostatic interaction and nano-assembly stability at this pH value are ensured, drug release is triggered in acidic environments as BMNPs become uncharged¹⁵⁷, and BMNPs behave as stimulus-response drug delivery systems. Furthermore, BMNPs are hyperthermia agents that are able to locally raise the temperature to the hyperthermia therapeutic range (41–45 °C) following the application of an alternating magnetic field (AMF)^{35,160}, which further increases the drug release at the target^{161–163}.

Novel compounds with unexploited mechanisms of action are required to deal with bacterial infections. Among them, the bacteriocin AS-48 is a cationic 70 residues-long head-to-tail cyclized peptide produced by *Enterococcus faecalis* with a potent bactericidal effect on Gram-positive bacteria^{164,165}, including several human pathogens^{166,167}. AS-48 is very stable in a broad range of conditions (pH, temperature, salt concentrations) and resistant to most proteases. This antimicrobial peptide in solution is arranged in two different dimeric forms as a function of the physico-chemical environment: dimeric form I (DF-I), in which the molecules are linked by hydrophobic interactions (hydro-soluble form), and dimeric form II (DF-II), in which the molecules are linked by hydrophilic interactions (hydrophobic form). Basically, the bactericidal effect is electrostatic dependent and is exerted by the accumulation of DF-I on the negatively charged membrane, followed by dissociation into DF-II and insertion into the lipid bilayer, which causes the creation of pores¹⁶⁸. The antibacterial action is based on a receptor-independent mechanism, thus reducing the development of stable and transmissible resistance¹⁶⁶. Additionally, AS-48 has not shown any remarkable toxicity in preclinical studies, indicating its safety at preventing and treating infections, even those caused by MDR microorganisms¹⁶⁹. However, Gram-negative bacteria show naturally increased resistance to AS-48 due to the presence of the outer membrane. The nano-assembly AS-48-BMNPs combine the thermal and mechanical damages of the outer membrane induced by the rotation of the BMNPs (under an AMF stimulus), in such a way that the bacteriocin

can reach the cytoplasmic membrane. In these conditions, AS-48 can exert antimicrobial effects even against microorganisms considered naturally resistant³⁴.

Despite the advances made to date, improving the cellular uptake of the nanocarriers is crucial to reach an intracellular pathogen. In this scenario, Vurro *et al.* and Jabalera *et al.*^{35,170} tested the PLGA encapsulation of BMNPs to enhance their internalization in U87MG and HepG2 cells, respectively. Polylactic-co-glycolic acid (PLGA) is a copolymer of the ester family, widely used to prepare nano- and microparticles for nanomedicine purposes^{24,171,172} when biocompatibility and biodegradability are required. Moreover, PLGA has been approved for human therapies by the Food and Drug Administration (FDA) and the European Medicines Agency (EMA)^{55,59}. The biocompatibility for human cells is strictly related to its spontaneous hydrolysis, which leads to the release of lactic and glycolic acid monomers that can be easily metabolized by cells through the Krebs cycle¹⁷². Nevertheless, while embedding compounds, such as those reported in Jabalera *et al.*³⁵, is relatively easy, the embedding of AS-48 is not trivial due to its ability to insert and induce permeability in lipid membranes¹⁷³. In fact, previous attempts to encapsulate AS-48 in liposomes yielded non-functional formulations. Therefore, being able to encapsulate a nano-formulation containing AS-48 means that the direction of this molecule is a real step forward in the potential use of this bacteriocin.

The present study focuses on the design of a nano-formulation that allows the combination of directed chemotherapy and local hyperthermia and that could be potentially used against intracellular pathogens. Several nano-formulations based on AS-48-BMNP were optimized and characterized to improve cell uptake, reduce their toxicity in healthy (non-infected) cells, and delay bacteriocin release until the nano-formulation is inside the host. As a cell model, human macrophages (THP-1) are used since these cells are usually invaded by *M. tuberculosis*. This could be the first step toward a new approach in the treatment of diseases caused by intracellular pathogenic species, even if belonging to MDR strains, using a safe nanomaterial.

4.3 Experimental section

Several nanoformulations have been designed and characterized in the present study and are summarized in Table 8.

Table 8. Summary of the nano-formulations prepared and analyzed in the present study.

Nanomaterial	Description	Preparation Method
BMNPs	Biomimetic magnetic nanoparticles	Protein-mediated coprecipitation
AS-48-BMNPs	AS-48 immobilized on BMNPs	Ionic coupling
PLGA	Empty PLGA nanoparticles	Single emulsion
PLGA[BMNPs]	PLGA nanoparticles bearing BMNPs	Single emulsion
PLGA[AS-48-BMNPs]	PLGA nanoparticles bearing AS-48-BMNPs	Single emulsion

Biomimetic magnetic nanoparticles were synthesized by the protein-mediated coprecipitation method under anaerobic conditions (Table 8) following the protocol described in Valverde-Tercedor *et al.* ¹⁷⁴. MamC was produced and purified as a recombinant protein following a previously described protocol ¹⁷⁴. Briefly, transformed *Escherichia coli* TOP10 cells (Life Technologies: Invitrogen, Grand Island, NY, USA) were grown at 37 °C in Luria–Bertani (LB) broth supplemented with ampicillin, and the production of the MamC protein was induced with isopropyl- β -d-thiogalactopyranoside (IPTG, Fisher BioReagents, Pittsburgh, PA, USA). Once produced, the purification of the protein was carried out under denaturing conditions by fast protein liquid chromatography (FPLC, GE Healthcare) using immobilized metal affinity chromatography (IMAC, GE Healthcare, Chicago, IL, USA). Fractions containing MamC were refolded at 4 °C through dialysis in suitable buffers.

The synthesis of BMNPs was carried out at 1 atm of total pressure and 25 °C from oxygen-free solutions, at pH 9, following standard protocols ¹⁵⁷. All experiments were conducted under anaerobic conditions inside an anaerobic Coy chamber (96% N₂/4% H₂, Coy Laboratory Products, Grass Lake, MI, USA). Samples were incubated for 30 days, and then the solids, following magnetic concentration and

discarding the supernatant, were washed with deoxygenated Milli-Q water. The precipitated solid was stored in HEPES buffer (HEPES 10 mM, NaCl 150 mM, pH 7.4) and sterilized.

AS-48 was purified from cultures of the enterococcal UGRA10 strain [31] on Esprion 300 plus glucose (1%) (DMV Int., Veghel, Netherland) in a pH-controlled device following the conditions established by Ananou *et al.* Briefly, the fermentation supernatant was purified by cationic exchange chromatography on a Sepharose Big Beads resin (GE Amershan) and the eluted fractions were applied to a hydrophobic C18 column, to finally be purified to homogeneity by reverse-phase, high-performance liquid chromatography (RP-HPLC) on a Vydac 218TP510 semipreparative column (the Separation Group, Hesperia, CA, USA). The concentration of purified derivatives, determined by measuring UV absorption at 280 nm in a Nanodrop, was converted to a protein concentration using the molecular extinction coefficient.

To produce AS-48-BMNPs nano-assemblies, 5 mg of nanoparticles were mixed with 1 mL of aqueous 100 μ M AS-48 in HEPES buffer (10 mM HEPES, 150 mM NaCl, pH 7.4), and the samples were incubated for 24 h³⁴. After the incubation time, the nano-assemblies were collected with a magnet, and pellets were carefully washed twice with 1 mL HEPES buffer. The supernatants were measured by UV-Vis spectroscopy at 280 nm and the non-adsorbed AS-48 was estimated using a calibration line and subtracted from the initial concentration suspension. Thus, the coupling efficiency was expressed as the percentage of AS-48 bound (AS-48(%)_{bound}) and calculated by the following equation, where AS-48_{fed} is the amount of the peptide used for the coupling, while AS-48_{lost} is the unbound amount quantified in the waste supernatants. Finally, the total bound amount was expressed per mg of magnetite.

$$AS - 48(\%)_{bond} = \frac{(AS - 48_{fed} - AS - 48_{lost})}{AS - 48_{fed}} \times 100$$

PLGA encapsulation protocol. The synthesis of the PLGA nano-formulation embedding BMNPs was achieved using the single emulsion–evaporation method (Table 8)^{37,38,86}. To avoid the aggregation phenomenon, we tested different concentrations of PVA (0.1–2%), and to reduce the loss of AS-48, we performed several trials varying the PLGA concentration (2.5–20 mg/mL); the BMNP concentration was kept constant (5 mg/mL). Additionally, the influences of different organic phases (acetone, acetonitrile, dimethyl sulphate, acetone/ethanol) on the nano-assembly formation were tested. Thus, the following protocol was optimized to achieve a stable hyperthermia agent within the nanometric range. Briefly, 10 mg of PLGA copolymer (in the presence of 5 mg of BMNPs or AS-48-BMNPs) were dissolved in 1 mL of organic solution (85% acetone and 15% ethanol) and dripped into 10 mL of polyvinyl alcohol (PVA) 1% aqueous solution under sonication. The obtained emulsion was left under shaking overnight to enhance the organic solvent evaporation. Finally, the nano-assemblies were collected using a magnet and washed 3 times with PBS pH 7.4 before being resuspended in the desired buffer.

Empty PLGA nanoparticles were prepared with the same procedure, just avoiding the presence of the payloads. In this case, PLGA nanoparticles were collected by centrifugation (15,550× g for 20 min) (Eppendorf Centrifuge 5804R) and washed three times with PBS. The final pellet was re-suspended in 1 mL of sterile PBS buffer and stored at 4 °C. In the case of the synthesis of the AS-48-BMNPs, all supernatants were measured by UV-Vis spectroscopy at 280 nm to check for the presence of residual amounts of AS-48, using the same calibration curve previously prepared. Thus, the encapsulation efficiency was expressed as the percentage of the bacteriocin loaded ($AS-48(\%)_{loaded}$) and calculated by the following general equation, where $AS-48_{fed}$ stands for the quantity bound to BMNPs and is used for the encapsulation process, while $AS-48_{lost}$ stands for the free AS-48 in the waste supernatants.

$$AS - 48(\%)_{loaded} = \frac{(AS - 48_{fed} - AS - 48_{lost})}{AS - 48_{fed}} \times 100$$

Physico-chemical Characterization of the Nano-Formulations. The nano-formulations obtained were characterized in terms of size (Nanoparticle Tracking Analysis–NTA- and Atomic Force Microscopy–AFM), surface charge (ζ -potential), and surface chemistry (Fourier Transformed Infra-Red, FT-IR). AFM is a scanning probe microscopy (SPM) based on atomic force interactions between the sample and a nanometric probe; the technique offers information about morphology and surface topography. The analysis was performed in dry mode on a mica disk. The AFM output is a direct estimate of the nanoparticle diameter [34]. Thus, the AFM analysis, 20 μ L drops of each previously sonicated sample, were deposited on 20 mm diameter mica discs. An NT-MDT Solver Promicroscope (Moscow, Russia), with a single-crystal silicon–antimony-doped probe and a gold-coated tip (NSG-01 from NT-MDT), was used to collect images. The microscope was calibrated using a calibration grating (TGQ1 from NT-MDT) to reduce non-linearity and hysteresis in the measurements. The obtained images were processed using the program Gwyddion¹⁷⁵, and a statistical analysis as a function of the diameters on 35 different nanoparticles of each sample was conducted.

The NTA analysis is based on the dynamic light scattering phenomenon where the diffusion coefficient of each tracked particle was calculated in an aqueous environment by the Stokes–Einstein equation. Therefore, NTA analyses yield the hydrodynamic radii of the nano-formulations¹⁷⁶. Analyses were performed from suspensions of the nano-formulations in PBS pH 7.4. The nanoparticle tracking analysis (NTA) was performed using a Malvern NanoSight NS300 instrument (Worcestershire, UK) on diluted samples (1:1000) at 25 °C. For each sample, 3 sequences of 30 s with 25 FPS were recorded. The data analysis was carried out using NTA 3.4 Build 3.4.003 software¹⁷⁷. Nanoparticle tracking analysis (NTA) was performed using a Malvern NanoSight NS300 instrument (Worcestershire, UK) on diluted samples (1:1000) at 25 °C. For each sample, three sequences of 30 s with 25 FPS were recorded. The data analysis was carried out using NTA 3.4 Build 3.4.003 software¹⁷⁶.

The ζ -potential of the nano-formulations at pH 7.4 and 25 °C (10 mM NaClO₄) was analyzed using a Nano Zeta Sizer ZS (ZEN3600, Malvern Instruments, Malvern, Worcestershire, UK). Before performing the measurements, samples were diluted 20 times obtaining a final concentration of BMNPs close to 0.25 mg/mL.

Lyophilized samples were characterized by an FTIR spectrometer (model 6600, Jasco, Japan) equipped with an attenuated total reflection (ATR) diamond crystal window (ATR ProOne). A total of 64 scans were collected in the wavenumber range from 4000 to 400 cm⁻¹, at 2 cm⁻¹ resolution.

Magnetic properties. An AC generator was used to perform the magnetic hyperthermia experiments. The experimental setup consisted of induction heating coils made up of four turns of water-cooled copper, a power supply, and a chiller to maintain the temperature of the coils. Samples were analyzed at a fixed frequency of 120 kHz and under three magnetic field strengths, 13, 17, and 23 kA/m measured at the center of the coil, with an AC magnetic probe (NanoScience Laboratories Ltd., Staffordshire, UK). These parameters were chosen for the application of the alternating magnetic field since they are below the limit established by Hergt and Duzt in 2017 ($H_f < 5 \times 10^9 \text{ Am}^{-1}\text{s}^{-1}$)¹⁷⁸ and were recently proposed by Herrero de la Parte et al. in 2022 [38] ($H_f < 9.59 \times 10^9 \text{ Am}^{-1} \text{ s}^{-1}$) as the biophysical limitations. All samples were previously thermostated at 37.0 ± 0.2 °C. The temperature increase as a function of time was measured with a fiber optic thermometer (Optocon AG, Dresden, Germany), and the specific absorption rate (SAR) and intrinsic loss power (ILP) of the different systems were calculated^{179,180} using Equations (1) and (2).

$$(1) \text{ SAR} = \left(\frac{C \times V_s}{m} \right) \frac{dT}{dt}$$

$$(2) \text{ ILP} = \frac{\text{SAR}}{f H_0^2}$$

where C is the volumetric specific heat capacity of the sample ($C_{\text{Water}} = 4185 \text{ J/LK}$), v_s is the sample volume (0.2 mL in the reported experiments), and m is the mass of solids in the sample (2 mg).

The photothermia experiments were performed in a microfuge tube (0.5 mL) containing 0.2 mL of suspension of the relevant nano-formulation in HEPES buffer. Nanoparticle concentrations were adjusted to $[\text{Fe}] = 19 \text{ mM}$. During the experiments, each sample was irradiated from the top with a NIR laser ($\lambda = 808 \text{ nm}$) at 0.5, 1, and 2 W/cm^2 and visualized with a thermography camera (Flir 60 with 320×240 pixels, IR resolution, and thermal sensitivity $<0.045 \text{ }^\circ\text{C}$; FLIR Systems, Inc., Wilsonville, Oregon, USA), to measure temperature increases.

Stability and Bacteriocin Release. The releases of AS-48 bacteriocin from PLGA[AS-48-BMNPs] and AS-48-BMNPs were analyzed at different temperatures (4 $^\circ\text{C}$, 20 $^\circ\text{C}$, and 37 $^\circ\text{C}$) and different pH values (7.4 and 5) by suspending the nano-assemblies in PBS and citrate buffers, respectively. The experiment was performed for one week and, at each specific time interval, the nano-assemblies were magnetically separated from the supernatant and resuspended in the fresh buffer to continue the time course experiment. The released bacteriocin was quantified from UV-Vis at 280 nm.

In addition, the release of AS-48 was identically analyzed following magnetic hyperthermia (frequency = 120 kHz, $H = 23 \text{ kA/m}$, 120 min) or photothermia treatment ($\lambda = 808 \text{ nm}$, at 1 W/cm^2 , 30 min). AS-48 release was indirectly analyzed over the time course experiment from the supernatants as detailed above. Each experiment was performed in triplicate for each condition.

Cell culture. The human leukemia monocytic cell line, THP-1, was obtained from the European Collection of Animal Cell Cultures (Salisbury, UK). The cells were cultured in RPMI-1640 containing 10% heat-inactivated FBS supplemented with 2 mM L-glutamine, 100 U/mL penicillin, and 100 $\mu\text{g/mL}$ streptomycin, in a humid atmosphere with 5% CO_2 at 37 $^\circ\text{C}$, and sub-cultured at a ratio of 1:10 once a week.

Cytotoxicity of the Nano-Assemblies. THP-1 cells were seeded onto 96-well black plates with clear bottoms (20,000 cells/well) in complete RPMI-1640 containing 10% FBS and were differentiated to macrophages adding 20 nM phorbol 12-myristate 13-acetate (PMA) to the medium for 48 h. Then, the culture medium was replaced with fresh medium/10% FBS and the different nano-assembly treatments were applied in a volume of 100 μ L. Macrophages were incubated for 48 h in the absence (control) or in the presence of different nano-formulations: BMNP (229 μ g/mL), AS-48 (32 μ g/mL), PLGA (457 μ g/mL), AS-48-BMNPs (229 μ g/mL BMNPs and 32 μ g/mL AS-48), PLGA[AS-48-BMNPs] (457 μ g/mL PLGA, 229 μ g/mL BMNPs and 32 μ g/mL AS-48). To determine the cell viability, the resazurin assay was conducted, adding to each well 10 μ L of 1 mM resazurin and determining the fluorescence at $\lambda_{ex} = 535/\lambda_{em} = 590$ nm, in a microplate reader (HTX Microplate Reader BioTek Instruments, Winooski, VT, USA).

Cellular Uptake and Iron Content Estimation. To determine the amounts of internalized BMNPs in the different nano-formulations, THP-1 cells were seeded in 12-well plates (300,000 cells/well) and treated with BMNPs (229 μ g/mL), AS-48-BMNPs (229 μ g/mL BMNPs and 32 μ g/mL AS-48), PLGA[BMNPs] (457 μ g/mL PLGA, 229 μ g/mL BMNPs), and PLGA[AS-48-BMNPs] (457 μ g/mL PLGA, 229 μ g/mL BMNPs and 32 μ g/mL AS-48). In all cases, the final concentration of BMNPs was 229 μ g/mL ($[Fe] = 2.97$ mM). Cells were incubated for 48 and 72 h and then trypsinized and transferred to 2 mL tubes and centrifuged at $8500\times g$ for 5 min. Afterward, to dissolve the cell pellet with internalized nanoparticles, 100 μ L of 37% HCl/10% H₂O₂ were added and maintained for 20 min at room temperature. Finally, 1 mL of 1% potassium thiocyanate in Milli-Q water was added to the tubing, and the absorbance at 490 nm was measured by UV–Vis spectroscopy. To obtain the percentage of endogenous iron ($Fe_{endogenous}$), the following equation was applied: where $Abs_{Fe(internalized)}$ is the absorbance collected by dissolving cell pellet, while $Abs_{Fe(fed)}$ stands for the absorbance of the desired nano-formulation.

$$Fe_{endogenous}(\%) = \frac{Abs_{Fe(internalized)}}{Abs_{Fe(fed)}}$$

Statistical analysis. Statistical analyses were performed using Excel (16.65 20209) for Mac. For in vitro biological analysis, data represent means \pm SEM of three independent experiments performed in triplicate, and statistical analyses were carried out using single-way ANOVA, with a Bonferroni' s post hoc test for the grouped analysis. Statistical differences between the treatments were considered significant at * $p \leq 0.05$, ** $p \leq 0.001$, *** $p \leq 0.0001$.

This work has been a part of an active collaboration between the University of Verona and the University of Granada

4.4 Results

4.4.1 Nano-Assemblies Physico-chemical Characterization

BMNPs were previously characterized¹⁷⁴, and they consisted of pure stoichiometric magnetite with an average size of 39 ± 7 nm (sizes from 10 to 70 nm) and an isoelectric point (iep) of ~ 4.1 . AS-48 was effectively coupled to BMNPs, yielding a load of 0.14 ± 0.04 mg AS-48/mg BMNPs. This load is consistent with that reported by Jabalera *et al*³⁴. Additionally, no AS-48 loss was observed during PLGA encapsulation. FTIR analyses were run to confirm the binding of AS-48, and the covering of the nano-assemblies with PLGA (Figure 25). The absorption bands at 800 and 900 cm^{-1} corresponded to the Fe-O bond of magnetite (Fe_3O_4) and were evident for both the BMNPs and the nano-assemblies, although the signal was less intense as the coating width increased (from AS-48-BMNPs) to PLGA[AS-48-BMNPs]. AS-48 and PLGA shared common adsorption bands within the region 1100–1500 cm^{-1} . There were also distinctive bands for AS-48 at 801 and 837, 1543, 1656, 2936 cm^{-1} (C-C stretch, C=C bend, C=N bend, and O-H/C-H stretch, respectively). PLGA also showed distinctive bands at 862 and 1089, 1171, and 1752 cm^{-1} (C-C stretch, C-O stretch, and C=O bend). Many of these bands (1089, 1171, and 1752 cm^{-1}) can also be detected in PLGA[AS-48-BMNPs], showing the existence of the coating. Furthermore, the presence of AS-48 in PLGA[AS-48-BMNPs] was directly demonstrated by SDS-PAGE (Figure 26), in which a clear band close to 7000 Da, corresponding to AS-48 (expected size 7149.5 Da), can be observed in lanes where AS-48 from a pure stock and PLGA[AS-48-BMNPs] were loaded.

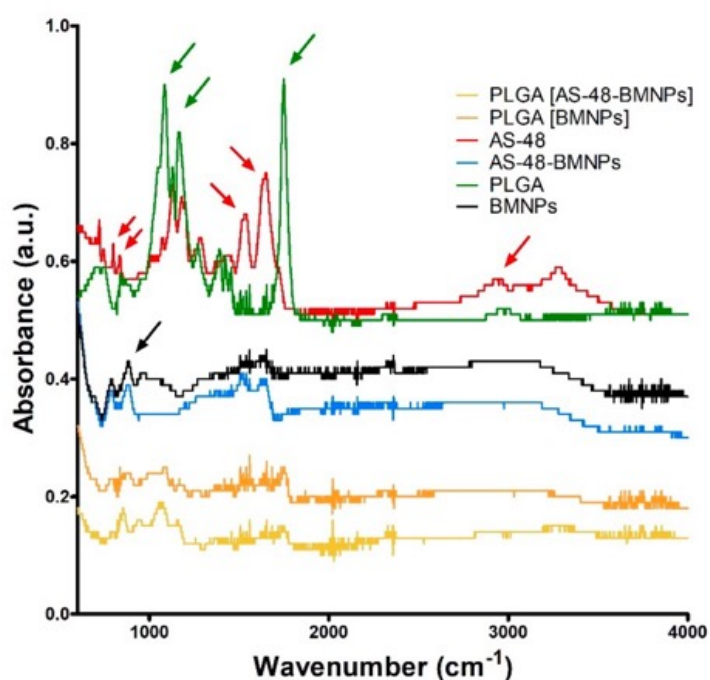


Figure 25. FTIR spectrum collected in the range between 600 and 4000 cm^{-1} . The black arrow stands for adsorption bands associated with magnetite (lines in black), AS48 distinctive adsorption bands are marked with red arrows and those for PLGA are marked with green arrows.

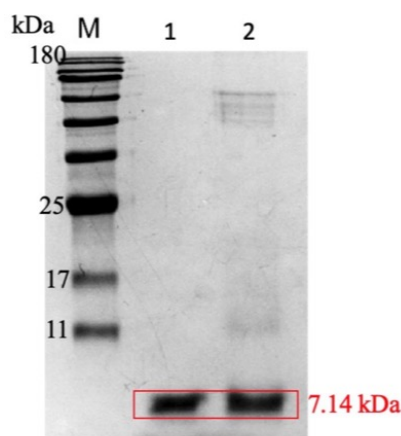


Figure 26. SDS-PAGE gel of the nano-formulation. Other than the marker (M), purified AS-48 (Lane 1) and PLGA[AS-48-BMNPs] (Lane 2) were loaded in the second and third lanes, respectively.

The size of each nano-formulation was estimated comparing two different techniques: nano-tracking analysis (NTA) and atomic force microscopy (AFM). NTA and AFM analyses of PLGA[BMNPs], PLGA[AS-48-BMNPs], AS-48-BMNPs,

BMNPs, and empty PLGA nanoparticles, yielded mode average sizes below 120 nm (Table 9). The discrepancy in NTA and AFM data for PLGA nano-formulations is mainly associated with artifacts during AFM measurements related to the expansion of soft PLGA on the mica surface, with the consequent increase in size⁸⁶. On the contrary, AFM data for harder materials, such as BMNPs, do not show such artifacts, with size data from both techniques (NTA and AFM) being comparable.

Table 9. NTA data compared to the AFM diameter. NTA average size represents the average obtained from three independent measures while the NTA mode size is the value most frequently detected. The values correspond to three independent experiments for which standard deviations were calculated.

Samples	NTA Average* (nm)	NTA Mode** (nm)	AFM Diameter (nm)
BMNPs	164 ± 87	107 ± 15	77 ± 35
AS-48-BMNPs	128 ± 100	67 ± 12	91 ± 50
PLGA	131 ± 26	117 ± 5	182 ± 29
PLGA[BMNPs]	173 ± 72	114 ± 9	201 ± 75
PLGA[AS-46-BMNPs]	160 ± 68	115 ± 7	228 ± 93

NTA size distributions of BMNPs (Figure 27a) showed several populations with sizes of 35, 63, 99, 149, and 229 nm, although the highest percentage of BMNPs was 99 nm. The average TEM size for the nanoparticles in this batch of BMNPs was 39 nm¹⁷⁴ and, therefore, it can be inferred that, although there were monodisperse BMNPs nanoparticles (NTA size of 35 nm), most BMNPs were aggregated in clusters of 2 to 3 BMNPs (NTA size of 99 nm). Regarding AS-48-BMNPs, most of the population exhibited sizes of 45 and 67 nm, although higher sizes of 131 and 181 nm were also detected.

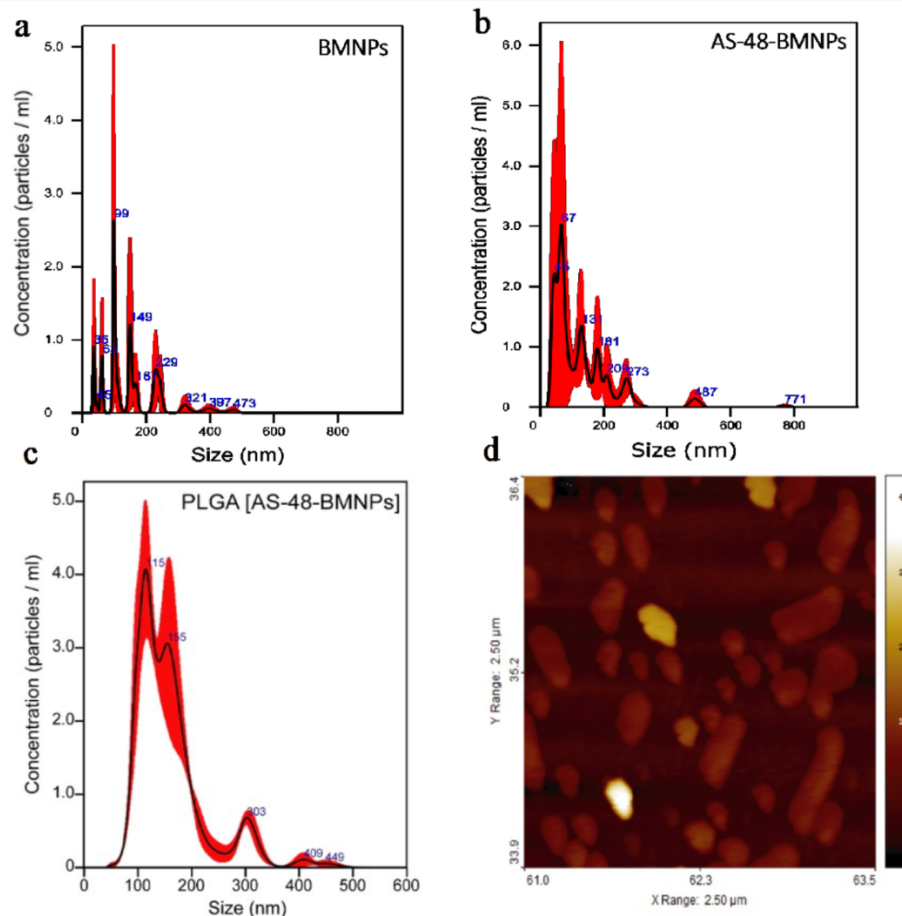


Figure 27. NTA size distribution of (a) BMNPs, (b) AS-48-BMNPs, and (c) PLGA[AS-48-BMNPs]. (d) AFM analysis of PLGA[AS-48-BMNPs].

PLGA[AS-48-BMNPs] preparation was optimized using PVA 1%, 10 mg of PLGA, 5 mg of BMNPs, and a mixture of acetone/ethanol with a ratio of 85/15. Indeed, lower concentrations (<1%) of the surfactant led to greater aggregation resulting in an increase in size; while a concentration greater than 1% did not bring more benefits. The polymer concentration used was the best one able to reduce the AS-48 loss while maintaining the nanometric size of the nano-assembly. Furthermore, among the different organic phases used (acetone, acetonitrile, dimethyl sulphate), only the mixture of acetone and ethanol did not negatively influence the binding between the peptide and BMNPs. Two well-defined populations with sizes of 115 and 155 nm (Figure 27c) were observed.

ζ -potential measurements of all nano-formulations at physiological pH show that they display negative surface charges (Table 10). For BMNPs, this negative charge is due to the carboxylic and hydroxyl groups present in MamC, which allow the electrostatic interactions with the cationic AS-48 through the amine groups of the peptide³⁴. The binding of AS-48 to BMNPs blocks some of the negatively charged functional groups, thus becoming the surface less negative (Table 10, -32 mV for BMNPs, -15 mV for AS-48-BMNPs). PLGA[BMNPs] and PLGA[AS-48-BMNPs] showed the ζ -potential of -19 ± 7 and -14 ± 6 mV, respectively (Table 10). In acid environment a zero net charge of the BMNPs) was collected, while AS-48-BMNPs reached a positive value of $+10 \pm 5$ mV. Since the $-\text{CHCOOH}$ groups were almost all protonated, PLGA negative surface charge decreased from -10 ± 5 mV collected at pH 7.5 to -1 ± 0.2 mV at pH 5. Same behaviour was observed for PLGA[BMNPs] and PLGA[AS-48-BMNPs] which showed ζ -potential values of -3 ± 1 mV and $+4 \pm 2$ mV respectively.

Table 10. ζ -Potential (mV) values at physiological and acidic conditions, pH 7.4 and pH 5, respectively. The data correspond to the average of three independent experiments for which the standard deviation has been calculated.

Nanoformulation	ζ -Potential (mV)	
	pH 7.4	pH 5
BMNPs	-32 ± 6	-6 ± 5
AS-48-BMNPs	-15 ± 4	$+10 \pm 5$
PLGA	-10 ± 3	-1 ± 0.2
PLGA[BMNPs]	-21 ± 6	-3 ± 1
PLGA[AS-46-BMNPs]	-18 ± 4	4 ± 2

4.4.2 Magnetic hyperthermia

All nano-formulations tested (BMNPs, PLGA[BMNPs], AS-48-BMNPs, and PLGA[AS-48-BMNPs]) were able to raise the temperature to the so-called therapeutic temperature (40–45 °C, transparent grey band) following their exposure to an alternating magnetic field (AMF) (Figure 28). Table 11 presents the summary of the specific absorption rate (SAR) and intrinsic loss power (ILP) for each nano-formulation. This temperature increase was dependent on the magnetic field strength of the AMF. The fastest and higher temperature increase occurred for BMNPs, for which in only ~15 s the therapeutic temperature was achieved, even at the lowest intensity of AMF (Figure 28a).

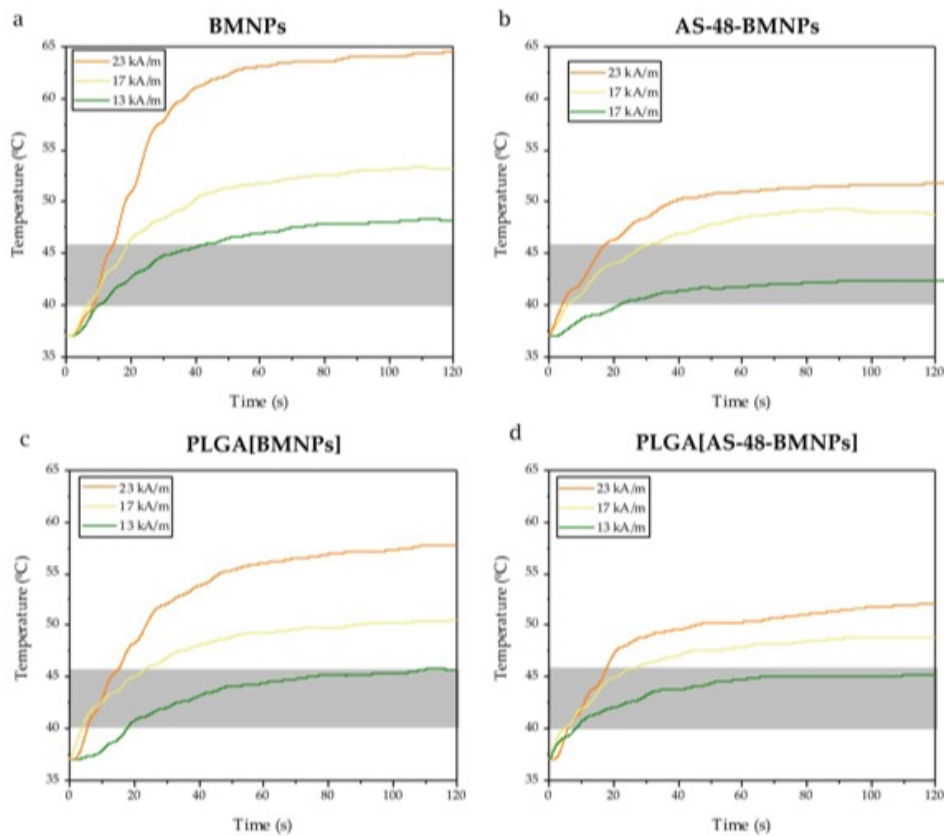


Figure 28. Time evolution of the temperature increase caused by (a) BMNPs, (b) AS-48-BMNPs, (c) PLGA[BMNPs], and (d) PLGA[AS-48-BMNPs] following exposure to AMF of different magnetic field strengths (13, 17, 23 kA/m) at a fixed frequency of 120 kHz. The transparent grey band shows the therapeutic temperature.

Table 11. Summary of SAR (specific absorption rate) and ILP (intrinsic lose power) calculations concerning the several samples at different intensities and at fixed frequency of 120 kHz, after 30 seconds of exposure. Sample volume 0.2 ml.

Samples	Field (kA/m)	SAR (W/g)	ILP (nHm²kg⁻¹)
BMNPs	13.4 ± 0.2	373 ± 29	20.0 ± 1.5
	17.7 ± 0.2	595 ± 40	18.7 ± 1.2
	23.3 ± 0.2	1210 ± 130	20.8 ± 2.1
Samples	Field (kA/m)	SAR (W/g)	ILP (nHm²kg⁻¹)
PLGA[BMNPs]	13.4 ± 0.2	252 ± 23	13.6 ± 1.1
	17.7 ± 0.2	416 ± 30	13.1 ± 1.0
	23.3 ± 0.2	760 ± 50	13.0 ± 0.9
Samples	Field (kA/m)	SAR (W/g)	ILP (nHm²kg⁻¹)
AS-48-BMNPs	13.4 ± 0.2	193 ± 12	10.4 ± 0.7
	17.7 ± 0.2	322 ± 30	11.6 ± 1.9
	23.3 ± 0.2	625 ± 30	10.7 ± 0.6
Samples	Field (kA/m)	SAR (W/g)	ILP (nHm²kg⁻¹)
PLGA[AS-48-BMNPs]	13.4 ± 0.2	314 ± 21	16.9 ± 1.1
	17.7 ± 0.2	440 ± 40	13.8 ± 1.1
	23.3 ± 0.2	836 ± 100	14.4 ± 1.7

4.4.3 Photothermia

As observed with magnetic hyperthermia, the nano-formulations tested were able to increase the temperature after a few seconds following laser exposure ($\lambda = 808$ nm) at a laser power density ranging from 1 to 2 W/cm². Applying 0.5 W/cm² was not enough to enhance the hyperthermia response. Again, the rate of the temperature increases, and the final temperature reached were dependent on the laser power density. In almost all of the nano-formulations, the therapeutic temperature was only reached at ≤ 40 s following laser exposure at the highest laser power density (Figure 29). A summary of the calculation of the specific absorption rate (SAR) for all nano-formulations at different laser power densities is presented in Table 12.

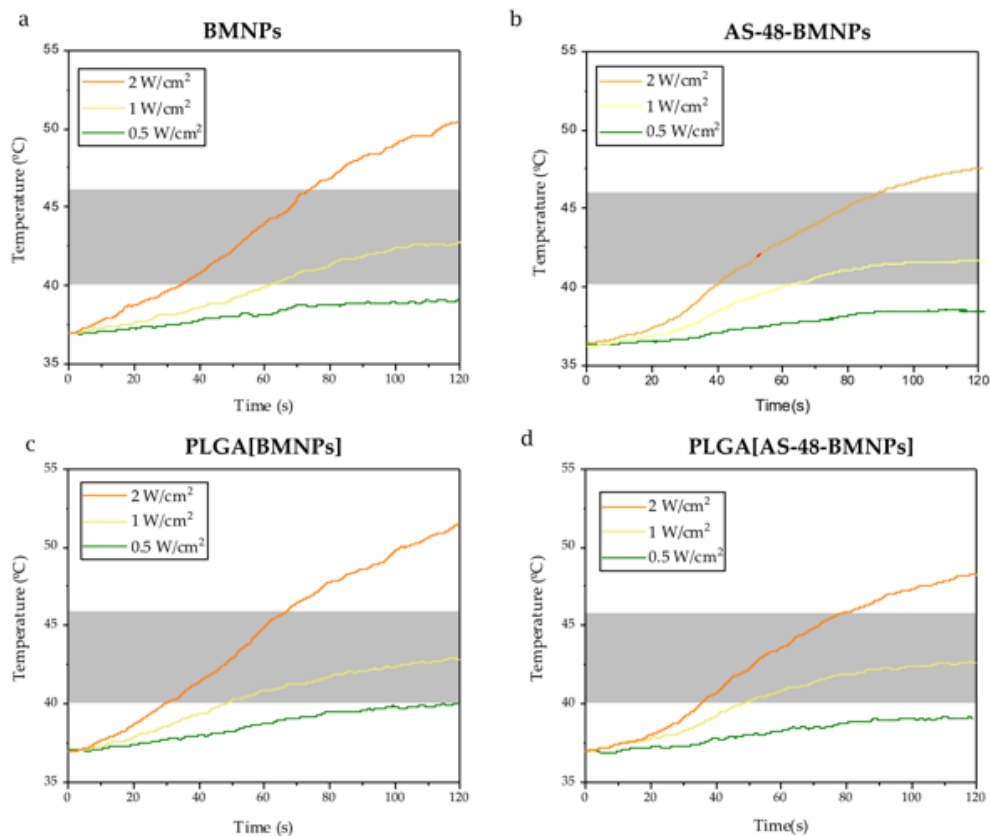


Figure 29. Time evolution of the temperature increase caused by (a) BMNPs, (b) AS-48-BMNPs, (c) PLGA[BMNPs], and (d) PLGA[AS-48-BMNPs] following exposure to different laser power densities (0.5, 1, 2 W/cm²). The transparent grey band shows the therapeutic temperature.

Table 12. Summary of the calculation of SAR (specific absorption rate) for all the samples at different laser power densities after 30 seconds of exposure. Sample volume 0.2 ml.

Samples	Power (W/cm²)	SAR (W/g)
BMNPs	0.5 ± 0.1	13.5 ± 1.3
	1.0 ± 0.1	37.1 ± 1.3
	2.0 ± 0.1	70.4 ± 2.9
Samples	Power (W/cm²)	SAR (W/g)
PLGA[BMNPs]	0.5 ± 0.1	14.9 ± 1.5
	1.0 ± 0.1	36.9 ± 1.3
	2.0 ± 0.1	80.7 ± 1.5
Samples	Power (W/cm²)	SAR (W/g)
AS-48-BMNPs	0.5 ± 0.1	18.3 ± 2.8
	1.0 ± 0.1	46.2 ± 2.1
	2.0 ± 0.1	78.0 ± 2.0
Samples	Power (W/cm²)	SAR (W/g)
PLGA[AS-48-BMNPs]	0.5 ± 0.1	18.3 ± 2.8
	1.0 ± 0.1	46.2 ± 2.1
	2.0 ± 0.1	78.0 ± 2.0

4.4.5 Stabilities and release pattern

Data in Figure 30 show that there is a release of AS-48 [AS-48 release (%)] from both nano-assemblies, AS-48-BMNPs and PLGA[AS-48-BMNPs], dependent on the pH, temperature, and the combination with hyperthermia. The release of AS-48 is favoured at high temperatures for both pH values. In fact, at physiological pH (pH 7.4), the release percentage of AS-48 reached a maximum of 10%, 30%, and 45% for temperatures of 4, 20, and 37 °C, respectively, but when temperature increased to 45 °C, following laser application, the release of AS-48 reached ~60% (Figure 30b). An identical trend was observed at pH = 5. The release percentage of AS-48 reached maximums of 20%, ~48%, and ~70% for temperatures of 4, 20, and 37 °C, and it reached 80% following laser exposure (Figure 30c,d). In all cases, the release of AS-48 from the nano-formulations was higher at acidic pH values compared to those of physiological pH values. On the one hand, pH = 5 is close to the isoelectric points of BMNPs, so the nanoparticles do not exhibit the negative charges at higher pH values, which were responsible for the electrostatic binding between the BMNPs and the cationic groups of AS-48³⁵. Once detached from BMNPs, the AS-48 released from the PLGA embedding is also favoured at acidic pH values, as acidic environments trigger PLGA hydrolysis into its by-products, i.e., polylactic acid and polyglycolic acid¹⁸¹.

Identically, thermal energy was previously shown to weaken the electrostatic bond and trigger a drug release³⁵. Therefore, the lowest rate of the AS-48 release from the nano-formulations was observed at 4 °C (<10% in 7 days), while the faster and more intense release (~80%) occurred after only 30 min at acidic pH values under high temperatures induced by photothermia (45 °C). It was remarkable to note the difference in the time scale for AS-48 release between conditions with and without external stimuli, such as magnetic hyperthermia or photothermia. In the case of photothermia, 80% release occurs in the first 30 min and in magnetic hyperthermia, 50% release is reached in only 120 min compared to one week for the same release under non-hyperthermia conditions.

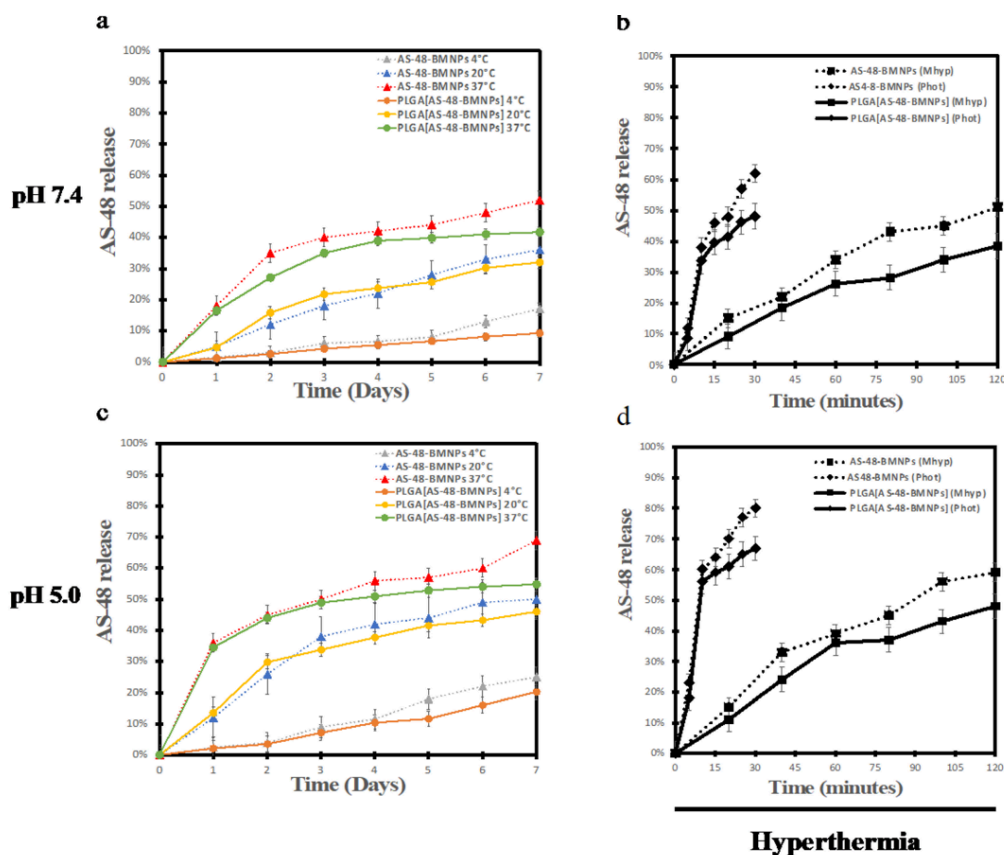


Figure 30. AS-48 released data from PLGA[AS-48-BMNPs] and AS-48-BMNPs in PBS pH 7.2–7.4 (a) and in citrate pH 5.0 (c) at different temperatures (4, 20, and 37 °C). AS-48 released data from the same nano-formulations following magnetic hyperthermia (Mhyp) and photothermia (Phot) applied for 120 and 30 min, respectively, at pH 7.2–7.4 (b) and pH 4.5–5.0 (d).

4.4.6 In vitro studies

One crucial characteristic in an efficient drug delivery nano-formulation is the ability to increase cellular internalization, which, in our case, was quantified as iron uptake, and then translated as the % of BMNPs internalized (Figure 31). While 42% (96.18 $\mu\text{g/mL}$) of the BMNPs incubated for 48 h were internalized in THP-1 cells (and 48% (109.92 $\mu\text{g/mL}$) at 72 h), higher percentages were obtained at 48 h for PLGA[BMNPs] and PLGA[AS-48-BMNPs] (56% (128.24 $\mu\text{g/mL}$) and 66% (151.14 $\mu\text{g/mL}$), respectively), and at 72 h (64% (146.56 $\mu\text{g/mL}$) and 78% (178.62 $\mu\text{g/mL}$), respectively). Furthermore, Figure 31b showed a brightfield microscopy picture after 72 h of treatment with PLGA[AS-48-BMNPs], in which no signs of cytotoxicity are shown in the cells.

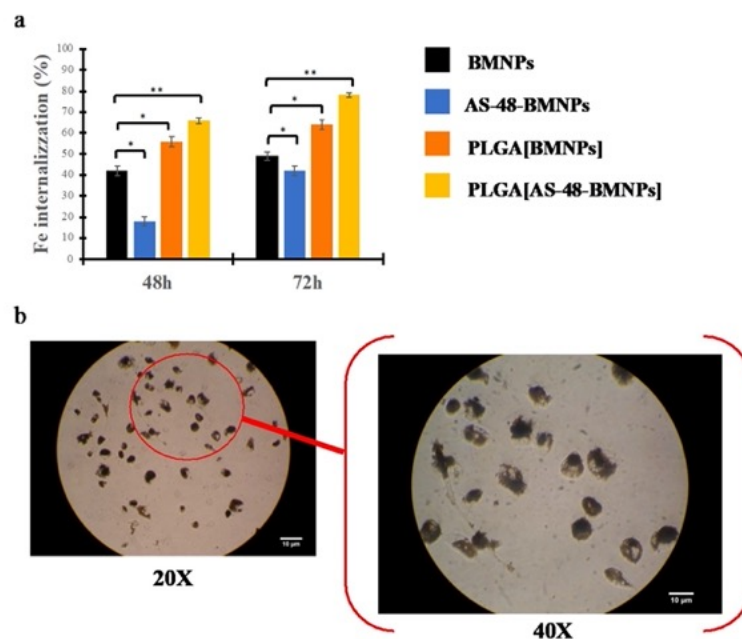


Figure 31. (a) Quantitative analysis of BMNPs by measuring the Fe content inside the macrophages after 48 and 72 h in TH1-P cell line following treatment with BMNPs (229 $\mu\text{g/mL}$), AS-48-BMNPs (229 $\mu\text{g/mL}$ BMNPs and 32 $\mu\text{g/mL}$ AS-48), PLGA[BMNPs] (457 $\mu\text{g/mL}$ PLGA, 229 $\mu\text{g/mL}$ BMNPs), PLGA[AS-48-BMNPs] (457 $\mu\text{g/mL}$ PLGA, 229 $\mu\text{g/mL}$ BMNPs and 32 $\mu\text{g/mL}$ AS-48). (b) Brightfield microscopy of THP-1 cells treated 72 h with PLGA[AS-48-BMNPs] * $p \leq 0.05$, ** $p \leq 0.001$.

Data in Figure 32 show that BMNPs and PLGA are cytocompatible for healthy (non-infected) THP-1 cells (>85% and >95%, respectively, cell survival after the treatment), while <3% THP-1 survival occurred following treatment with soluble AS-48 (32 µg/mL < MIC for *M. tuberculosis*¹⁸²). By coupling AS-48 to BMNPs, the viability of healthy macrophages increased up to 70%; furthermore, including AS-48-BMNPs in PLGA results in an increase in healthy THP-1 viability (up to 80%). This result is of particular interest; although PLGA[AS-48-BMNPs] shows the highest internalization, it also shows the lowest toxicity for healthy macrophages.

These results highlight the importance of shielding healthy cells from the interaction with free AS-48 since the administration of soluble AS-48 alone at these concentrations results in being highly toxic for healthy, non-infected, macrophages.

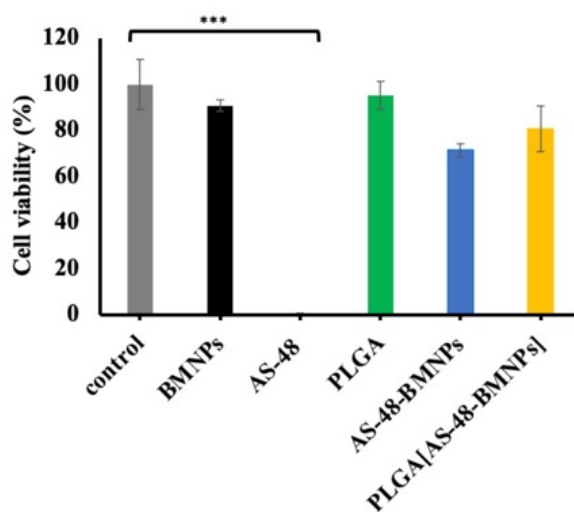


Figure 32. Viability assay in TH1-P cell line following treatment with culture medium (control), BMNPs (229 µg/mL), AS-48 (32 µg/mL), PLGA (457 µg/mL), AS-48-BMNPs (229 µg/mL BMNPs and 32 µg/mL AS-48), PLGA[AS-48-BMNPs] (457 µg/mL PLGA, 229 µg/mL BMNPs and 32 µg/mL AS-48). *** $p \leq 0.0001$ when compared to control values.

4.5 Discussion

BMNPs and AS-48-BMNPs dimensions were previously investigated by TEM technique^{163,174}. Thus, we decided to analyse all the sample by Nano-tracking Analysis (NTA) to investigate the hydrodynamic radius and then we compared the results with Atomic force Microscopy (AFM). Our results suggested: (1) AS-48-BMNPs mostly consisted of monodisperse populations of (non-aggregated) individually covered BMNPs, and (2) there were different sizes related to the covering of individual BMNPs (i.e., 45 and 67 nm). On the one hand, BMNP aggregation seemed to be prevented in the presence of AS-48, providing AS-48-BMNP nanoformulations with higher colloidal stability. Since BMNPs are superparamagnetic, the BMNP aggregation revealed in Figure 27a should be related to electrostatic and/or hydrophobic interactions between the nanoparticles, likely within the MamC domains present at the BMNP surface¹⁵⁷. These forces changed when AS-48 was present: As AS-48 is strongly positively charged at this pH³⁴, a preferential electrostatic interaction may occur between AS-48 and BMNP that destabilizes the former BMNP cluster. On the other hand, AS-48 attaches to BMNPs following a cooperative model³⁴, in which AS-48 binds to either the BMNP surface and/or to the previously attached AS-48 molecules. This led to differences in the number of AS-48 molecules that are carried by a single BMNP, thus explaining the observed differences in the NTA population sizes.

The presence of BMNPs into PLGA was confirmed by comparing FTIR spectra of naked BMNPs and the ones covered by the polymer. Despite the identifying peaks of AS-48 were observed in the spectrum of AS-48-BMNPs, they were completely hidden by PLGA signal for the nanoassembly PLGA[AS-48-BMNPs]. Nevertheless, the presence of the peptide was confirmed by SDS-Page as it is reported in figure 26.

PLGA covering procedure has been optimized to preserve, as much as possible, the electrostatic interaction between AS-48 and BMNPs to avoid the chance of losing

the peptide, while preparing nanoassembly in the nanometric range. These results were obtained using acetone:ethanol (85/15) as organic solvent and PVA as surfactant. The size range we obtained for PLGA[AS-48-BMNPs] was adequate to ensure enhanced permeability and retention (EPR) effect (<150 nm, ¹⁸³) and to allow an extended circulating time⁴². Notably, the embedding in PLGA improved the colloidal stability of this nano-formulation, as the size ranges of the nano-formulations in Figure 27c were narrower than those of BMNPs and AS-48-BMNPs. Differences within the two well-defined populations (115 and 150 nm) were likely caused by either the number of AS-48-BMNPs nano-assemblies enclosed in PLGA and/or the size of the enclosed individual AS48-BMNP nano-assemblies, related to differences in the number of the attached AS-48 molecules. Overall, all the nano-formulations were charged at physiological pH improving colloidal stability, as their aggregation were prevented due to electrostatic repulsion. Furthermore, covering AS-48-BMNPs with PLGA preserved the negative surface charges of the nano-assemblies, probably thanks to the carboxylic groups of the lactic and glycolic acid of PLGA. As pH decreased, the acidic functional groups were protonated, and the surfaces became less negative (Table 10). The roughly zero net charge (of the BMNPs) at pH = 5 was consistent with previous studies ¹⁵⁷. Covering AS-48-BMNPs with PLGA conferred the nano-formulations a net positive charge at acidic pH values, thus potentially favouring their interactions with the negatively charged cells without compromising the activity of AS-48, whose interactions with cell structures are most likely prevented until PLGA dissolution.

Once the colloidal stability was assessed, we tested the ability to raise the temperature to the killing one (hyperthermia temperature), when the nanoformulations were exposed to an alternating magnetic field. As BMNPs were covered by a non-magnetic covering (i.e., AS-48 and/or PLGA), the ability to raise the temperature slightly decreased, although PLGA[AS-48-BMNPs] was still able to reach the therapeutic temperature within 30 s upon AMF exposure (23 kA/m, 120 kHz frequency). This shielding of the magnetic core by a non-magnetic coating was observed by numerous authors ^{184,185} and, in particular, for the TAT-PLGA[DOXO-BMNPs]

nano-assembly by Jabalera *et al.*³⁵. The nanoparticles inside the polymeric coating are mechanically constrained, leading to a reduction in the freedom of rotation, which results in an impediment to Brownian relaxation. Moreover, the constraint increases the chance of an interaction between the particles inside the PLGA which hampers the Néel relaxation. Both relaxation patterns are crucial for the magnetic hyperthermia performance^{186–188}.

Again, BMNPs showed the faster raise temperature also when exposed to photo-thermic stimulus. Nevertheless, we observed a general decrease in the performance for AS-48. BMNPs. The attachment of AS-48 to the BMNPs decreased (but did not suppress) the ability of the nano-formulations to act as photothermal agents. This shielding in terms of photothermal behaviour of BMNPs was also observed by Jabalera *et al.* for TAT-PLGA (DOXO-BMNP)³⁵. The FTIR analysis showed that AS-48 has a peak close to 808 cm^{-1} (801 cm^{-1}); likely, the corresponding functional group (C-C) interfered with the photothermal performance by absorbing some of the radiation¹⁸⁷. After the peptide's absorption capacity was saturated, the heating rate increased linearly. Conversely, the PLGA polymer improved the response to hyperthermia (Figure 29a,b). Indeed, as observed for the silica coating¹⁸⁷, PLGA could modify the thermal conductivity of the solution by improving the heating rate¹⁸⁹.

According to the release rate experiments, pH 7.4 and 4 °C should be used for the storage and conservation of the nano-assemblies. In summary, BMNP-based nano-assemblies can be magnetically concentrated at the target in less than 1 h (mice model,¹⁵⁵). At physiological pH values, while being driven to the target, PLGA[AS-48-BMNPs] is stable (negligible AS-48 release, Figure 30a). Being positively charged, PLGA[AS-48-BMNPs] readily interact with and are internalized by THP-1 cells (Figure 31a), likely by endocytosis¹⁹⁰. At this point, environmental pH conditions change to more acidic environments^{191,192}, so the AS-48 release is triggered (Figure 30c). Moreover, once at the target, either magnetic hyperthermia

or photothermia is applied, and the temperature increases inside the cell further enhancing the AS-48 release in THP-1.

Interestingly, in terms of the AS-48 release rate, there was a trend observed in all experiments, such as the ability of PLGA to delay (in time) the AS-48 release. This result is important because the nano-formulation PLGA[AS-48-BMNPs] could be especially useful for longer treatments in which a delayed and lasting drug release is needed, for instance, to treat macrophages infected with *M. tuberculosis* ¹⁵².

The slightly higher internalization values of PLGA[AS-48-BMNPs] were consistent with their positive ζ -potential, which enhanced the electrostatic interaction between this nano-formulation and the negative cellular membrane. These results were consistent with those of Vurro *et al.* and Jabalera *et al.* ^{35,170}, in which BMNPs encapsulated in PLGA showed enhanced internalization in U87MG and HepG2 cells compared to non-encapsulated BMNPs, without affecting (in any case) cellular viability. PLGA likely promotes phagocytosis, overcoming BMNP internalization limits ¹⁹⁰.

Therefore, our data show that the nano-formulation PLGA[AS-48-BMNPs] could be a good candidate for the directed chemotherapy of AS-48, which could be combined with hyperthermia (magnetic hyperthermia and photothermia). This nano-formulation also enhances internalization and mediates a slow release of the bacteriocin suitable for extended antibacterial treatment and reduces the mortality of non-infected cells with respect to those treated with the free bacteriocin. Moreover, our hypothesis, which will be tested in the future, is that this nano-formulation allows non-infected macrophages to store AS-48 without affecting cell viability (for at least 72 h), likely preventing a spread if they are further infected by the pathogen. Experiments proving the activity of PLGA[AS-48-BMNPs] on *M. tuberculosis* inside infected macrophages are already under development.

4.6 Conclusion

These results show a slower AS-48 release from PLGA[AS-48-BMNPs] compared to previous nano-formulations, which could make this new nano-assembly suitable for longer extended treatments of intracellular pathogens. PLGA[AS-48-BMNPs] are internalized in THP-1 cells where AS-48 is released slowly, which may be useful to treat diseases and prevent infection caused by intracellular pathogens. The treatment will be more efficient when combined with hyperthermia or photothermia.

The nano-formulations (AS-48-BMNPs, PLGA[AS-48-BMNPs]) are suitable in terms of size and surface charge, and because they behave as hyperthermia agents, to allow the directed chemotherapy of AS-48 combined with hyperthermia therapies (both magnetic hyperthermia and photothermia). In particular, PLGA[AS-48-BMNPs] shows the slowest AS-48 release at physiological pH values (<15% AS-48 release within the first 24 h), indicating a low chance of bacteriocin loss while magnetically concentrating at the target (~1 h in mice model).¹⁵⁵ Moreover, this nano-formulation shows a high percentage of internalization in a model macrophage cell (>80%). The release of AS-48 from this nano-formulation is the slowest, which could be beneficial for extended treatments, but it can be accelerated up to 80% in minutes by combining with hyperthermia. Finally, this nano-formulation shows little cytotoxicity with respect to healthy (non-infected) cells, at least within the first 72 h. Therefore, little impact of this nano-formulation in healthy cells is expected while being guided/concentrated at the target. Furthermore, the internalization of these nano-formulations in healthy macrophages and the slow release of bacteriocin inside could prevent the pathogen from colonizing the cell and, thus, the spreading of the infection. Nevertheless, the present study only offers a proof of concept of a novel nano-formulation, whose performance are under test in the future in a real intracellular infection model.



Article

Embedding Biomimetic Magnetic Nanoparticles Coupled with Peptide AS-48 into PLGA to Treat Intracellular Pathogens

Salvatore Calogero Gaglio ^{1,†}, Ylenia Jabalera ^{2,†}, Manuel Montalbán-López ², Ana Cristina Millán-Placer ^{3,4}, Marina Lázaro-Callejón ⁵, Mercedes Maqueda ², María Paz Carrasco-Jimenez ⁶, Alejandro Laso ⁶, José A. Aínsa ³, Guillermo R. Iglesias ⁵, Massimiliano Perduca ^{1,*} and Concepción Jiménez López ^{2,*}

¹ Department of Biotechnology, University of Verona, Strada Le Grazie 15, 37134 Verona, Italy

² Department of Microbiology, Faculty of Sciences, University of Granada, 18071 Granada, Spain

³ Departamento de Microbiología, Pediatría, Radiología y Salud Pública (Facultad de Medicina) & BIFI, Universidad de Zaragoza, 50009 Zaragoza, Spain

⁴ CIBER de Enfermedades Respiratorias (CIBERES), Instituto de Salud Carlos III, 28029 Madrid, Spain

⁵ Department of Applied Physics and Instituto de Investigación Biosanitaria IBS. GRANADA, NanoMag Laboratory, University of Granada, 18071 Granada, Spain

⁶ Department of Biochemistry and Molecular Biology I, University of Granada, 18071 Granada, Spain

* Correspondence: massimiliano.perduca@univr.it (M.P.); cjl@ugr.es (C.J.L.)

† These authors contributed equally to this work.



Citation: Gaglio, S.C.; Jabalera, Y.; Montalbán-López, M.; Millán-Placer, A.C.; Lázaro-Callejón, M.; Maqueda, M.; Carrasco-Jimenez, M.P.; Laso, A.; Aínsa, J.A.; Iglesias, G.R.; et al. Embedding Biomimetic Magnetic Nanoparticles Coupled with Peptide AS-48 into PLGA to Treat Intracellular Pathogens. *Pharmaceutics* **2022**, *14*, 2744. <https://doi.org/10.3390/pharmaceutics14122744>

Academic Editor: Heejun Park

Received: 15 October 2022

Accepted: 4 December 2022

Published: 8 December 2022

Publisher's Note: MDPI stays neutral with regard to jurisdictional claims in published maps and institutional affiliations.



Copyright: © 2022 by the authors. Licensee MDPI, Basel, Switzerland. This article is an open access article distributed under the terms and conditions of the Creative Commons Attribution (CC BY) license (<https://creativecommons.org/licenses/by/4.0/>).

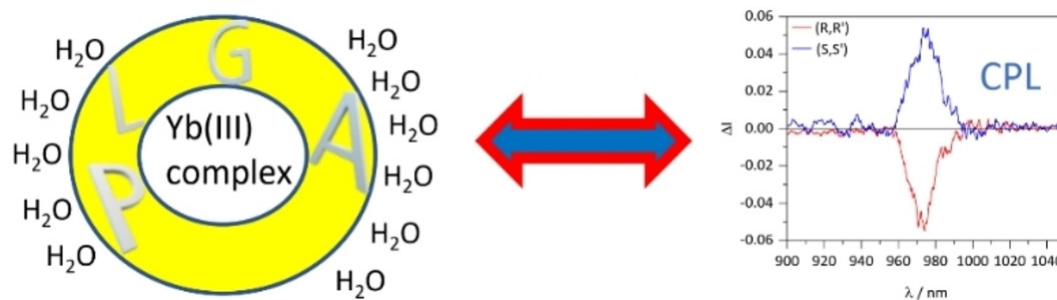
Abstract: Among the strategies employed to overcome the development of multidrug-resistant bacteria, directed chemotherapy combined with local therapies (e.g., magnetic hyperthermia) has gained great interest. A nano-assembly coupling the antimicrobial peptide AS-48 to biomimetic magnetic nanoparticles (AS-48-BMNPs) was demonstrated to have potent bactericidal effects on both Gram-positive and Gram-negative bacteria when the antimicrobial activity of the peptide was combined with magnetic hyperthermia. Nevertheless, intracellular pathogens remain challenging due to the difficulty of the drug reaching the bacterium. Thus, improving the cellular uptake of the nanocarrier is crucial for the success of the treatment. In the present study, we demonstrate the embedding cellular uptake of the original nano-assembly into THP-1, reducing the toxicity of AS-48 toward healthy THP-1 cells. We optimized the design of PLGA[AS-48-BMNPs] in terms of size, colloidal stability, and hyperthermia activity (either magnetic or photothermal). The stability of the nano-formulation at physiological pH values was evaluated by studying the AS-48 release at this pH value. The influence of pH and hyperthermia on the AS-48 release from the nano-formulation was also studied. These results show a slower AS-48 release from PLGA[AS-48-BMNPs] compared to previous nano-formulations, which could make this new nano-formulation suitable for longer extended treatments of intracellular pathogens. PLGA[AS-48-BMNPs] are internalized in THP-1 cells where AS-48 is liberated slowly, which may be useful to treat diseases and prevent infection caused by intracellular pathogens. The treatment will be more efficient combined with hyperthermia or photothermia.

Keywords: BMNPs; PLGA; AS-48; photothermia; hyperthermia; magnetic nanoparticles; antimicrobial peptide; monocytes; *Mycobacterium tuberculosis*

1. Introduction

Directed chemotherapy to treat local infections is not only necessary to avoid undesired secondary effects, but also to reduce the number of drugs needed to control the infection. This advantage becomes crucial in the context of antibiotics. In fact, the World Health Organization (WHO) is warning about the increase in the failure of common antibacterial therapies due to the development and selection of multidrug-resistant (MDR) bacteria, mainly due to the generalized and/or extended drug administration [1]. As an example,

NIR Circularly Polarized Luminescence from water stable organic nanoparticles containing a chiral Yb(III) complex



Cavalli *et al.* Chem. Eur. J. <https://doi.org/10.1002/chem.202200574>

5.1 Aim

Chiral small metabolic molecules are important to control physiological processes and verify the health status of humans. Changes in the enantiomer distribution in biofluids and tissues are related to several diseases, including cancer, kidney, and brain diseases.

Circularly polarized luminescence (CPL), as bioassay, could be employed for the detection of such chiral molecules. CPL provides insight into the excited state properties of chiral molecular systems linking differential emission intensity of right and left circularly polarized light. Current applications of circularly polarized luminescence (CPL) in bioimaging would greatly benefit from its extension and consolidation in the near-infrared (NIR) region, where tissues, skin, blood and water are quite transparent and scattering is also relatively low¹⁰. The 1000–1400 nm range is sometimes called the second biological window and it is emerging as a very attractive region for biological imaging. In general, lanthanide (Ln) complexes suffer from quenching phenomenon limiting their use in water environment.

In previous studies⁸⁶, we successfully showed an elegant solution to preserve Eu^{3+} complex emission in water environment such as PBS pH 7.4, a common buffer used for bioassay, thus we encapsulated the lanthanide into PLGA via single emulsion method. Interestingly, PLGA was able to preserve Eu emission in water environment by preventing multiphonon relaxation quenching, opening the way for using Ln complex in imaging applications. The reason why these kinds of complexes are interesting is related to the huge Stokes shift which allows the narrow-size emission pattern to be clearly recognized from the background. Near infrared range, where tissues, skin, blood and water are quite transparent and the scattering is very low, is widely used in imaging. Furthermore, 1000–1400 nm range is sometimes called the second biological window and it is emerging as a very attractive region for biological imaging. In this work, we designed the first example of very efficient NIR Circularly Polarized Luminescence (around 970 nm) in water, obtained thanks to

the combined use of a chiral Yb complex and of poly lactic-co-glycolic acid nanoparticles.

Being part of collaboration, we will describe here only the chemico-physical characterization of the nanoparticles, while the development of the dye and spectroscopy studies are available in the article⁶⁸. We thank prof. Fabio Piccinelli and his team for providing the complexes.

5.2 Introduction

The detection of specific disease-related biomarkers is an important feature for early diagnosis and therefore to increase the chances of treatment success. Several chiral small metabolic molecules are important to control physiological processes and provide clues on the health status of humans. Changes in the enantiomeric distribution of specific compounds in biofluids and tissues are related to several diseases¹⁹³. For instance, a reduction in D-Asp was observed in the substantia nigra of patients suffering Parkinson's disease¹⁹⁴. Abnormal concentrations of D-lactate and L/D-2-HG were detected in urine, plasma and saliva of patients with diabetes¹⁹⁵. Hepatocellular carcinoma causes a decrease in serum D-glutamic acid (D-Glu) and D-glutamine (D-Gln) in patients who develop the disease¹⁹⁶. Thus, chiral small molecules are suitable biomarkers for disease diagnosis, drug effect monitoring, and pharmacodynamic studies.

Circularly polarized luminescence refers to the differential emission of left versus right circularly polarized light that allows the study of chiral interactions of luminescent molecular systems, providing a new tool for the investigation of chiral molecules in biological complex systems. For instance, efficient CPL probe complexes, especially lanthanide coordination complexes, can be used to detect chiral molecules in cell imaging analysis¹⁹⁷. Current applications of circularly polarized luminescence (CPL) in bioimaging would greatly benefit from its extension and consolidation in the near-infrared (NIR) region, where tissues, skin, blood and water are quite transparent and scattering is also relatively low¹⁰. The 1000–1400 nm range is sometimes called the second biological window and it is emerging as a very attractive region for biological imaging. CPL in this region benefits from the specificity, selectivity and sensitivity, which are typical of the chiroptical counterpart of emission spectroscopy, in the context of biological applications, like microscopy and bioassays^{198–201}. Complexes of NIR emitting lanthanide ions like Yb(III), having small size and metal-centred emission properties, may provide good candidates, thanks to the 1 μm emission band of Yb(III), associated with its low toxicity and to

the well-known chemistry developed for using other lanthanides in biomedicine. Only few examples of such complexes have been reported within literature so far.^{11,202–204} In order to switch to practical applications of NIR-CPL in the field of bioassays, it would be important to devise systems that can be dissolved/dispersed in aqueous media while still retaining their (chiro) optical properties. With Yb(III)-based complexes this is challenging, because the emission efficiency of Yb(III) complexes in solution can be significantly affected by multiphonon relaxation (MPR) processes⁹.

In previous studies⁸⁶, we demonstrated poly lactic-co-glycolic acid (PLGA) is suitable for encapsulating and thus protecting organic molecules and metal complexes. In fact, once $[\text{EuL}(\text{tta})_2(\text{H}_2\text{O})]\text{CF}_3\text{SO}_3$ complex (Figure 33), where L stand for N, N'-bis(2-pyridylmethylidene)-1,2- (R,R or S,S) cyclohexanediamine, respectively, was embedded in PLGA, Eu red emission was collected in water environment upon excitation. These findings suggested that PLGA is suitable for preserving the so-called antenna effect by shielding the metal from water molecules. Since Yb complex share the same antenna structure of Eu complex we decided to verify once again, if PLGA nanoparticles could protect the NIR-emitting dye in water environment paving the way in the field of NIR-CPL bio-assays.

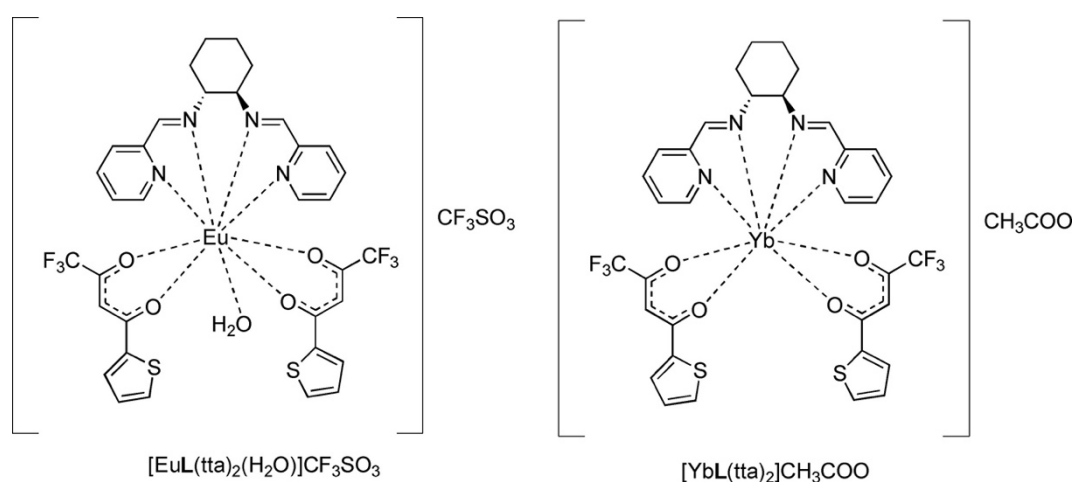


Figure 33. Molecular structure of the complexes discussed in this contribution. The R,R isomer of L ligand is reported.

5.3 Experimental section

Preparation of [YbL(tta)₂]·CH₃COO loaded PLGA nanoparticles. Loaded nanoparticles have been prepared by modifying the nanoprecipitation method reported in the work of Reisch *et al*⁶⁷. Firstly, 2 mg of PLGA and 1 mg of the complex were dissolved in acetonitrile. The polymeric solution was diluted 60 times into an aqueous phase of glycine pH 9. Nanoparticles are instantly formed by exploiting the nano precipitation. Subsequently, they were purified by two washing with water (centrifugation 11000rpm/ 30- 40 minutes) and then they were resuspended in the desired buffer. The same protocol was followed to prepare empty nanoparticles by avoiding the complex in the polymeric phase.

Physico-chemical Characterization of the Nano-Formulations. Nanoparticles obtained were characterized in terms of size (Nanoparticle Tracking Analysis-NTA Atomic Force Microscopy-AFM and Dynamic Light Scattering-DLS). Moreover, the colloidal stability was assessed by checking surface charge (ζ -potential).

Dynamic light scattering (Nano Zeta Sizer ZS ZEN3600, Malvern Instruments, Malvern, Worcestershire, UK) was performed by diluting samples (1:20) in PBS pH 7.4 before starting the analysis. The ζ -potential at pH 7.4 and 25 °C (10 mM NaClO₄) was also analysed.

Thus, for the AFM analysis, 20 μ L drops of each previously sonicated sample were deposited on 20 mm diameter mica discs. An NT-MDT Solver Promicroscope (Moscow, Russia), with a single-crystal silicon–antimony-doped probe and a gold-coated tip (NSG-01 from NT-MDT), was used to collect images. The microscope was calibrated using a calibration grating (TGQ1 from NT-MDT) to reduce non-linearity and hysteresis in the measurements. The obtained images were processed using the program SPIP[®], and a statistical analysis as a function of the diameters on different nanoparticles of each sample was conducted.

Nanoparticle tracking analysis (NTA) was performed using a Malvern NanoSight NS300 instrument (Worcestershire, UK) on diluted samples (1:1000) at 25 °C. For

each sample, three sequences of 30 s with 25 FPS were recorded. The data analysis was carried out using NTA 3.4 Build 3.4.003 software.

Encapsulation efficiency. The entrapped amount of lanthanide complex was estimated by absorbance spectroscopy. Briefly, PLGA NPs were dissolved in acetonitrile and the obtained solution was analysed using a calibration curve. Encapsulation efficiency was calculated by applying the following Equation:

$$EE(\%) = \frac{Ln\ complex_{loaded}}{Ln\ complex_{fed}} \times 100$$

5.4 Results

5.4.1 Physico-chemical characterization

To make the Yb(III) complex stable in aqueous solution, we prepared a nanof ormulation in which this complex is embedded in PLGA by means of a modified nanoprecipitation method at 20°C²⁰⁵ The obtained NPs showed a monodispersed distribution of the size as it is demonstrated by the NTA diagram (figure 35), in line with the small PDI of 0.053 ± 23 . By means of dynamic light scattering (DLS), the average size was 118 ± 3 and 102 ± 3 nm for the R,R and S,S enantiomers respectively with negative surface charge for both enantiomer (-13 mV). AFM picture shows round shaped nanoparticles confirming the size collected by NTA and DLS.

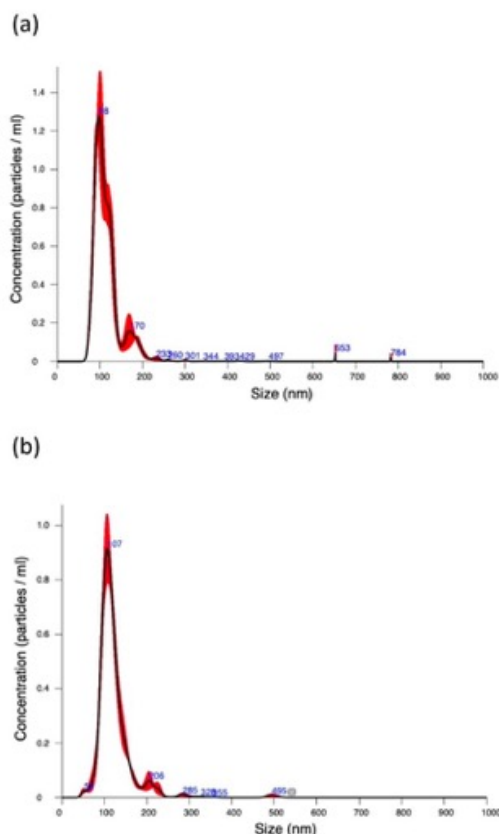


Figure 35. Nanotracking analysis (NTA) of (a) S,S and (b) R,R isomers of $[\text{YbL}(\text{tta})_2] \cdot \text{CH}_3\text{COO}$ loaded nanoparticles. Diagrams are obtained as average of three independent measurements.

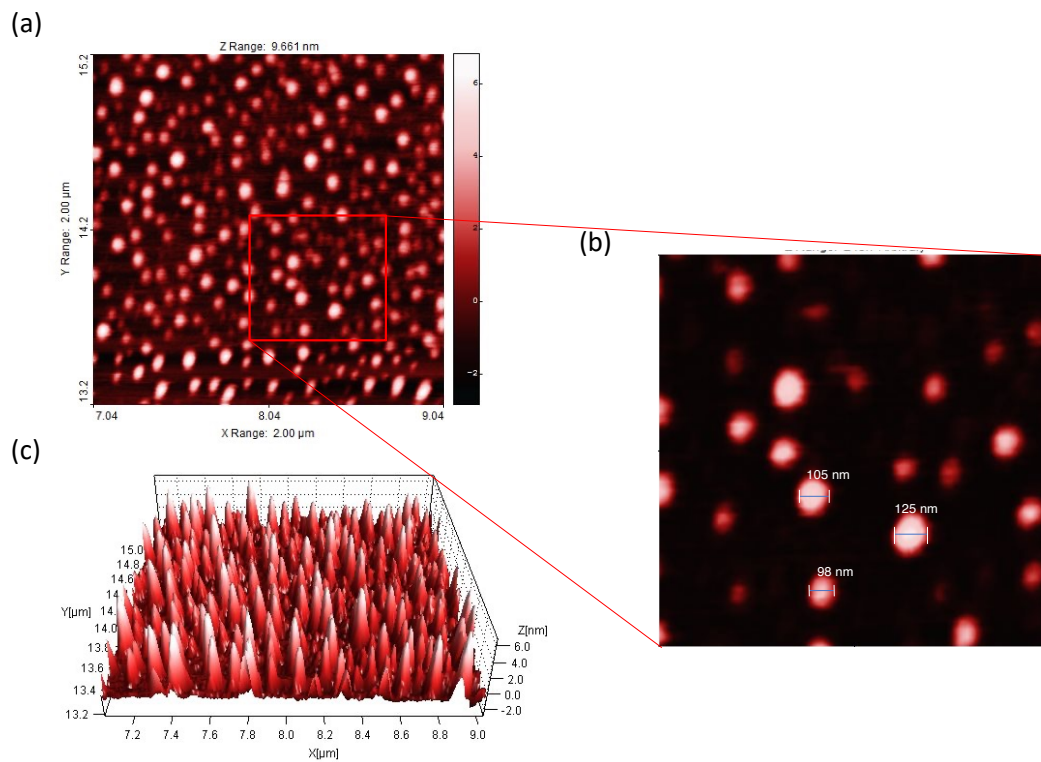


Figure 36. AFM images of PLGA NPs embedded with Yb(III) complex: (a) 2D image; (b) detail of a single section in which it is possible to observe the single nanoparticles with dimensions close to 100 nm; (c) 3D prospective.

5.4.2 Spectroscopy studies

The encapsulation efficiency was quantified by absorbance spectroscopy. As expected from both enantiomers, we achieved the same value of 64.5 ± 4.5 %. The luminescence emission spectra were fully consistent with those recorded in DCM, suggesting that the complexes preserve their identities when incorporated in the PLGA matrix (Figure 37).

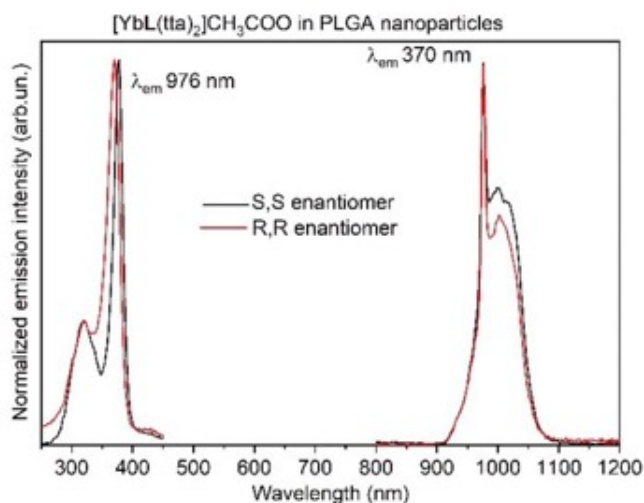


Figure 37. Excitation spectra (left) and emission spectra (right) of both enantiomers of Yb(III) complex embedded in PLGA nanoparticles, in aqueous solution. R,R (red line); S,S (black line).

Furthermore, the luminescence decay profile of the complexes embedded in PLGA-NPs is a double-exponential (Figure 38) with the dominant long-lived component having a time constant of 13 μ s and 11.7 μ s, for the S,S and R,R enantiomers, respectively; i.e. rather similar to that observed in DCM (Figure 38). The origin of the faster component of the decay is still unknown as it had been already observed in previous studies for Eu(III) complex⁸⁶. Likely, it could be a consequence of interactions of the molecules of the complex with each other or with the donor groups (i.e. OH and COOH) of the PLGA polymer.

Interestingly, the two enantiomers of $[\text{YbL}(\text{tta})_2] \cdot \text{CH}_3\text{COO}$ embedded in the NPs show again a NIR CPL mirror image (Figure 39b). In fact, these spectra are almost superimposable to those recorded in DCM solutions (Figure 39a).

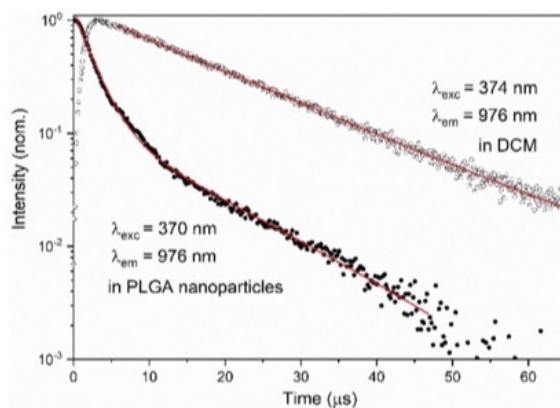


Figure 38. Comparison between the emission decay profiles of S,S - $[\text{YbL}(\text{tta})_2] \cdot \text{CH}_3\text{COO}$ in DCM solution and encapsulated in PLGA NPs in water solution.

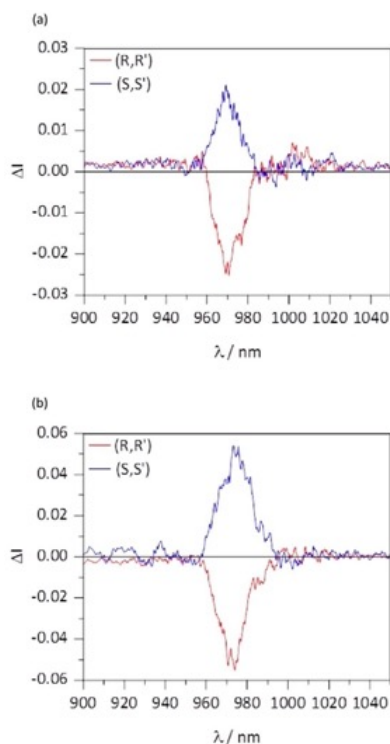


Figure 39. NIR CPL spectra of S,S (blue line) and R,R (red line) enantiomers of the $[\text{YbL}(\text{tta})_2] \cdot \text{CH}_3\text{COO}$ complex in DCM solution (a) and embedded in water stable PLGA polymer (b).

5.5 Discussion

In this work, we demonstrated the possibilities of using nanoprecipitation instead of single emulsion to prepare PLGA nanoparticles embedded with NIR-emitting lanthanide complexes. Nanoprecipitation led to smaller nanoparticles (~100 nm) than those prepared by single emulsion (~150-250 nm)⁸⁶. We prepared a monodispersed PLGA[Yb complex] colloidal suspension, stabilized by a negative surface charge of -13 mV. Interestingly, empty nanoparticles showed particles size close to 1000 nm suggesting the non-innocent role of the complex in the formation of the nanostructure. Furthermore, close interaction between PLGA and Ln complex could be demonstrated by the different emission decay in comparison with the free complex in DCM. These findings suggested no water molecules were present either in the inner or outer coordination spheres of the metal ion also in the PLGA environment. The double- exponential luminescence decay was observed also in previous studies⁸⁶ where we have highlighted the presence of two different species of the complex within the same nanoparticle. Although further studies are needed to better underline the interaction between the complex and the polymer, we have demonstrated that PLGA encapsulation technology does not perturb the luminescent quality of the lanthanides but preserves the NIR-CPL signal from quenching phenomena caused by water, enabling imaging and biological sensors applications. Remarkably, after one week, the NPs containing the complexes are still emissive and the shape of the decay curves remains almost identical, even though a decrease of the luminescence intensity is detected (data not shown).

5.6 Conclusion

In this work, we demonstrated the possibility to use nanoprecipitation instead of single emulsion to prepare loaded nanoparticles with hydrophobic compounds. Compared to single emulsion evaporation method, this one allows nanoparticles to be prepared in few minutes skipping *overnight* step. Nanoprecipitation allows to have dyes prepared on the spot and possibly 100% performing, which is a useful feature to increase the quality of biological investigations by imaging. Moreover, nanoprecipitation allowed to obtain nanoparticles smaller (~100 nm) than those of the single emulsion method used in several works (~150-250 nm): this could enhance penetration into tissues, easily overcoming natural barriers such as tight junctions of epithelial cells.

In conclusion, we demonstrated that PLGA nanoparticles are a suitable delivery system to incorporate the complex and protect the metal ion from the intrusion of solvent molecules, while ensuring biocompatibility, water solubility and stability to the complex. We gave a proof of concept in developing hydrophilic NIR-CPL optical probes based on Yb(III) complex and PLGA NPs. Therefore, PLGA nanoparticles incorporate the complex and protect the metal ion from the intrusion of solvent molecules, while ensuring biocompatibility, water solubility and stability to the complex.

Near Infrared Circularly Polarized Luminescence From Water Stable Organic Nanoparticles Containing a Chiral Yb(III) Complex

Enrico Cavalli,^[a] Chiara Nardon,^[b] Oliver G. Willis,^[c] Francesco Zinna,^[c] Lorenzo Di Bari,^{*,[c]} Silvia Mizzone,^[b] Silvia Ruggieri,^[b] Salvatore C. Gaglio,^[d] Massimiliano Perduca,^[d] Claudio Zaccone,^[e] Alessandro Romeo,^[f] and Fabio Piccinelli^{*,[b]}

Dedicated to Professor Marco Bettinelli on the occasion of his retirement

Abstract: We report the first example of very efficient NIR Circularly Polarized Luminescence (CPL) (around 970 nm) in water, obtained thanks to the combined use of a chiral Yb complex and of poly lactic-co-glycolic acid (PLGA) nanoparticles. $[\text{YbL}(\text{tta})_2]\text{CH}_3\text{COO}$ (L=N, N'-bis(2-pyridylmethylidene)-1,2-(R,R+S,S) cyclohexanediamine and tta=2-theynoltrifluoroacetate) shows good CPL in organic solvents, because the tta ligands efficiently sensitize Yb NIR lumines-

cence and the readily prepared chiral ligand L endows the complex with the necessary dissymmetry. PLGA nanoparticles incorporate the complex and protect the metal ion from the intrusion of solvent molecules, while ensuring biocompatibility, water solubility and stability to the complex. Hydrophilic NIR-CPL optical probes can find applications in the field of NIR-CPL bio-assays.

Introduction

Current applications of circularly polarized luminescence (CPL) in biomaging would greatly benefit from its extension and consolidation in the near-infrared (NIR) region, where tissues, skin, blood and water are quite transparent and scattering is also relatively low. The 1000–1400 nm range is sometimes called the second biological window and it is emerging as a very attractive region for biological imaging. CPL in this region benefits from the specificity, selectivity and sensitivity, which are typical of the chiroptical counterpart of emission spectroscopy, in the context of biological applications, like, for example microscopy and bioassays.^[1]

Complexes of NIR emitting lanthanide ions like Yb(III), having small size and metal-centred emission properties, may provide good candidates, thanks to the 1 μm emission band of Yb(III), associated with its low toxicity and to the well-known chemistry developed for using other lanthanides in biomedicine.

Moreover, in addition to biomedical applications, Yb-centred NIR-CPL may lend itself to several other technological fields, where vis-CPL allied to Eu or Tb have already demonstrated a positive impact.^[2]

NIR-CPL activity is indeed expected in the case of chiral Yb(III)-based complexes in which the spin allowed $^2F_{5/2} \rightarrow ^2F_{7/2}$ emission transition, around 980 nm, is characterized by a high value of the rotational strength^[3] and can be conveniently

[a] Prof. E. Cavalli
Department of Chemical Sciences, Life and Environmental Sustainability
Parma University
Parco Area delle Scienze, 11/a – 43124, Parma (Italy)

[b] Dr. C. Nardon, S. Mizzone, Dr. S. Ruggieri, Prof. F. Piccinelli
Luminescent Materials Laboratory, DB
Verona University
Strada Le Grazie 15, 37134, Verona (Italy)
E-mail: fabio.piccinelli@univr.it

[c] O. G. Willis, Dr. F. Zinna, Prof. L. Di Bari
Department of Chemistry and Industrial Chemistry
Pisa University
via Moruzzi 13, 56124 Pisa (Italy)
E-mail: lorenzo.dibari@unipi.it

[d] S. C. Gaglio, Dr. M. Perduca
Biocrystallography Lab, Department of Biotechnology
Verona University
Strada Le Grazie 15, 37134, Verona (Italy)

[e] Prof. C. Zaccone
Department of Biotechnology
Verona University
Strada Le Grazie 15, 37134, Verona (Italy)

[f] Prof. A. Romeo
Department of Computer Science
Verona University
Strada Le Grazie 15, 37134, Verona (Italy)

Supporting information for this article is available on the WWW under <https://doi.org/10.1002/chem.202200574>

© 2022 The Authors. Chemistry - A European Journal published by Wiley-VCH GmbH. This is an open access article under the terms of the Creative Commons Attribution License, which permits use, distribution and reproduction in any medium, provided the original work is properly cited.

Conclusion

Among the biomaterials, Polylactic-co-glycolic acids (PLGA) could be considered the “golden standard” for precision medicine purpose: indeed, it is a material suitable to design nano and microstructures, such as particles and scaffolds, enhancing the properties of the cargo (hydrophobic molecules, nanoparticles, cells and so on) while overcoming several drawbacks, such as chemical instability and lower bioavailability. Furthermore, the polymeric composition can be easily modified to control drug release pattern and to add new functionalities such as active targeting.

Nevertheless, we wanted to add some insights on PLGA nanoparticles as delivery system that we found out during the last three years:

- I. PLGA nanoparticles are biocompatible as it was established by the U.S. Food and Drug Administration (FDA) and European Medicines Agency (EMA). However, such nanomaterials could cause some undesired effects due to unexpected “cell priming”. To overcome this issue, it could be recommended to insert in the design of the PLGA NPs loadings able to reduce or avoid “cell priming activation”. In the work of Gaglio *et al*³⁸, we highlighted that in the design of nanoparticles-based delivery systems the cargo should also be chosen properly in order to add features to the carrier. Therefore, consideration should be given not only to the benefits added to the loading but also to those that the loading could potentially bring to the carrier

- II. PLGA nanoparticles are suitable for plant extract-based delivery since they can increase bioavailability and chemical stability^{37,38}. We also demonstrated the ability to penetrate natural barrier by shielding the loading and letting it penetrate as intact. This feature could be useful to preserve the biological activity of label-molecules¹³⁰

- III. We demonstrated PLGA could be used to produce nanoplatforms, encapsulating BMNPs bounded to chemotherapy agents (Doxorubicin or antibacterial peptide AS-48)^{32,35}. These complex structures can provide dual treatment combining hyperthermia (either magnetic or photothermic) together with the preserved action of the molecule bound to BMNPs. We also demonstrated the non-toxicity of this nanoplatforms against macrophages, paving the way for its potential use as intracellular drug-carrier
- IV. We showed how to produce a NIR-CPL optical probes based on Yb(III) complex and PLGA. In this regard, the shielding from the environment is crucial to avoid quenching phenomenon. Thus, we used PLGA nanoparticles to preserve lanthanide complex emission from water molecules by avoiding the so-called Multiphoton Relaxation phenomenon

References

1. Garcia-Henao, C. E. *et al.* Bioactive food coating: A review. *Packag Technol Sci* **36**, 3–13 (2023).
2. Rezaei, A., Fathi, M. & Jafari, S. M. Nanoencapsulation of hydrophobic and low-soluble food bioactive compounds within different nanocarriers. *Food Hydrocolloids* **88**, 146–162 (2019).
3. Tayemeh, M. B., Kalbassi, M. R., Paknejad, H. & Joo, H. S. Dietary nano-encapsulated quercetin homeostated transcription of redox-status orchestrating genes in zebrafish (*Danio rerio*) exposed to silver nanoparticles. *Environmental Research* **185**, 109477 (2020).
4. Savjani, K. T., Gajjar, A. K. & Savjani, J. K. Drug Solubility: Importance and Enhancement Techniques. *ISRN Pharmaceutics* **2012**, 1–10 (2012).
5. Nayak, A. K. & Panigrahi, P. P. Solubility Enhancement of Etoricoxib by Cosolvency Approach. *ISRN Physical Chemistry* **2012**, 1–5 (2012).
6. Göke, K. *et al.* Novel strategies for the formulation and processing of poorly water-soluble drugs. *European Journal of Pharmaceutics and Biopharmaceutics* **126**, 40–56 (2018).
7. Zhang, X., Xing, H., Zhao, Y. & Ma, Z. Pharmaceutical Dispersion Techniques for Dissolution and Bioavailability Enhancement of Poorly Water-Soluble Drugs. *Pharmaceutics* **10**, 74 (2018).
8. Liu, D. *et al.* Elderberry (*Sambucus nigra* L.): Bioactive Compounds, Health Functions, and Applications. *J. Agric. Food Chem.* **70**, 4202–4220 (2022).
9. Cho, U. & Chen, J. K. Lanthanide-Based Optical Probes of Biological Systems. *Cell Chemical Biology* **27**, 921–936 (2020).
10. Heffern, M. C., Matosziuk, L. M. & Meade, T. J. Lanthanide Probes for Bioresponsive Imaging. *Chem. Rev.* **114**, 4496–4539 (2014).
11. Brandner, A. *et al.* Luminescence Properties and Quenching Mechanisms of $\text{Ln}(\text{Tf}_2\text{N})_3$ Complexes in the Ionic Liquid bmpyr Tf_2N . *Inorg. Chem.* **50**, 6509–6520 (2011).
12. *Comprehensive Inorganic Chemistry II.* (Elsevier, 2013). doi:10.1016/C2009-0-63454-1.
13. Shishir, M. R. I., Xie, L., Sun, C., Zheng, X. & Chen, W. Advances in micro and nano-encapsulation of bioactive compounds using biopolymer and lipid-based transporters. *Trends in Food Science & Technology* **78**, 34–60 (2018).
14. Ariyaratna, I. R. & Karunaratne, D. N. Microencapsulation stabilizes curcumin for efficient delivery in food applications. *Food Packaging and Shelf Life* **10**, 79–86 (2016).
15. Rodríguez, J., Martín, M. J., Ruiz, M. A. & Clares, B. Current encapsulation strategies for bioactive oils: From alimentary to pharmaceutical perspectives. *Food Research International* **83**, 41–59 (2016).
16. Joye, I. J. & McClements, D. J. Biopolymer-based nanoparticles and microparticles: Fabrication, characterization, and application. *Current Opinion in Colloid & Interface Science* **19**, 417–427 (2014).
17. de Souza Simões, L. *et al.* Micro- and nano bio-based delivery systems for food applications: In vitro behavior. *Advances in Colloid and Interface Science* **243**,

23–45 (2017).

18. Martins, V. F. R., Pintado, M. E., Morais, R. M. S. C. & Morais, A. M. M. B. Valorisation of Micro/Nanoencapsulated Bioactive Compounds from Plant Sources for Food Applications Towards Sustainability. *Foods* **12**, 32 (2022).
19. Rossi, Y. E., Vanden Braber, N. L., Díaz Vergara, L. I. & Montenegro, M. A. Bioactive Ingredients Obtained from Agro-industrial Byproducts: Recent Advances and Innovation in Micro- and Nanoencapsulation. *J. Agric. Food Chem.* **69**, 15066–15075 (2021).
20. Ortega-Oller, I. *et al.* Bone Regeneration from PLGA Micro-Nanoparticles. *BioMed Research International* **2015**, 1–18 (2015).
21. Sherstneva, A. A. *et al.* Biodegradable Microparticles for Regenerative Medicine: A State of the Art and Trends to Clinical Application. *Polymers* **14**, 1314 (2022).
22. Ross, K. A. *et al.* Nano-enabled delivery of diverse payloads across complex biological barriers. *Journal of Controlled Release* **219**, 548–559 (2015).
23. Hoshyar, N., Gray, S., Han, H. & Bao, G. The effect of nanoparticle size on *in vivo* pharmacokinetics and cellular interaction. *Nanomedicine* **11**, 673–692 (2016).
24. Hirano, S. *et al.* Ketamine nano-delivery based on poly-lactic-co-glycolic acid (PLGA) nanoparticles. *Appl Nanosci* **8**, 655–663 (2018).
25. Portioli, C. *et al.* Novel functionalization strategies of polymeric nanoparticles as carriers for brain medications: PEPTIDIC MOIETIES ENABLE BBB TRAVERSAL OF THE NPs. *J. Biomed. Mater. Res.* **105**, 847–858 (2017).
26. Wu, S.-H., Hung, Y. & Mou, C.-Y. Mesoporous silica nanoparticles as nanocarriers. *Chem. Commun.* **47**, 9972 (2011).
27. Din, F. *et al.* Effective use of nanocarriers as drug delivery systems for the treatment of selected tumors. *IJN Volume* **12**, 7291–7309 (2017).
28. Mago, A., Junaid Tahir, M., Arslan Khan, M., Abbasher Hussien Mohamed Ahmed, K. & Usman Munir, M. Nanomedicine: Advancement in healthcare. *Annals of Medicine and Surgery* **79**, 104078 (2022).
29. Saha. Nanomedicine: Promising Tiny Machine for the Healthcare in Future-A Review. *OMJ* (2009) doi:10.5001/omj.2009.50.
30. Navya, P. N. & Daima, H. K. Rational engineering of physicochemical properties of nanomaterials for biomedical applications with nanotoxicological perspectives. *Nano Convergence* **3**, 1 (2016).
31. Odiba, A., Ukegbu, C., Anunobi, O., Chukwunonyelum, I. & Esemonu, J. Making drugs safer: improving drug delivery and reducing the side effect of drugs on the human biochemical system. *Nanotechnology Reviews* **5**, (2016).
32. Gaglio, S. C. *et al.* Embedding Biomimetic Magnetic Nanoparticles Coupled with Peptide AS-48 into PLGA to Treat Intracellular Pathogens. *Pharmaceutics* **14**, 2744 (2022).
33. Seung, K. J., Keshavjee, S. & Rich, M. L. Multidrug-Resistant Tuberculosis and Extensively Drug-Resistant Tuberculosis. *Cold Spring Harb Perspect Med* **5**, a017863 (2015).
34. Jabalera, Y. *et al.* Antibacterial directed chemotherapy using AS-48 peptide immobilized on biomimetic magnetic nanoparticles combined with magnetic

- hyperthermia. *International Journal of Biological Macromolecules* **189**, 206–213 (2021).
35. Jabalera, Y. *et al.* Enhanced Cytotoxic Effect of TAT–PLGA-Embedded DOXO Carried by Biomimetic Magnetic Nanoparticles upon Combination with Magnetic Hyperthermia and Photothermia. *Pharmaceutics* **13**, 1168 (2021).
36. Witika, B. A. *et al.* Biocompatibility of Biomaterials for Nanoencapsulation: Current Approaches. *Nanomaterials* **10**, 1649 (2020).
37. Donini, M., Gaglio, S. C., Laudanna, C., Perduca, M. & Dusi, S. Ox-yresveratrol-Loaded PLGA Nanoparticles Inhibit Oxygen Free Radical Production by Human Monocytes: Role in Nanoparticle Biocompatibility. *Molecules* **26**, 4351 (2021).
38. Gaglio, S. C., Donini, M., Denbaes, P. E., Dusi, S. & Perduca, M. Ox-yresveratrol Inhibits R848-Induced Pro-Inflammatory Mediators Release by Human Dendritic Cells Even When Embedded in PLGA Nanoparticles. *Molecules* **26**, 2106 (2021).
39. Li, Y. *et al.* Hollow Mesoporous Silica Nanoparticles with Tunable Structures for Controlled Drug Delivery. *ACS Appl. Mater. Interfaces* **9**, 2123–2129 (2017).
40. Yang, W., Liang, H., Ma, S., Wang, D. & Huang, J. Gold nanoparticle based photothermal therapy: Development and application for effective cancer treatment. *Sustainable Materials and Technologies* **22**, e00109 (2019).
41. Bobo, D., Robinson, K. J., Islam, J., Thurecht, K. J. & Corrie, S. R. Nanoparticle-Based Medicines: A Review of FDA-Approved Materials and Clinical Trials to Date. *Pharm Res* **33**, 2373–2387 (2016).
42. Mitchell, M. J. *et al.* Engineering precision nanoparticles for drug delivery. *Nat Rev Drug Discov* **20**, 101–124 (2021).
43. Lopez-Chaves, C. *et al.* Gold nanoparticles: Distribution, bioaccumulation and toxicity. In vitro and in vivo studies. *Nanomedicine: Nanotechnology, Biology and Medicine* **14**, 1–12 (2018).
44. Anselmo, A. C. & Mitragotri, S. Nanoparticles in the clinic: An update. *Bi-oeng Transl Med* **4**, (2019).
45. Fenton, O. S., Olafson, K. N., Pillai, P. S., Mitchell, M. J. & Langer, R. Advances in Biomaterials for Drug Delivery. *Adv. Mater.* **30**, 1705328 (2018).
46. Liu, P., Chen, G. & Zhang, J. A Review of Liposomes as a Drug Delivery System: Current Status of Approved Products, Regulatory Environments, and Future Perspectives. *Molecules* **27**, 1372 (2022).
47. Fonseca-Santos, B., Chorilli, M. & Palmira Daflon Gremião, M. Nanotechnology-based drug delivery systems for the treatment of Alzheimer's disease. *IJN* 4981 (2015) doi:10.2147/IJN.S87148.
48. Khalin, I., Alyautdin, R., Ismail, N. M., Haron, M. H. & Kuznetsov, D. Nanoscale drug delivery systems and the blood–brain barrier. *IJN* 795 (2014) doi:10.2147/IJN.S52236.
49. Leung, A. K. K., Tam, Y. Y. C., Chen, S., Hafez, I. M. & Cullis, P. R. Microfluidic Mixing: A General Method for Encapsulating Macromolecules in Lipid Nanoparticle Systems. *J. Phys. Chem. B* **119**, 8698–8706 (2015).
50. Asem, H. & Malmström, E. Polymeric Nanoparticles Explored for Drug-

- Delivery Applications. in *ACS Symposium Series* (eds. Horkay, F., Douglas, J. F. & Del Gado, E.) vol. 1296 315–331 (American Chemical Society, 2018).
51. Kahraman, E., Güngör, S. & Özsoy, Y. Potential enhancement and targeting strategies of polymeric and lipid-based nanocarriers in dermal drug delivery. *Therapeutic Delivery* **8**, 967–985 (2017).
 52. Zielińska, A. *et al.* Polymeric Nanoparticles: Production, Characterization, Toxicology and Ecotoxicology. *Molecules* **25**, 3731 (2020).
 53. Matthew, S. A. L., Rezwani, R., Perrie, Y. & Seib, F. P. Volumetric Scalability of Microfluidic and Semi-Batch Silk Nanoprecipitation Methods. *Molecules* **27**, 2368 (2022).
 54. Afsharzadeh, M., Hashemi, M., Mokhtarzadeh, A., Abnous, K. & Ramezani, M. Recent advances in co-delivery systems based on polymeric nanoparticle for cancer treatment. *Artificial Cells, Nanomedicine, and Biotechnology* **46**, 1095–1110 (2018).
 55. Danhier, F. *et al.* PLGA-based nanoparticles: An overview of biomedical applications. *Journal of Controlled Release* **161**, 505–522 (2012).
 56. Alsaab, H. O. *et al.* PLGA-Based Nanomedicine: History of Advancement and Development in Clinical Applications of Multiple Diseases. *Pharmaceutics* **14**, 2728 (2022).
 57. Anderson, J. M. & Shive, M. S. Biodegradation and biocompatibility of PLA and PLGA microspheres. *Advanced Drug Delivery Reviews* **28**, 5–24 (1997).
 58. Hines, D. J. & Kaplan, D. L. Poly(lactic-co-glycolic) Acid-Controlled-Release Systems: Experimental and Modeling Insights. *Crit Rev Ther Drug Carrier Syst* **30**, 257–276 (2013).
 59. Lü, J.-M. *et al.* Current advances in research and clinical applications of PLGA-based nanotechnology. *Expert Review of Molecular Diagnostics* **9**, 325–341 (2009).
 60. Hans, M. L. & Lowman, A. M. Biodegradable nanoparticles for drug delivery and targeting. *Current Opinion in Solid State and Materials Science* **6**, 319–327 (2002).
 61. Kocbek, P., Obermajer, N., Cegnar, M., Kos, J. & Kristl, J. Targeting cancer cells using PLGA nanoparticles surface modified with monoclonal antibody. *Journal of Controlled Release* **120**, 18–26 (2007).
 62. Luque-Michel, E., Sebastian, V., Larrea, A., Marquina, C. & Blanco-Prieto, M. J. Co-encapsulation of superparamagnetic nanoparticles and doxorubicin in PLGA nanocarriers: Development, characterization and in vitro antitumor efficacy in glioma cells. *European Journal of Pharmaceutics and Biopharmaceutics* **145**, 65–75 (2019).
 63. Quintanar-Guerrero, D., Allémann, E., Fessi, H. & Doelker, E. Preparation Techniques and Mechanisms of Formation of Biodegradable Nanoparticles from Preformed Polymers. *Drug Development and Industrial Pharmacy* **24**, 1113–1128 (1998).
 64. McCall, R. L. & Sirianni, R. W. PLGA Nanoparticles Formed by Single- or Double-emulsion with Vitamin E-TPGS. *JoVE* 51015 (2013) doi:10.3791/51015.
 65. Kulkarni, S. A. & Feng, S.-S. Effects of Particle Size and Surface Modification on Cellular Uptake and Biodistribution of Polymeric Nanoparticles for Drug

- Delivery. *Pharm Res* **30**, 2512–2522 (2013).
66. Choi, H. S. *et al.* Tissue- and Organ-Selective Biodistribution of NIR Fluorescent Quantum Dots. *Nano Lett.* **9**, 2354–2359 (2009).
67. Reisch, A., Runser, A., Arntz, Y., Mély, Y. & Klymchenko, A. S. Charge-Controlled Nanoprecipitation as a Modular Approach to Ultrasmall Polymer Nanocarriers: Making Bright and Stable Nanoparticles. *ACS Nano* **9**, 5104–5116 (2015).
68. Cavalli, E. *et al.* Near Infrared Circularly Polarized Luminescence From Water Stable Organic Nanoparticles Containing a Chiral Yb(III) Complex. *Chemistry A European J* **28**, (2022).
69. Iván Martínez-Muñoz, O., Fernando Ospina-Giraldo, L. & Elizabeth Mora-Huertas, C. Nanoprecipitation: Applications for Entrapping Active Molecules of Interest in Pharmaceuticals. in *Nano- and Microencapsulation - Techniques and Applications* (ed. Abu-Thabit, N.) (IntechOpen, 2021). doi:10.5772/intechopen.93338.
70. Staff, R. H., Landfester, K. & Crespy, D. Recent Advances in the Emulsion Solvent Evaporation Technique for the Preparation of Nanoparticles and Nanocapsules. in *Hierarchical Macromolecular Structures: 60 Years after the Staudinger Nobel Prize II* (ed. Percec, V.) vol. 262 329–344 (Springer International Publishing, 2013).
71. Yus, C., Arruebo, M., Irusta, S. & Sebastián, V. Microflow Nanoprecipitation of Positively Charged Gastroresistant Polymer Nanoparticles of Eudragit® RS100: A Study of Fluid Dynamics and Chemical Parameters. *Materials* **13**, 2925 (2020).
72. Fadeel, B. Hide and Seek: Nanomaterial Interactions With the Immune System. *Front. Immunol.* **10**, 133 (2019).
73. Hilligan, K. L. & Ronchese, F. Antigen presentation by dendritic cells and their instruction of CD4+ T helper cell responses. *Cell Mol Immunol* **17**, 587–599 (2020).
74. Wang, Y. *et al.* Dendritic cell biology and its role in tumor immunotherapy. *J Hematol Oncol* **13**, 107 (2020).
75. Anderson, D. A., Dutertre, C.-A., Ginhoux, F. & Murphy, K. M. Genetic models of human and mouse dendritic cell development and function. *Nat Rev Immunol* **21**, 101–115 (2021).
76. Floss, D. M., Moll, J. M. & Scheller, J. IL-12 and IL-23—Close Relatives with Structural Homologies but Distinct Immunological Functions. *Cells* **9**, 2184 (2020).
77. Vignali, D. A. A. & Kuchroo, V. K. IL-12 family cytokines: immunological playmakers. *Nat Immunol* **13**, 722–728 (2012).
78. Zelová, H. & Hošek, J. TNF- α signalling and inflammation: interactions between old acquaintances. *Inflamm. Res.* **62**, 641–651 (2013).
79. Kaur, S., Bansal, Y., Kumar, R. & Bansal, G. A panoramic review of IL-6: Structure, pathophysiological roles and inhibitors. *Bioorganic & Medicinal Chemistry* **28**, 115327 (2020).
80. Švajger, U., Obermajer, N. & Jeras, M. Dendritic cells treated with resveratrol during differentiation from monocytes gain substantial tolerogenic properties upon activation: Resveratrol-induced dendritic cell tolerogenicity. *Immunology* **129**,

525–535 (2010).

81. Panichakul, T. *et al.* Additive Effect of a Combination of *Artocarpus lakoocha* and *Glycyrrhiza glabra* Extracts on Tyrosinase Inhibition in Melanoma B16 Cells. *Pharmaceuticals* **13**, 310 (2020).
82. Ashraf, M. I., Shahzad, M. & Shabbir, A. Oxyresveratrol ameliorates allergic airway inflammation via attenuation of IL-4, IL-5, and IL-13 expression levels. *Cytokine* **76**, 375–381 (2015).
83. Hankittichai, P. *et al.* Oxyresveratrol Inhibits IL-1 β -Induced Inflammation via Suppressing AKT and ERK1/2 Activation in Human Microglia, HMC3. *IJMS* **21**, 6054 (2020).
84. Wei, J. *et al.* Oxyresveratrol Is a Phytoestrogen Exerting Anti-inflammatory Effects Through NF- κ B and Estrogen Receptor Signaling. *Inflammation* **40**, 1285–1296 (2017).
85. Aziz, R. S., Siddiqua, A., Shahzad, M., Shabbir, A. & Naseem, N. Oxyresveratrol ameliorates ethanol-induced gastric ulcer via downregulation of IL-6, TNF- α , NF- κ B, and COX-2 levels, and upregulation of TFF-2 levels. *Biomedicine & Pharmacotherapy* **110**, 554–560 (2019).
86. Gaglio, S. C., De Rosa, C., Piccinelli, F., Romeo, A. & Perduca, M. Complexes of rare earth ions embedded in poly(lactic-co-glycolic acid) (PLGA) nanoparticles: Characterization and spectroscopic study. *Optical Materials* **94**, 249–256 (2019).
87. Jurk, M. *et al.* Human TLR7 or TLR8 independently confer responsiveness to the antiviral compound R-848. *Nat Immunol* **3**, 499–499 (2002).
88. Frega, G. *et al.* Trial Watch: experimental TLR7/TLR8 agonists for oncological indications. *OncImmunology* **9**, 1796002 (2020).
89. Marongiu, L. *et al.* The inclusion into PLGA nanoparticles enables α -bisabolol to efficiently inhibit the human dendritic cell pro-inflammatory activity. *J Nanopart Res* **16**, 2554 (2014).
90. Harirforoosh, S., Asghar, W. & Jamali, F. Adverse Effects of Nonsteroidal Antiinflammatory Drugs: An Update of Gastrointestinal, Cardiovascular and Renal Complications. *J Pharm Pharm Sci* **16**, 821 (2014).
91. Whitehouse, M. W. Anti-inflammatory glucocorticoid drugs: reflections after 60 years. *Inflammopharmacol* **19**, 1–19 (2011).
92. Radapong, S., Sarker, S. D. & Ritchie, K. J. Oxyresveratrol Possesses DNA Damaging Activity. *Molecules* **25**, 2577 (2020).
93. Hankittichai, P. *et al.* *Artocarpus lakoocha* Extract Inhibits LPS-Induced Inflammatory Response in RAW 264.7 Macrophage Cells. *IJMS* **21**, 1355 (2020).
94. Jia, Y.-N. *et al.* Oxyresveratrol prevents lipopolysaccharide/d-galactosamine-induced acute liver injury in mice. *International Immunopharmacology* **56**, 105–112 (2018).
95. Fischer, R., Kontermann, R. E. & Pfizenmaier, K. Selective Targeting of TNF Receptors as a Novel Therapeutic Approach. *Front. Cell Dev. Biol.* **8**, 401 (2020).
96. Steeland, S., Libert, C. & Vandenbroucke, R. E. A New Venue of TNF Targeting. *IJMS* **19**, 1442 (2018).
97. Moschen, A. R., Tilg, H. & Raine, T. IL-12, IL-23 and IL-17 in IBD:

- immunobiology and therapeutic targeting. *Nat Rev Gastroenterol Hepatol* **16**, 185–196 (2019).
98. Chyuan, I.-T. & Lai, J.-H. New insights into the IL-12 and IL-23: From a molecular basis to clinical application in immune-mediated inflammation and cancers. *Biochemical Pharmacology* **175**, 113928 (2020).
99. Lorenz, P., Roychowdhury, S., Engelmann, M., Wolf, G. & Horn, T. F. W. Oxyresveratrol and resveratrol are potent antioxidants and free radical scavengers: effect on nitrosative and oxidative stress derived from microglial cells. *Nitric Oxide* **9**, 64–76 (2003).
100. Shah, A., Chao, J., Legido-Quigley, C. & Chang, R. C.-C. Oxyresveratrol exerts ATF4- and Grp78-mediated neuroprotection against endoplasmic reticulum stress in experimental Parkinson's disease. *Nutritional Neuroscience* **24**, 181–196 (2021).
101. Dobrovolskaia, M. A., Shurin, M. & Shvedova, A. A. Current understanding of interactions between nanoparticles and the immune system. *Toxicology and Applied Pharmacology* **299**, 78–89 (2016).
102. Najafi-Hajivar, S. *et al.* Overview on experimental models of interactions between nanoparticles and the immune system. *Biomedicine & Pharmacotherapy* **83**, 1365–1378 (2016).
103. Vogt, K. L., Summers, C., Chilvers, E. R. & Condliffe, A. M. Priming and de-priming of neutrophil responses in vitro and in vivo. *Eur J Clin Invest* **48**, e12967 (2018).
104. Locati, M., Curtale, G. & Mantovani, A. Diversity, Mechanisms, and Significance of Macrophage Plasticity. *Annu. Rev. Pathol. Mech. Dis.* **15**, 123–147 (2020).
105. Chistè, E. *et al.* TiO₂-coated luminescent porous silicon micro-particles as a promising system for nanomedicine. *J. Mater. Chem. B* **6**, 1815–1824 (2018).
106. Fang, S.-C., Hsu, C.-L. & Yen, G.-C. Anti-inflammatory Effects of Phenolic Compounds Isolated from the Fruits of *Artocarpus heterophyllus*. *J. Agric. Food Chem.* **56**, 4463–4468 (2008).
107. Abdul Rahim, R. *et al.* Recent Advances in Nanoencapsulation Systems Using PLGA of Bioactive Phenolics for Protection against Chronic Diseases. *IJERPH* **16**, 4962 (2019).
108. Brieger, K., Schiavone, S., Miller, Jr. & Krause, K. Reactive oxygen species: from health to disease. *Swiss Med Wkly* (2012) doi:10.4414/smw.2012.13659.
109. Ban, J. Y. *et al.* Neuroprotective Effect of Oxyresveratrol from *Smilacis Chinae* Rhizome on Amyloid .BETA. Protein (25-35)-Induced Neurotoxicity in Cultured Rat Cortical Neurons. *Biological & Pharmaceutical Bulletin* **29**, 2419–2424 (2006).
110. Andrabi, S. A. *et al.* Oxyresveratrol (trans-2,3',4,5'-tetrahydroxystilbene) is neuroprotective and inhibits the apoptotic cell death in transient cerebral ischemia. *Brain Research* **1017**, 98–107 (2004).
111. Du, H., Ma, L., Chen, G. & Li, S. The effects of oxyresveratrol abrogates inflammation and oxidative stress in rat model of spinal cord injury. *Mol Med Report* (2017) doi:10.3892/mmr.2017.8294.
112. Hu, X., Liang, Y., Zhao, B. & Wang, Y. Oxyresveratrol protects human lens

- epithelial cells against hydrogen peroxide-induced oxidative stress and apoptosis by activation of Akt/HO-1 pathway. *Journal of Pharmacological Sciences* **139**, 166–173 (2019).
113. Choi, H. Y. *et al.* Oxyresveratrol abrogates oxidative stress by activating ERK–Nrf2 pathway in the liver. *Chemico-Biological Interactions* **245**, 110–121 (2016).
114. Kim, K.-M. *et al.* *Smilax China* Root Extract Detoxifies Nicotine by Reducing Reactive Oxygen Species and Inducing CYP2A6: *Smilax china* root extract detoxifies nicotine.... *Journal of Food Science* **79**, H2132–H2139 (2014).
115. Chatsumpun, M., Chuanasa, T., Sritularak, B. & Likhitwitayawuid, K. Oxyresveratrol protects against DNA damage induced by photosensitized riboflavin. *Nat Prod Commun* **6**, 41–44 (2011).
116. Lee, H., Kim, D., Hong, J., Lee, J.-Y. & Kim, E. Oxyresveratrol suppresses lipopolysaccharide-induced inflammatory responses in murine macrophages. *Hum Exp Toxicol* **34**, 808–818 (2015).
117. Xu, B., Watkins, R., Wu, L., Zhang, C. & Davis, R. Natural product-based nanomedicine: recent advances and issues. *IJN* 6055 (2015) doi:10.2147/IJN.S92162.
118. Hesari, M. *et al.* Current Advances in the Use of Nanophytomedicine Therapies for Human Cardiovascular Diseases. *IJN Volume* **16**, 3293–3315 (2021).
119. Zang, X., Cheng, M., Zhang, X. & Chen, X. Quercetin nanoformulations: a promising strategy for tumor therapy. *Food Funct.* **12**, 6664–6681 (2021).
120. Xie, X. *et al.* PLGA Nanoparticles Improve the Oral Bioavailability of Curcumin in Rats: Characterizations and Mechanisms. *J. Agric. Food Chem.* **59**, 9280–9289 (2011).
121. Nauseef, W. M. The phagocyte NOX2 NADPH oxidase in microbial killing and cell signaling. *Current Opinion in Immunology* **60**, 130–140 (2019).
122. De Marco Castro, E., Calder, P. C. & Roche, H. M. β -1,3/1,6-Glucans and Immunity: State of the Art and Future Directions. *Mol. Nutr. Food Res.* **65**, 1901071 (2021).
123. Goodridge, H. S., Wolf, A. J. & Underhill, D. M. β -glucan recognition by the innate immune system. *Immunological Reviews* **230**, 38–50 (2009).
124. Dupré-Crochet, S., Erard, M. & Nüße, O. ROS production in phagocytes: why, when, and where? *Journal of Leukocyte Biology* **94**, 657–670 (2013).
125. Aillon, K. L., Xie, Y., El-Gendy, N., Berkland, C. J. & Forrest, M. L. Effects of nanomaterial physicochemical properties on in vivo toxicity. *Advanced Drug Delivery Reviews* **61**, 457–466 (2009).
126. Anozie, U. C. & Dalhaimer, P. Molecular links among non-biodegradable nanoparticles, reactive oxygen species, and autophagy. *Advanced Drug Delivery Reviews* **122**, 65–73 (2017).
127. Mortezaee, K. *et al.* Redox interactions and genotoxicity of metal-based nanoparticles: A comprehensive review. *Chemico-Biological Interactions* **312**, 108814 (2019).
128. Tulinska, J. *et al.* Immunotoxicity and genotoxicity testing of PLGA-PEO nanoparticles in human blood cell model. *Nanotoxicology* **9**, 33–43 (2015).
129. Yousefian, M. *et al.* The natural phenolic compounds as modulators of

- NADPH oxidases in hypertension. *Phytomedicine* **55**, 200–213 (2019).
130. Dalle Carbonare, L. *et al.* Fisetin: An Integrated Approach to Identify a Strategy Promoting Osteogenesis. *Front Pharmacol* **13**, 890693 (2022).
131. Khan, N., Afaq, F., Syed, D. N. & Mukhtar, H. Fisetin, a novel dietary flavonoid, causes apoptosis and cell cycle arrest in human prostate cancer LNCaP cells. *Carcinogenesis* **29**, 1049–1056 (2008).
132. Zheng, W. *et al.* Fisetin inhibits IL-1 β -induced inflammatory response in human osteoarthritis chondrocytes through activating SIRT1 and attenuates the progression of osteoarthritis in mice. *International Immunopharmacology* **45**, 135–147 (2017).
133. Léotoing, L. *et al.* The Polyphenol Fisetin Protects Bone by Repressing NF- κ B and MKP-1-Dependent Signaling Pathways in Osteoclasts. *PLoS ONE* **8**, e68388 (2013).
134. Cederroth, C. R. & Nef, S. Soy, phytoestrogens and metabolism: A review. *Molecular and Cellular Endocrinology* **304**, 30–42 (2009).
135. Trzeciakiewicz, A., Habauzit, V. & Horcajada, M.-N. When nutrition interacts with osteoblast function: molecular mechanisms of polyphenols. *Nutr. Res. Rev.* **22**, 68–81 (2009).
136. Kular, J., Tickner, J., Chim, S. M. & Xu, J. An overview of the regulation of bone remodelling at the cellular level. *Clinical Biochemistry* **45**, 863–873 (2012).
137. Soltanoff, C. S., Yang, S., Chen, W. & Li, Y.-P. Signaling Networks that Control the Lineage Commitment and Differentiation of Bone Cells. *Crit Rev Eukar Gene Expr* **19**, 1–46 (2009).
138. Marie, P. J. Transcription factors controlling osteoblastogenesis. *Archives of Biochemistry and Biophysics* **473**, 98–105 (2008).
139. Komori, T. Regulation of bone development and extracellular matrix protein genes by RUNX2. *Cell Tissue Res* **339**, 189–195 (2010).
140. Lee, B. *et al.* Missense mutations abolishing DNA binding of the osteoblast-specific transcription factor OSF2/CBFA1 in cleidocranial dysplasia. *Nat Genet* **16**, 307–310 (1997).
141. Kaback, L. A. *et al.* Osterix/Sp7 regulates mesenchymal stem cell mediated endochondral ossification. *J Cell Physiol* **214**, 173–182 (2008).
142. Sechi, M. *et al.* Nanoencapsulation of dietary flavonoid fisetin: Formulation and in vitro antioxidant and α -glucosidase inhibition activities. *Materials Science and Engineering: C* **68**, 594–602 (2016).
143. Kadari, A. *et al.* Enhanced oral bioavailability and anticancer efficacy of fisetin by encapsulating as inclusion complex with HP β CD in polymeric nanoparticles. *Drug Delivery* **24**, 224–232 (2017).
144. Dalle Carbonare, L. *et al.* Increased Gene Expression of RUNX2 and SOX9 in Mesenchymal Circulating Progenitors Is Associated with Autophagy during Physical Activity. *Oxidative Medicine and Cellular Longevity* **2019**, 1–14 (2019).
145. Liu, W.-Y., Lin, C.-C., Hsieh, Y.-S. & Wu, Y.-T. Nanoformulation Development to Improve the Biopharmaceutical Properties of Fisetin Using Design of Experiment Approach. *Molecules* **26**, 3031 (2021).
146. Rajamäki, K. *et al.* Extracellular Acidosis Is a Novel Danger Signal Alerting Innate Immunity via the NLRP3 Inflammasome. *Journal of Biological Chemistry*

- 288, 13410–13419 (2013).
147. de Nadai, T. R. *et al.* Metabolic Acidosis Treatment as Part of a Strategy to Curb Inflammation. *International Journal of Inflammation* **2013**, 1–4 (2013).
148. Casimir, G. J., Lefèvre, N., Corazza, F., Duchateau, J. & Chamekh, M. The Acid–Base Balance and Gender in Inflammation: A Mini-Review. *Front. Immunol.* **9**, 475 (2018).
149. Joshi, G., Kumar, A. & Sawant, K. Enhanced bioavailability and intestinal uptake of Gemcitabine HCl loaded PLGA nanoparticles after oral delivery. *European Journal of Pharmaceutical Sciences* **60**, 80–89 (2014).
150. Palocci, C. *et al.* Endocytic pathways involved in PLGA nanoparticle uptake by grapevine cells and role of cell wall and membrane in size selection. *Plant Cell Rep* **36**, 1917–1928 (2017).
151. Llor, C. & Bjerrum, L. Antimicrobial resistance: risk associated with antibiotic overuse and initiatives to reduce the problem. *Therapeutic Advances in Drug Safety* **5**, 229–241 (2014).
152. Griffiths, G., Nyström, B., Sable, S. B. & Khuller, G. K. Nanobead-based interventions for the treatment and prevention of tuberculosis. *Nat Rev Microbiol* **8**, 827–834 (2010).
153. Wu *et al.* Metal–Organic Framework-Based Chemo-Photothermal Combinational System for Precise, Rapid, and Efficient Antibacterial Therapeutics. *Pharmaceutics* **11**, 463 (2019).
154. Wang, H. *et al.* A dual-targeted platform based on graphene for synergistic chemo-photothermal therapy against multidrug-resistant Gram-negative bacteria and their biofilms. *Chemical Engineering Journal* **393**, 124595 (2020).
155. Oltolina, F. *et al.* Biomimetic Magnetite Nanoparticles as Targeted Drug Nanocarriers and Mediators of Hyperthermia in an Experimental Cancer Model. *Cancers* **12**, 2564 (2020).
156. Prestinaci, F., Pezzotti, P. & Pantosti, A. Antimicrobial resistance: a global multifaceted phenomenon. *Pathogens and Global Health* **109**, 309–318 (2015).
157. García Rubia, G. *et al.* pH-Dependent Adsorption Release of Doxorubicin on MamC-Biomimetic Magnetite Nanoparticles. *Langmuir* **34**, 13713–13724 (2018).
158. Jabalera, Y. *et al.* Nanoformulation Design Including MamC-Mediated Biomimetic Nanoparticles Allows the Simultaneous Application of Targeted Drug Delivery and Magnetic Hyperthermia. *Polymers* **12**, 1832 (2020).
159. Peigneux, A. *et al.* Functionalized Biomimetic Magnetic Nanoparticles as Effective Nanocarriers for Targeted Chemotherapy. *Part. Part. Syst. Charact.* **36**, 1900057 (2019).
160. Kok, H. P. & Crezee, J. A comparison of the heating characteristics of capacitive and radiative superficial hyperthermia. *International Journal of Hyperthermia* **33**, 378–386 (2017).
161. Toraya-Brown, S. & Fiering, S. Local tumour hyperthermia as immunotherapy for metastatic cancer. *International Journal of Hyperthermia* **30**, 531–539 (2014).
162. Golombek, S. K. *et al.* Tumor targeting via EPR: Strategies to enhance patient responses. *Advanced Drug Delivery Reviews* **130**, 17–38 (2018).




163. Jabalera, Y. *et al.* Oxaliplatin–Biomimetic Magnetic Nanoparticle Assemblies for Colon Cancer-Targeted Chemotherapy: An In Vitro Study. *Pharmaceutics* **11**, 395 (2019).
164. Montalbán-López, M. *et al.* Synergy of the Bacteriocin AS-48 and Antibiotics against Uropathogenic Enterococci. *Antibiotics* **9**, 567 (2020).
165. Ananou, S. *et al.* Effect of combined physico-chemical treatments based on enterocin AS-48 on the control of *Listeria monocytogenes* and *Staphylococcus aureus* in a model cooked ham. *Food Control* **21**, 478–486 (2010).
166. Martínez-García, M. *et al.* Autophagic-related cell death of *Trypanosoma brucei* induced by bacteriocin AS-48. *International Journal for Parasitology: Drugs and Drug Resistance* **8**, 203–212 (2018).
167. Abengózar, M. Á. *et al.* Enterocin AS-48 as Evidence for the Use of Bacteriocins as New Leishmanicidal Agents. *Antimicrob Agents Chemother* **61**, e02288-16 (2017).
168. Cebrián, R. *et al.* The bacteriocin AS-48 requires dimer dissociation followed by hydrophobic interactions with the membrane for antibacterial activity. *Journal of Structural Biology* **190**, 162–172 (2015).
169. Cebrián, R. *et al.* Preclinical studies of toxicity and safety of the AS-48 bacteriocin. *Journal of Advanced Research* **20**, 129–139 (2019).
170. Vurro, F. *et al.* Improving the Cellular Uptake of Biomimetic Magnetic Nanoparticles. *Nanomaterials* **11**, 766 (2021).
171. Kumari, A., Yadav, S. K. & Yadav, S. C. Biodegradable polymeric nanoparticles based drug delivery systems. *Colloids and Surfaces B: Biointerfaces* **75**, 1–18 (2010).
172. Makadia, H. K. & Siegel, S. J. Poly Lactic-co-Glycolic Acid (PLGA) as Biodegradable Controlled Drug Delivery Carrier. *Polymers* **3**, 1377–1397 (2011).
173. Gálvez, A., Maqueda, M., Martínez-Bueno, M. & Valdivia, E. Permeation of bacterial cells, permeation of cytoplasmic and artificial membrane vesicles, and channel formation on lipid bilayers by peptide antibiotic AS-48. *J Bacteriol* **173**, 886–892 (1991).
174. Valverde-Tercedor, C. *et al.* Size control of in vitro synthesized magnetite crystals by the MamC protein of *Magnetococcus marinus* strain MC-1. *Appl Microbiol Biotechnol* **99**, 5109–5121 (2015).
175. Nečas, D. & Klapetek, P. Gwyddion: an open-source software for SPM data analysis. *Open Physics* **10**, (2012).
176. Gross, J., Sayle, S., Karow, A. R., Bakowsky, U. & Garidel, P. Nanoparticle tracking analysis of particle size and concentration detection in suspensions of polymer and protein samples: Influence of experimental and data evaluation parameters. *European Journal of Pharmaceutics and Biopharmaceutics* **104**, 30–41 (2016).
177. Gross, J., Sayle, S., Karow, A. R., Bakowsky, U. & Garidel, P. Nanoparticle tracking analysis of particle size and concentration detection in suspensions of polymer and protein samples: Influence of experimental and data evaluation parameters. *European Journal of Pharmaceutics and Biopharmaceutics* **104**, 30–41 (2016).
178. Hergt, R. & Dutz, S. Magnetic particle hyperthermia—biophysical limitations of a visionary tumour therapy. *Journal of Magnetism and Magnetic Materials* **311**, 187–192 (2007).

179. Obaidat, I., Issa, B. & Haik, Y. Magnetic Properties of Magnetic Nanoparticles for Efficient Hyperthermia. *Nanomaterials* **5**, 63–89 (2015).
180. Wildeboer, R. R., Southern, P. & Pankhurst, Q. A. On the reliable measurement of specific absorption rates and intrinsic loss parameters in magnetic hyperthermia materials. *J. Phys. D: Appl. Phys.* **47**, 495003 (2014).
181. Zolnik, B. S. & Burgess, D. J. Effect of acidic pH on PLGA microsphere degradation and release. *Journal of Controlled Release* **122**, 338–344 (2007).
182. Aguilar-Pérez, C. *et al.* Synergy between Circular Bacteriocin AS-48 and Ethambutol against Mycobacterium tuberculosis. *Antimicrob Agents Chemother* **62**, e00359-18 (2018).
183. Wu, J. The Enhanced Permeability and Retention (EPR) Effect: The Significance of the Concept and Methods to Enhance Its Application. *J Pers Med* **11**, 771 (2021).
184. El-Boubbou, K. Magnetic iron oxide nanoparticles as drug carriers: preparation, conjugation and delivery. *Nanomedicine* **13**, 929–952 (2018).
185. Dobson, J. Magnetic micro- and nano-particle-based targeting for drug and gene delivery. *Nanomedicine* **1**, 31–37 (2006).
186. Kaczmarek, K., Mrówczyński, R., Hornowski, T., Bielas, R. & Józefczak, A. The Effect of Tissue-Mimicking Phantom Compressibility on Magnetic Hyperthermia. *Nanomaterials* **9**, 803 (2019).
187. Nemeč, S. *et al.* Comparison of Iron Oxide Nanoparticles in Photothermia and Magnetic Hyperthermia: Effects of Clustering and Silica Encapsulation on Nanoparticles' Heating Yield. *Applied Sciences* **10**, 7322 (2020).
188. Singh, R. K., Kim, T.-H., Patel, K. D., Knowles, J. C. & Kim, H.-W. Biocompatible magnetite nanoparticles with varying silica-coating layer for use in biomedicine: Physicochemical and magnetic properties, and cellular compatibility. *J. Biomed. Mater. Res.* **100A**, 1734–1742 (2012).
189. Xuan, Y. & Li, Q. Heat transfer enhancement of nanofluids. *International Journal of Heat and Fluid Flow* **21**, 58–64 (2000).
190. Cartiera, M. S., Johnson, K. M., Rajendran, V., Caplan, M. J. & Saltzman, W. M. The uptake and intracellular fate of PLGA nanoparticles in epithelial cells. *Biomaterials* **30**, 2790–2798 (2009).
191. Zeng, J., Martin, A., Han, X., Shirihai, O. S. & Grinstaff, M. W. Biodegradable PLGA Nanoparticles Restore Lysosomal Acidity and Protect Neural PC-12 Cells against Mitochondrial Toxicity. *Ind. Eng. Chem. Res.* **58**, 13910–13917 (2019).
192. Zhang, X. *et al.* Use of acidic nanoparticles to rescue macrophage lysosomal dysfunction in atherosclerosis. *Autophagy* 1–18 (2022) doi:10.1080/15548627.2022.2108252.
193. Liu, Y., Wu, Z., Armstrong, D. W., Wolosker, H. & Zheng, Y. Detection and analysis of chiral molecules as disease biomarkers. *Nat Rev Chem* **7**, 355–373 (2023).
194. Nuzzo, T. *et al.* The levels of the NMDA receptor co-agonist D-serine are reduced in the substantia nigra of MPTP-lesioned macaques and in the cerebrospinal fluid of Parkinson's disease patients. *Sci Rep* **9**, 8898 (2019).
195. Cheng, Q.-Y. *et al.* Sensitive Determination of Onco-metabolites of D- and

- L-2-hydroxyglutarate Enantiomers by Chiral Derivatization Combined with Liquid Chromatography/Mass Spectrometry Analysis. *Sci Rep* **5**, 15217 (2015).
196. Han, M. *et al.* Development and validation of a rapid, selective, and sensitive LC–MS/MS method for simultaneous determination of d- and l-amino acids in human serum: application to the study of hepatocellular carcinoma. *Anal Bioanal Chem* **410**, 2517–2531 (2018).
197. Stachelek, P., MacKenzie, L., Parker, D. & Pal, R. Circularly polarised luminescence laser scanning confocal microscopy to study live cell chiral molecular interactions. *Nat Commun* **13**, 553 (2022).
198. Yuasa, J. *et al.* Fingerprint signatures of lanthanide circularly polarized luminescence from proteins covalently labeled with a β -diketonate europium(iii) chelate. *Chem. Commun.* **49**, 4604 (2013).
199. Orsini, S., Zinna, F., Biver, T., Di Bari, L. & Bonaduce, I. Circularly polarized luminescence reveals interaction between commercial stains and protein matrices used in paintings. *RSC Adv.* **6**, 96176–96181 (2016).
200. Leonzio, M. *et al.* A chiral lactate reporter based on total and circularly polarized Tb(III) luminescence. *New J. Chem.* **42**, 7931–7939 (2018).
201. Fabian, P. *et al.* Lifelong single-cell profiling of cranial neural crest diversification in zebrafish. *Nat Commun* **13**, 13 (2022).
202. Maupin, C. L., Parker, D., Williams, J. A. G. & Riehl, J. P. Circularly Polarized Luminescence from Chiral Octadentate Complexes of Yb(III) in the Near-Infrared. *J. Am. Chem. Soc.* **120**, 10563–10564 (1998).
203. Maupin, C. L. *et al.* The Measurement of Circular Polarization in the Near-IR Luminescence from Chiral Complexes of Yb(III) and Nd(III). *J. Phys. Chem. A* **104**, 6709–6717 (2000).
204. Zinna, F., Arrico, L. & Di Bari, L. Near-infrared circularly polarized luminescence from chiral Yb(III)-diketonates. *Chem. Commun.* **55**, 6607–6609 (2019).
205. Aguiar, J., Estevinho, B. N. & Santos, L. Microencapsulation of natural antioxidants for food application – The specific case of coffee antioxidants – A review. *Trends in Food Science & Technology* **58**, 21–39 (2016).

Quest'opera è stata rilasciata con licenza Creative Commons Attribuzione – non commerciale
Non opere derivate 3.0 Italia . Per leggere una copia della licenza visita il sito web:

<http://creativecommons.org/licenses/by-nc-nd/3.0/it/>

-  **Attribuzione** Devi riconoscere una menzione di paternità adeguata, fornire un link alla licenza e indicare se sono state effettuate delle modifiche. Puoi fare ciò in qualsiasi maniera ragionevole possibile, ma non con modalità tali da suggerire che il licenziante avalli te o il tuo utilizzo del materiale.
-  **NonCommerciale** Non puoi usare il materiale per scopi commerciali.
-  **Non opere derivate** —Se remixi, trasformi il materiale o ti basi su di esso, non puoi distribuire il materiale così modificato.

Improving bioavailability of insoluble payloads through PLGA nanotechnology

Salvatore Calogero Gaglio

Tesi di Dottorato

Verona,
ISBN